Computational study of electron transport in nanocrystalline graphene

vom Fachbereich Material- und Geowissenschaften

der Technischen Universität Darmstadt

zur Erlangung des Grades

DOCTOR RERUM NATURALIUM
(DR. RER. NAT.)

DISSERTATION
VON DELWIN PERERA

Referent: Prof. Dr. rer. nat. Karsten Albe
Korreferent: Prof. Dr. rer. nat. Ralph Krupke

DARMSTADT 2023

COMPUTATIONAL STUDY OF ELECTRON TRANSPORT IN NANOCRYSTALLINE GRAPHENE

Zur Erlangung des akademischen Grades
Doctor rerum naturalium (Dr. rer. nat.)
genehmigte Dissertation von M. Sc. Delwin Perera, geboren in Offenbach a. M.

Fachgebiet Materialmodellierung
Fachbereich Material- und Geowissenschaften
Technische Universität Darmstadt

Referent: Prof. Dr. rer. nat. Karsten Albe
Korreferent: Prof. Dr. rer. nat. Ralph Krupke
1. Prüfer: Prof. Dr. Mads Brandbyge
2. Prüfer: Prof. Dr. rer. nat. Vera Krewald

Tag der Einreichung: 18.11.2022
Tag der Prüfung: 09.02.2023

Darmstadt 2023
D17

Please cite this document as:
URN: urn:nbn:de:tuda-tuprints-233051
URL: https://tuprints.ulb.tu-darmstadt.de/id/eprint/23305

Dieses Dokument wird bereitgestellt von tuprints,
E-Publishing-Service der TU Darmstadt
https://tuprints.ulb.tu-darmstadt.de

tuprints@ulb.tu-darmstadt.de

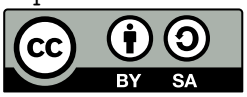

CONTENTS

ERKLÄRUNG ZUR DISSERTATION

Hiermit versichere ich, die vorliegende Dissertation selbständig mit Hilfe der angegebenen Quellen und Hilfsmittel angefertigt zu haben. Alle Stellen, die aus Quellen entnommen wurden, sowie alle Daten, die aus Kollaborationen stammen, sind als solche kenntlich gemacht. Diese Arbeit hat in gleicher oder ähnlicher Form noch keiner Prüfungsbehörde vorgelegen, ein Promotionsversuch wurde von mir bisher nicht unternommen.

Darmstadt, den 18.11.2022

(Delwin Perera)

ABSTRACT

Over the last years graphene research has branched into many fields and sub-fields spanning from pure theory to technology. A first climax of this development was the Nobel Prize in Physics 2010. Since then new milestones have been reached increasingly focussing on the technological application of graphene. Ideally, the extraordinary properties of graphene could be directly transferred from laboratory to commercial devices. Such a straight route, however, does not exist in most cases. Designing and manufacturing graphene-based electronic devices on large scales rather poses additional questions and challenges.

A major challenge is the control of dislocations and grain boundaries in graphene. These defects are typically caused by large-scale synthesis methods such as chemical vapour deposition. Defects often deteriorate pristine material properties like mechanical strength, electric conductivity or electron mobility. In this sense they are clearly undesired, but defects offer new possibilities as well. They can be used to tune for example mechanical or electronic properties and defect engineering has become an increasingly pursuit research area.

In this work, we study a specific type of defect in graphene: grain boundaries at the nanometer scale. Graphene grain boundaries are extended defects but in contrast to three-dimensional materials they are line not area defects. The reduced dimensionality relates them closely to dislocations and other topological defects. Topological defects, generally, change the connectivity between atomic sites without necessarily changing the coordination. This strongly affects the electronic properties of graphene and offers possibilities to engineer electron transport that contrast with commonly used methods like doping or chemical modifications.

A second source to modulate transport properties is mechanical strain. The piezoresistive effect, i.e. the change of electric response upon mechanical strain, is a well-known example. In graphene the piezoresistive effect offers interesting application possibilities in the form of transparent strain sensors due to graphene's optical transparency and mechanical flexibility. The piezoresistive effect in graphene is also an interesting crossing point between electromechanical properties and their interaction with grain boundaries.

Nanocrystalline graphene (NCG) shows a pronounced piezoresistivity suggesting that the high grain boundary density contributes somehow to it. Uncovering the role of grain boundaries for electron transport is invaluable, both theoretically and experimentally. Transport at the length scales relevant in NCG offers a quite interesting opportunity: The problem can be investigated theoretically by quantum-mechanical methods while still accessible to experimental probes. Such a complementary investigation is interesting in itself. We must acknowledge, however, that the theoretical treatment in this thesis, still uses several simplifications that cannot be mimicked in experiments, directly.

First we study how the grain boundary structure influences electron transport in graphene bicrystals. We find that there are generally two transport regimes within the ballistic transport approximation: an energy gap region and, at energies beyond this gap, an ohmic region. The size of the energy gap depends on the bicrystal geometry and can be zero for some bicrystals. The gap region is insensitive to structural variations while the ohmic region is quite sensitive. This insight motivates a purely geometric picture of the emergence and size of transport gaps in graphene bicrystals. Moreover, this picture can be extended to describe a gap modulation by mechanical strain. It is therefore a useful bridge from bicrystals to piezoresistivity in graphene nanocrystals.

The final topic considered in this thesis is an approximation of electron transport in nanocrystals under a uniaxial external strain. The approximate nature lies mainly in the model construction: We use hexagonally shaped grains to establish simple orientation relations between adjacent grains and to reduce the number of additional degrees of freedom. By combining conventional two-terminal transport calculations and transport samples embedded in complex absorbing potentials we find that the grain boundary network exhibits pronounced metallicity at low energies. This indicates that the enhanced piezoresistivity of NCG may be attributed to a finite-size effect.

While a conclusive description of mechanically modulated conductivity in NCG could not be presented, our work establishes important technical insights into ballistic transport calculations of extended structures in general and transport across graphene grain boundaries in particular.

ZUSAMMENFASSUNG

Im Laufe der letzten Jahre hat sich die Graphen-Forschung in viele Gebiete und Untergebiete verzweigt. Diese reichen von Grundlagenforschung bis zu technologischen Anwendungen. Ein erster Höhepunkt dieser Entwicklung war die Verleihung des Physik-Nobelpreises 2010. Seit diesem Zeitpunkt sind neue Meilensteine erreicht worden, die sich zunehmend mit der technologischen Anwendung von Graphen auseinandersetzen. Idealerweise würden die außergewöhnlichen Eigenschaften von Graphen direkt vom Labor auf kommerzielle Anwendungen übertragbar sein. Ein derartiger geradliniger Weg existiert jedoch in den meisten Fällen nicht. Entwurf und Herstellung von graphen-basierten elektronischen Komponenten in großen Mengen bereiten zudem weitere Herausforderungen.

Eine große Herausforderung ist die Kontrolle von Versetzungen und Korngrenzen in Graphen. Diese Defekte treten üblicherweise bei großskaligen Synthesemethoden wie der chemischen Gasphasenabscheidung auf. Defekte setzen die intrinsischen Materialeigenschaften wie mechanische Festigkeit, elektrische Leitfähigkeit oder Elektronenmobilität häufig herab. In dieser Hinsicht sind sie zweifelsohne unerwünscht. Aber Defekte bieten auch neue Möglichkeiten. Sie können beispielsweise benutzt werden, um mechanische oder elektronische Eigenschaften gezielt zu verändern. Dieses sogenannte *Defect Engineering* ist zu einem bedeutsamen Forschungsfeld geworden.

In dieser Arbeit betrachten wir einen speziellen Graphen-Defekttyp: Korngrenzen im Nanometerbereich. Graphen-Korngrenzen sind ausgedehnte Defekte, aber im Gegensatz zu dreidimensionalen Materialien sind sie keine Flächendefekte. Die reduzierte Dimensionalität verbindet sie eng mit Versetzungen und anderen topologischen Defekten. Generell verändern topologische Defekte die Konnektivität zwischen Atomen ohne notwendigerweise deren Koordination zu verändern. Diese Tatsache beeinflusst die elektronischen Eigenschaften von Graphen enorm und bietet die Möglichkeit, Elektronentransport in Graphen gezielt zu steuern, ohne auf übliche Verfahren wie Dotierung oder chemische Modifikation angewiesen zu sein.

Eine zweite Quelle, um die Transporteigenschaften zu modulieren, ist mechanische Dehnung. Der piezoresistive Effekt, d. h. die Änderung der elektronischen Antwort unter mechanischer Dehnung, ist ein bekanntes Beispiel. Der piezoresistive Effekt bietet für Graphen interessante Anwendungsmöglichkeiten in Form transparenter Dehnungssensoren, da Graphen optisch transparent und mechanisch flexibel ist. Der piezoresistive Effekt in Graphen stellt darüber hinaus auch eine interessante Schnittstelle zwischen elektro-mechanischen Eigenschaften und deren Wechselwirkung mit Korngrenzen da.

Nanokristallines Graphen zeigt eine besonders ausgeprägte Piezoresistivität, was darauf schließen lässt, dass die hohe Korngrenzdichte hierfür eine Rolle spielt. Diese Rolle der Korngrenzen für den Elektronentransport zu be-

leuchten, ist sowohl in theoretischer wie auch in experimenteller Hinsicht wichtig. Transport bei den Längenskalen, die für nanokristallines Graphen relevant sind, bietet auch eine interessante Möglichkeit: Das Problem kann theoretisch durch quantenmechanische Methoden untersucht werden, ist aber auch experimenteller Untersuchung zugänglich. Wie müssen allerdings bekennen, dass die theoretischen Untersuchungen in dieser Arbeit dennoch viele Vereinfachungen nutzen müssen, die experimentell nicht direkt nachgebildet werden können.

Zuerst untersuchen wir, wie die Atomstruktur der Korngrenze den Elektronentransport in Graphenbikristallen beeinflusst. Wir kommen zu dem Resultat, dass generell zwei Transportbereiche in der ballistischen Transportnäherung existieren: ein Bereich mit einer Energielücke und bei Energien außerhalb dieser Lücke ein ohmscher Bereich. Die Größe der Lücke hängt von der Bikristallgeometrie ab und kann auch Null betragen für einige Bikristalle. Der Lückenbereich ist unempfindlich gegenüber strukturellen Veränderungen, während der ohmsche Bereich sehr empfindlich ist. Diese Erkenntnis motiviert, ein rein geometrisches Bild zu erstellen, das das Auftreten und die Größe von Energielücken in Graphenbikristallen vorhersagen kann. Dieses Bild kann darüber hinaus erweitert werden, um die Modulation von Lücken durch mechanische Dehnung zu beschreiben. Es ist daher nützlich als Bindeglied zwischen Bi- und Polykristallen.

Das abschließende Thema dieser Arbeit ist die Annäherung an Elektronentransport in Nanokristallen unter uniaxialer mechanischer Dehnung. Die Annäherung bezieht sich hauptsächlich auf die Modellerzeugung: Wir benutzen sechseckige Körner, um eine vereinfachte Orientierungsbeziehung zwischen benachbarten Körnern zu haben und die Anzahl zusätzlicher Freiheitsgrade zu reduzieren. Durch Kombination von konventionellen Zwei-Elektroden-Transportrechnungen und Transportproben, die in ein komplexes Absorptionspotential eingebettet sind, gelangen wir zu dem Schluss, dass das Korngrenznetzwerk eine auffällige Metallizität bei niedrigen Energien aufweist. Dies deutet darauf hin, dass die erhöhte Piezoresistivität von nanokristallinem Graphen ein *Finite-Size*-Effekt sein könnte.

Obwohl wir keine abschließende Beschreibung der mechanisch modulierten Leitfähigkeit in nanokristallinem Graphen bieten können, hat unsere Arbeit wichtige technische Erkenntnisse zu ballistischen Transportrechnungen in ausgedehnten Strukturen generell, und für Transport über Graphenkorngrenzen im Besonderen, geliefert.

DANKSAGUNG

Zum Gelingen einer Doktorarbeit ist die Unterstützung, das Interesse und der Rückhalt einiger Leute notwendig. Ihnen allen danke ich im Folgenden. Zuerst danke ich meinem Doktorvater, Karsten Albe, dafür, dass ich meine Arbeit in seiner Arbeitsgruppe anfertigen konnte und dass er mir seit meinem Studienbeginn mit Rat und Hilfe zur Seite gestanden ist. Ralph Krupke danke ich für die Zweitbegutachtung dieses Werks. Ihm verdanke ich auch viele interessante Diskussionen über die experimentellen Aspekte meines Forschungsthemas. Mads Brandbyge und Vera Krewald danke ich dafür, Mitglieder meiner Prüfungskommission zu sein.

During my research stay in 2019 at DTU, Denmark, Mads Brandbyge has shown great interest in my work and contributed many insightful remarks and suggestions. I thank him very much for a pleasant and instructive stay at his group.

Meinen Kollegen in Darmstadt und Dänemark danke ich besonders herzlich für die wunderbare Arbeitsumgebung und all die Erlebnisse, die wir in den vergangenen Jahren hatten.

Besonders hervorheben muss ich Jochen Rohrer. Er hat mich nun schon viele Jahre lang begleitet und mich als Wissenschaftler maßgeblich geprägt – dieser Satz dürfte ihn gewiss schmunzeln lassen. Seine Fähigkeit die richtigen Fragen zu stellen und an Probleme unvoreingenommen heranzugehen, hat mir nicht nur oft geholfen, sondern mich auch inspiriert.

Abschließend danke ich meiner Familie, insbesondere meinen Eltern, für ihren Rückhalt und ihre Liebe.

1 | INTRODUCTION

Sensors, microchips and transistors are ubiquitous in our world. Within a few decades electronic technology has become an integral part of society and the pace at which electronics has advanced is staggering. This development is exemplified by the miniaturization of electronic components. Well-known are the images of computing machines around the middle of the last century that filled large factory halls but offered a computing power far below personal computers of the early 2000s. Miniaturization necessarily leads to the ultimate boundaries of matter: the world of atoms and their quantum mechanical interactions.

The technological exploration at the edge of length and time scales poses enormous challenges on experimental and theoretical methods. Fundamental research in mesoscopic systems utilizes a large arsenal of synthesis and analysis methods developed over the course of several decades. Many-body perturbation theory offers sophisticated techniques to give complimentary theoretical analysis of experiments. How mature mesoscopic physics has become is perhaps best illustrated by the dizzying speed of research activity around graphene from fundamental aspects of condensed matter physics to various technological applications [1–4]. Indeed, graphene research has not only benefited from the evolution of mesoscopic physics but has itself advanced its state substantially.

This thesis focuses on a small part of the graphene landscape. The desire to synthesize graphene on large scales for cost-efficient use in electronic technology has triggered a growing interest in various kinds of defects in graphene. Grain boundaries (GBs), in particular, are in the spotlight of attention for two reasons: First, GBs are practically inevitable defects in large scale graphene sheets and second, they impact the properties of graphene substantially. Therefore, graphene GB research itself has become a very active and large field over the last years and consequently the focus of this work is still narrower: A theoretical investigation of electron transport in *nano*crystalline graphene under the influence of mechanical strain.

Nanocrystalline graphene (NCG) exhibits a strong change of resistivity towards an external strain [5]. This *piezoresistive* effect is not exclusive to nanocrystalline graphene but observed in macro- and singlecrystalline graphene as well [6, 7]. However, nanocrystalline graphene shows response factors that are at least an order of magnitude higher.

To provide some background on graphene and polycrystalline graphene, Sec. 1.1 sketches significant historic developments of graphene research and basic properties of graphene. Section 1.2 introduces general aspects of graphene GBs. The investigation of piezoresistivity in nanocrystalline graphene, though interesting in itself, is motivated by its potential application in strain sensing—especially, since nanocrystalline graphene is both flexible and transparent,

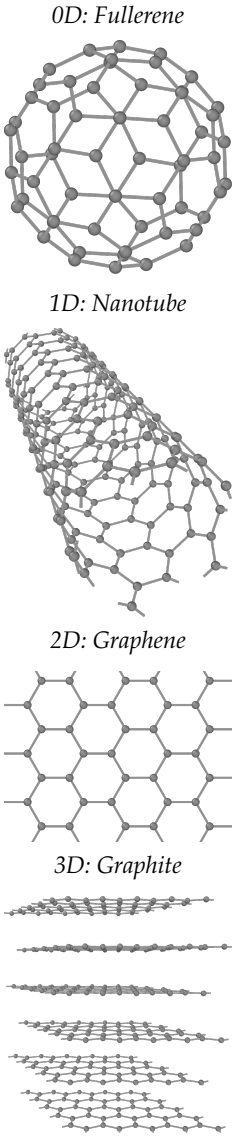

FIGURE 1.1 | Graphitic carbon allotropes from zero to three dimensions.

which is a strong advantage over the widely used indium-tin-oxide. Section 1.3 discusses strain sensing in general, followed by the experimental results on NCG that form the starting point of this work. The final section of this chapter (Sec. 1.4) presents the main research questions of this work and sketches how these questions will be addressed.

1.1 GRAPHENE: HISTORY, PROPERTIES, CHALLENGES

The explosion of research activity on graphene and other two-dimensional materials in the last years is commonly traced back to the experimental exfoliation of few-layer graphene from graphite via micromechanical cleavage by Geim and Novoselov in 2004 [8]. Subsequent electrical transport measurements of monolayer graphene in 2005 revealed unexpected properties: an ambipolar electric field effect with huge carrier mobilities [9] and the discovery of the anomalous quantum Hall effect and Berry's phase [10, 11]. The combination of these exotic phenomena with an intrinsically 2D system triggered a race to uncover more and more remarkable properties of graphene [1, 12–15].

The start of graphene research, however, dates back much further and is generally linked to the theoretical description of the band structure of graphite monolayers by Wallace in 1947 [16]. The first experimental evidence of isolated graphite monolayers was given by Boehm, who later coined the term *graphene*, in 1962 [17]. However, this work remained somewhat singular since no systematic procedure existed to obtain graphene reproducibly and with a sufficient quality to perform mesoscopic measurements.[†]

Graphene, at least as a theoretical concept, received new attention with the synthesis of novel carbon allotropes in the form of fullerenes [18] and especially carbon nanotubes [19]. Together with graphite, these allotropes can all be regarded emerging from graphene either by forming a ball (fullerene), rolling up a cylinder (nanotube), or stacking along the out-of-plane axis (graphite)—see Fig. 1.1. It was realized that the electronic structure of carbon nanotubes is fundamentally related to the band structure of graphene [20–22]. Indeed, the tight binding description of graphene has been an essential tool to describe the electronic properties of carbon nanotubes qualitatively and to some extent even quantitatively [23]. The close analogy of the electronic structure between nanotubes and graphene nanoribbons—the so called *multiples-of-three* rule [24, 25]—is also shared by graphene GBs.

Graphene exhibits a linear dispersion in the low-energy region of its spectrum thus its charge carriers can be described by the Dirac equation. The peculiar properties of such a two dimensional gas of Dirac fermions were anticipated by several theoretical works [26–29]. With the reproducible isolation of graphene it was possible to probe quantum electrodynamical phenomena such as zitterbewegung and Klein tunneling directly [1, 30–34]—phenomena that had not been observed in other condensed matter systems so far. A major part of the low-energy electronic structure of graphene originates somewhat

[†]The field of mesoscopic physics itself was in its infancy at that time.

from a simple fact: Graphene has a two-dimensional hexagonal bipartite lattice (Fig. 1.2). It follows that atoms from one sublattice (●-type) have only atoms from the other sublattice (○-type) as nearest neighbors and next-nearest neighbors are from the same sublattice type. Restricting interactions to nearest neighbors the following second quantized Hamiltonian can be defined [35]:

$$\mathcal{H}(\mathbf{r}) = \sum_i \epsilon_0 \hat{c}_i^\dagger(\mathbf{r})\hat{c}_i(\mathbf{r}) + \sum_{\langle ij \rangle} t\hat{c}_i^\dagger(\mathbf{r})\hat{c}_j(\mathbf{r}) + \text{h.c.} \tag{1.1}$$

Here the first sum is over both sublattices and the second sum is between the sublattices; $\hat{c}(\mathbf{r})$ $[\hat{c}^\dagger(\mathbf{r})]$ is the electron annihilation (creation) operator, respectively. The parameter ϵ_0 represents the so-called on-site energy which is set to zero in this discussion without loss of generality and t is the energy for electron transfer from one lattice site to a neighboring site.

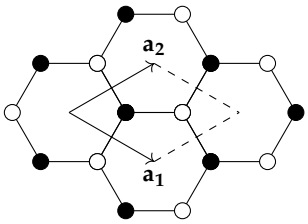

FIGURE 1.2 | Graphene lattice and primitive unit cell. The sublattices are indicated by different coloring of lattice sites.

The energy spectrum, $E_\pm(\mathbf{k})$, is obtained by diagonalizing the Fourier transformed Hamiltonian of Eq. (1.1), see Ref. [35],

$$E_\pm(\mathbf{k}) = \pm t\sqrt{3 - f(\mathbf{k})}, \tag{1.2}$$

with

$$f(\mathbf{k}) = 2\cos\left(\sqrt{3}k_y a\right) + 4\cos\left(\frac{\sqrt{3}}{2}k_y a\right)\cos\left(\frac{3}{2}k_x a\right). \tag{1.3}$$

Equation (1.3) can be expanded to first order around the Dirac points $\mathbf{K}^\dagger$ by defining the relative momentum $\mathbf{q} = \mathbf{K} + \mathbf{k}$ as

$$E_\pm \simeq \pm v_{\text{Fermi}}|\mathbf{q}| + \mathcal{O}\left((q/K)^2\right), \tag{1.4}$$

where $v_{\text{Fermi}} = 3ta/2$ is the Fermi velocity in terms of the hopping parameter. This expansion is an integral part of this thesis. In Ch. 4 it is shown that the linearity of the Dirac cones is an excellent approximation for the treatment of the electronic structure in polycrystalline graphene. Equation (1.4) is indeed so convenient that it is the basis of a semi-analytical approach to the transport gap problem for arbitrary graphene GBs presented in Ch. 6.

†The Dirac points are located at

$$\mathbf{K} = \left(\frac{2\pi}{3a}, \frac{2\pi}{3\sqrt{3}a}\right)$$

and

$$\mathbf{K}' = \left(\frac{2\pi}{3a}, -\frac{2\pi}{3\sqrt{3}a}\right),$$

with lattice constant a.

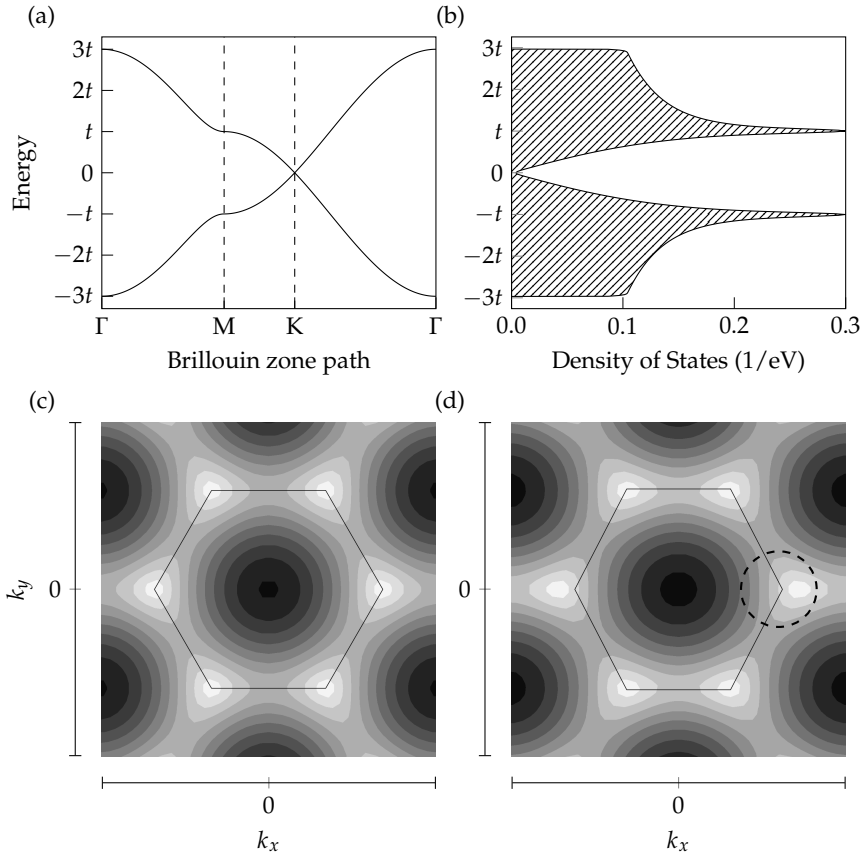

FIGURE 1.3 | Electronic structure of graphene based on a nearest neighbor tight-binding model [Eq. (1.1)]. Band structure along high symmetry points of pristine graphene (a) and Brillouin zone integrated density of states (b). Two-dimensional band structure at the valence band maximum of unstrained (c) and strained (d) graphene. Strain displaces the Dirac cones from the vertices of the Brillouin zone as indicated by the dashed circle in (d).

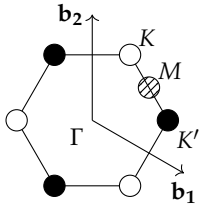

FIGURE 1.4 | There exist two Dirac points K and K' with different parity alternating at the vertices of the hexagonal Brillouin zone. These *valleys* are degenerate without spin-polarization.

Figure 1.3 summarizes the electronic structure of graphene based on the Hamiltonian of Eq. (1.1). The band structure [Fig. 1.3 (a)] is calculated along the path $\Gamma \to \mathrm{M} \to \mathrm{K} \to \Gamma$ consisting of high symmetry points in the hexagonal Brillouin zone (Fig. 1.4). The maximum band width at the Γ point is $6t$. The most pertinent feature of the band structure is the linear dispersion around K where the bands cross. Associated with this band structure Fig. 1.3 (b) shows the density of states. Here, three features stand out: (1) the van-Hove singularities at $\pm t$, (2) the zero density of states at the Fermi energy, (3) the symmetry between electrons and holes. (1) and (2) are directly related to the band structure, whereas (3) is a consequence of the nearest neighbor interaction. In general, the inclusion of next-nearest neighbor interactions or irregularities of the lattice break electron-hole symmetry [36, 37]. Another symmetry best

seen in the two-dimensional view of the top-most valence band [Fig. 1.3 (c)] is the so-called trigonal warping around the Dirac points [38]. This threefold symmetry is a feature common to all low-dimensional forms of carbon—it also occurs in nanotubes and ribbons. The warping will play a role in the discussion of strain-induced transport gap modulation in Ch. 6 because it determines how the Fermi velocity is affected by strain. In fact, the application of strain generally shifts the Dirac points away from the high symmetry sites and distorts the trigonal warping.

Pristine graphene is a semi-metal at zero temperature and a metal at finite temperatures. While its ambipolar electric field effect and ultrafast charge carrier mobility are interesting features for electronic amplification, graphene's gapless nature makes it unsuitable for applications in conventional digital electronics [3]. Therefore, substantial efforts exist to create energy gaps in graphene without sacrificing most of its extraordinary properties. Apart from chemical [39–43] and strain engineering [44–47], *quantum confinement* is a promising route for creating energy gaps. Quantum confinement is a concept borrowed from the electronic structure of carbon nanotubes. The definite circumference of a nanotube determines the periodicity of the wave functions. This periodicity discretizes the momentum space so that not all wave numbers are available anymore [24, 25]. The location of the Dirac points with regard to the allowed wave numbers determines if a nanotube is metallic or semi-conducting [21, 22].[†] The discretization of momentum space is also present in graphene nanoribbons [48, 49]. Indeed, the electronic structure of nanoribbons can be used as a calculation tool for the electronic structure of nanotubes. The experimental realization of graphene nanoribbons, however, is more complicated. A considerable challenge is the control of edge roughness and large scale synthesis of well-defined nanoribbons is currently not available [50]. Graphene GBs could provide a better alternative. They have an analogous electronic structure while their preparation, especially at large scales, does not require much effort. On the contrary, GBs are virtually inevitable for graphene grown by conventional synthesis methods such as chemical vapour deposition (CVD) [51–53].

[†]The curvature can have an additional influence, rendering certain metallic nanotubes also semi-conducting.

1.2 GRAIN BOUNDARIES IN GRAPHENE

The ability to synthesize large area graphene is often considered to be one of the most important steps towards graphene-based electronics. A promising attempt into this direction is the growth of graphene by chemical vapour deposition (CVD) from hydrocarbons on a metal substrate—such as Iridium [54], Nickel or Copper [55, 56]. Important input parameters of the CVD process are precursor material, temperature and pressure. On the output side the yield, sheet size, and most importantly the quality of graphene are the relevant parameters. Yield and sheet size are strongly influenced by the precursor materials, the metal substrates and the process parameters (temperature and

pressure). Detailed studies have been carried out to develop an understanding of the underlying thermodynamics and kinetics [56].

The quality of the synthesized graphene is certainly a more vague concept to assess. Commonly, electronic properties such as resistivity and charge carrier mobility and the Raman spectrum are evaluated. Raman spectroscopy is a powerful probe to characterize a variety of fundamental properties of graphene samples in a non-invasive way [57]. It is an ideal tool to check the quality of graphene grown by various synthesis methods at different scales and is sensitive to the presence of defects [58] and perturbations from external fields [59].

Improved control over the process parameters and the use of flexible substrates have resulted in increasing graphene film sizes and additional transfer processes to transparent polymer substrates [60]. These developments are particularly relevant for transparent flexible electrodes used for example as sensors in touch screens [61].

The presence of GBs in CVD-grown graphene samples has directed attention to the interplay between GB structure and graphene's intrinsic properties. Intuitively, GBs are expected to severely degrade properties such as the mechanical strength or electrical conductivity. The impact of GBs on the mechanical strength of graphene has been studied in various works [63–67] revealing that GBs are not generally detrimental. Rather the specific GB structure leads to either a weakening or even a strengthening of graphene [63, 65]. To appreciate this counter-intuitive result a knowledge of the detailed structure of graphene GBs is required. In the absence of extrinsic defects a threefold coordination of the carbon atoms is energetically most favorable. Graphene GBs, due to their 1D nature, can be specified by a rotation angle θ and a repeat length d. Depending on the exact choice of θ and d the lattices of the participating grains are either commensurate or incommensurate. For incommensurate lattices a finite mismatch strain needs to be exerted on the grains. All rotations—apart from highest symmetry rotations (0°, 60° and multiples) which introduce no misorientation at all—require the introduction of non-hexagonal polygons

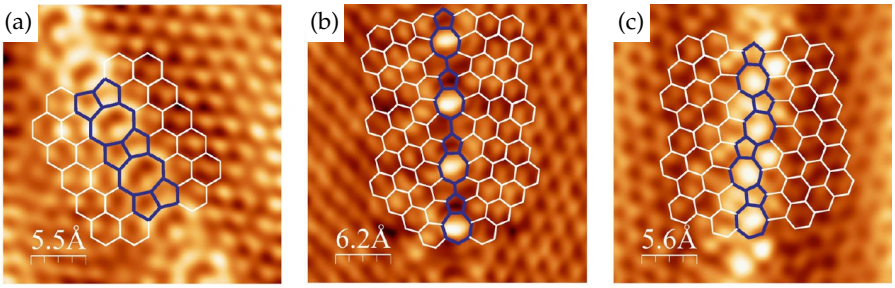

FIGURE 1.5 | Experimental scanning tunneling microscopy images of different graphene GBs. *Reprinted and adapted with permission from Ref. [62]. Copyright © 2014, American Chemical Society.*

to connect adjacent grains. Experimental studies of graphene GBs generally observe n-gons with $n \in (5, 7, 8)$. Figure 1.5 shows experimental scanning tunneling microscopy images of graphene polycrystals from a study by Yang *et al.* [62]. With the exception of Fig. 1.5 (a), the GBs feature pentagons and heptagons with different density and connectivity. Similarly, a combined experimental and theoretical study by Ophus *et al.* indicates that the majority of GBs is a patchwork of pentagons and heptagons [68].

The prevalence of these polygons is motivated by the following geometrical construction (Fig. 1.6): A semi-infinite 60°-wedge inserted into (removed from) the regular graphene lattice generates a positive (negative) *disclination* accommodated by a pentagon (heptagon) [69–71]. With these elementary building blocks both dislocations and GBs can be explained as topological entities based on a patchwork of disclinations. The topological nature of these defects has many implications for the mechanical [72, 73] and functional properties [74–76] of graphene polycrystals. Apart from the influence on mechanical strength mentioned above, disclinations also play an important role for out-of-plane buckling in graphene.

In this work all graphene models are flat, but it is known that even pristine graphene is buckled at finite temperatures [77] since bond length fluctuations induce instabilities. Polycrystalline graphene is generally buckled, too, as the GBs act as a network of junctions between the differently corrugated grains. From a mechanical viewpoint this is not surprising: Unresolved line forces along the interfaces within the plane can only resolve along the out-of-plane degree of freedom. A considerable body of literature connects this result from standard elasticity theory with investigations into the atomic structure of graphene [78–80].

Buckling has additional influences on mechanical stability and mechanical reversibility—the latter aspect is relevant for strain sensing. Moreover, the electronic properties of buckled graphene sheets may be profoundly different compared to flat graphene. However, systematic investigations on the interplay between buckling and electronic properties are scarce—an overview is given in Ref. [81]. A theoretical treatment of this problem suffers from the considerable increase of complexity: All simplifications from the reduced dimensionality need to be abandoned; in particular simple model Hamiltonians that account only for the $\pi - \pi$ bonds between carbon atoms must be replaced by more complicated Hamiltonians. Computationally, this means that the investigable system size shrinks notably. The situation may be further complicated by graphene-substrate interactions. These added difficulties lead to the old question of what constitutes a good model. Is buckling an essential aspect of electron transport in graphene polycrystals? We believe that the most dominant aspects of electron transport are governed by topological properties of the polycrystal: grain misorientation and grain size. This justifies to investigate flat polycrystals and ignore additional effects of buckling bearing in mind that our results are less valid for strongly corrugated graphene sheets

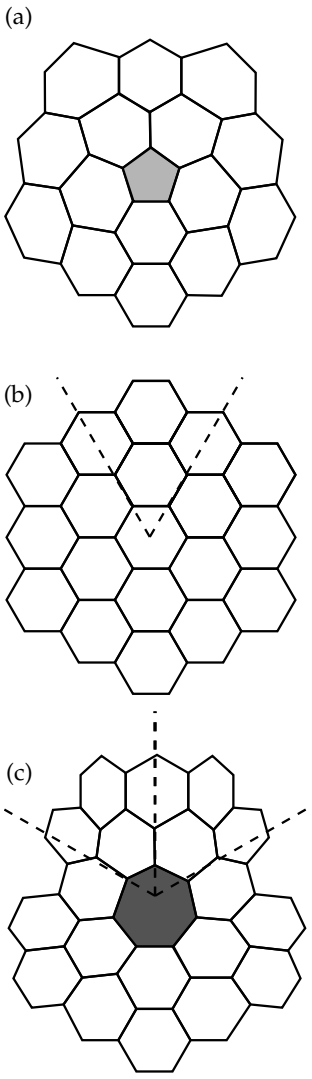

FIGURE 1.6 | Genesis of pentagon (a) [heptagon (c)] defect from pristine (b) graphene via removal (insertion) of a 60°-wedge (dashed lines). Adapted from Ref. [69].

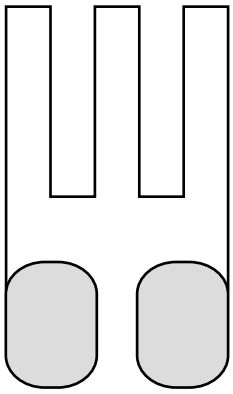

FIGURE 1.7 | Example of a simple strain sensor: A *linear* strain gauge can be realized with a very thin meandering metal stripe on a flexible polymer substrate. The gauge combines large contact pads (grey rectangles) with fine metal stripes to enhance the sensitivity.

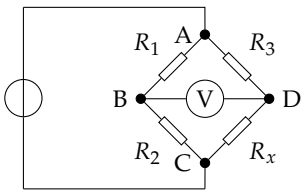

FIGURE 1.8 | Circuit diagram of the Wheatstone bridge. The unknown resistance R_x is given by the resistance ratio $R_x = \frac{R_2 R_3}{R_1}$ if the voltmeter shows zero voltage.

Type	GF
SCG/MCG	1.5-7
NCG	20

Table of strain gauge factors for single- (SCG) and microcrystalline (MCG) graphene from Ref. [7] and nanocrystalline graphene (NCG) from Ref. [5].

or high mechanical strains.

1.3 NANOCRYSTALLINE GRAPHENE FOR STRAIN SENSING

Sensors are an integral part of today's technology and the demands on sensor materials are high: Cost-efficient synthesis combined with often contradictory properties. Transparent strain sensors, for example, should offer mechanical flexibility, strength, optical quality, and high response factors. These sensors are important for the expanding fields of bio-medical sensing and flexible electronics.

From the above list of properties for strain sensors probably the most important is the response or *strain gauge* factor. Generally, a strain sensor relates an electrical input signal ξ_0 to an output signal ξ by a strain-dependent proportionality factor: $\xi \propto \alpha(\epsilon)\xi_0$. The input and output signal is the electrical resistance which for a specific geometry becomes the resistivity and is a material property. It is easier, though, to measure electrical voltages and determine the resistances indirectly. The *Wheatstone* bridge is the prototypical circuit to measure resistance changes. Here, the input and output voltages and the known resistances of all but one resistor allow to determine the unknown resistance. This unknown resistance is, in the case of strain sensing, the strain-dependent resistance of the strain gauge. The general proportionality relation above translates for the Wheatstone bridge (Fig. 1.8) to

$$V_{\text{out}} = f[R_{\text{SG}}(\epsilon); \lambda_i] V_{\text{in}}, \tag{1.5}$$

where the function f depends on the strain gauge resistance R_{SG} and on arbitrary other parameters λ_i of the sensing device.

In this thesis, we are concerned with the material specific aspects of the strain gauge and this is mainly contained in R_{SG}. To compare different materials and eliminate all explicit dependencies on the system geometry a so-called gauge factor is defined:

$$\text{GF} = \frac{\Delta R / R_0}{\epsilon} = 1 + 2\nu + \frac{\Delta\rho/\rho_0}{\epsilon}. \tag{1.6}$$

Equation (1.6) contains two contributions: a mechanical, i.e. the Poisson ratio ν, and an electronic, i.e. the resistivity ρ (see Fig. 1.9). These contributions have different weights depending on the material class. At constant temperature the resistivity of a metal hardly changes making the second term in Eq. (1.6) negligible. Thus, the gauge factor of metal-based strain gauges is almost exclusively determined by geometric deformation via the Poisson ratio and generally on the order of 1-5. On the other hand, strain gauges based on semiconductors reach much higher values. Here the mechanical contribution to the gauge factor can be neglected since the resistivity changes considerably with strain. This resistivity change is often related to a piezoresistive effect, i.e. the electronic structure of the material changes notably under strain. For silicon,

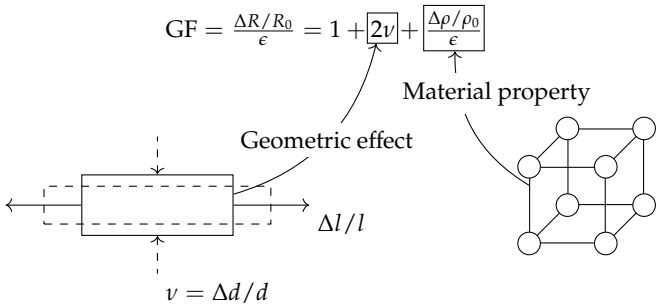

FIGURE 1.9 | The gauge factor contains a geometric and a material specific term. This factor is the most important figure of merit to assess the quality of a strain gauge.

for example, this is the change of the intrinsic band gap. In this example the piezoresistive effect is strongly temperature-dependent and strain sensors operating at high temperatures need to use different sensing mechanisms.

From the experimentally observed high gauge factor of NCG (Fig. 1.10), it is expected that the dominant contribution in Eq. (1.6) is the resistivity term. How does the resistivity in graphene change with strain? Pristine graphene is a semi-metal and at finite temperatures it behaves like a metal so that its piezoresistivity is expected to be rather low. The enhanced piezoresistivity of NCG may therefore be attributed to the presence of GBs. In principle, GBs could have two effects here: a direct effect changing the electronic structure of the polycrystal and an indirect *finite size* effect. Two theoretical studies have received considerable attention as they demonstrated that GBs can induce energy gaps for ballistic electron transport across the GB [82], and that such gaps are modulated by external strains [83]. These findings give an interesting hint that a strong piezoresistive effect in graphene polycrystals stems from the GBs—this speaks for a direct effect. That NCG has a higher strain gauge factor than microcrystalline graphene is then, of course, the effect of a higher GB density.

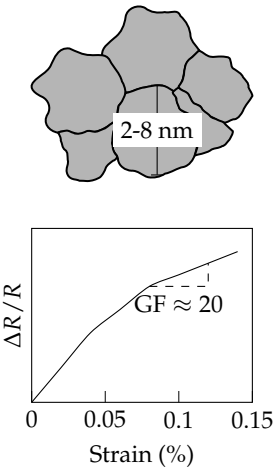

FIGURE 1.10 | Grain size in NCG and strain gauge factor with approximate data from Ref. [5].

1.4 RESEARCH QUESTIONS

Although theoretical works have demonstrated that GBs can evoke semiconducting behavior as mentioned in the last section, drawing a direct connection between these findings and the enhanced piezoresistivity in NCG may be premature. The above implications are based on ballistic electron transport across bicrystal GBs and as such only strictly applicable within these approximations. With average grain sizes of a few nanometer, however, electrons may propagate quite freely in NCG—at least if disorder at GBs is not dominant.

We use ballistic transport across bicrystal GBs as the starting point of our work. In Ch. 5 we address the question to what extent electron transport is affected by the local atomic GB structure. To investigate electron transport, we

first present the essentials of the calculation tools: Chapter 2 surveys the basic aspects of density functional theory (DFT) and the tight binding approach. Both electronic structure methods are used for transport calculations within the Green function formalism outlined in Ch. 3. The preparation of GB models via structural optimization of graphene grain patchworks is addressed in Ch. 4 along a general geometric description of graphene GBs.

Aside from the sensitivity of electron transport on the GB structure the ballistic approximation suggests a substantial abstraction of the essential transport properties of arbitrary bicrystals and external strains. In Ch. 6 we implement this abstraction to predict the strain modulation of electronic transport gaps. Chapters 5 and 6 discuss import aspects of GBs from the perspective of bicrystals relevant to the more complicated situation in NCG. Of course, transport across bicrystal GBs corresponds only to transport from one grain to another in NCG. Transport *along* GBs is thus not covered until Ch. 7 and there indirectly. The results of the bicrystal chapter will therefore primarily give qualitative guides on the transport behavior of the polycrystals.

Chapter 7 examines simplified structural models of NCG. The main simplification consists of the hexagonally shaped grains which lead to triple point junctions usually present in realistic polycrystals. The simplified models allow us to consider fixed and well-defined misorientations that are easier to relate to the bicrystal models than arbitrary interfaces. The central question of this chapter is therefore to what extent the insights of bicrystal transport are transferable to polycrystals and what features emerge from the more complicated GB network. In this regard the three results chapters of this work can be grouped into two areas of electron transport: Transport across individual GBs (Chs. 5 and 6), and transport within a network of GBs.

Figure 1.11 gives a schematic summary of the main questions addressed in this thesis.

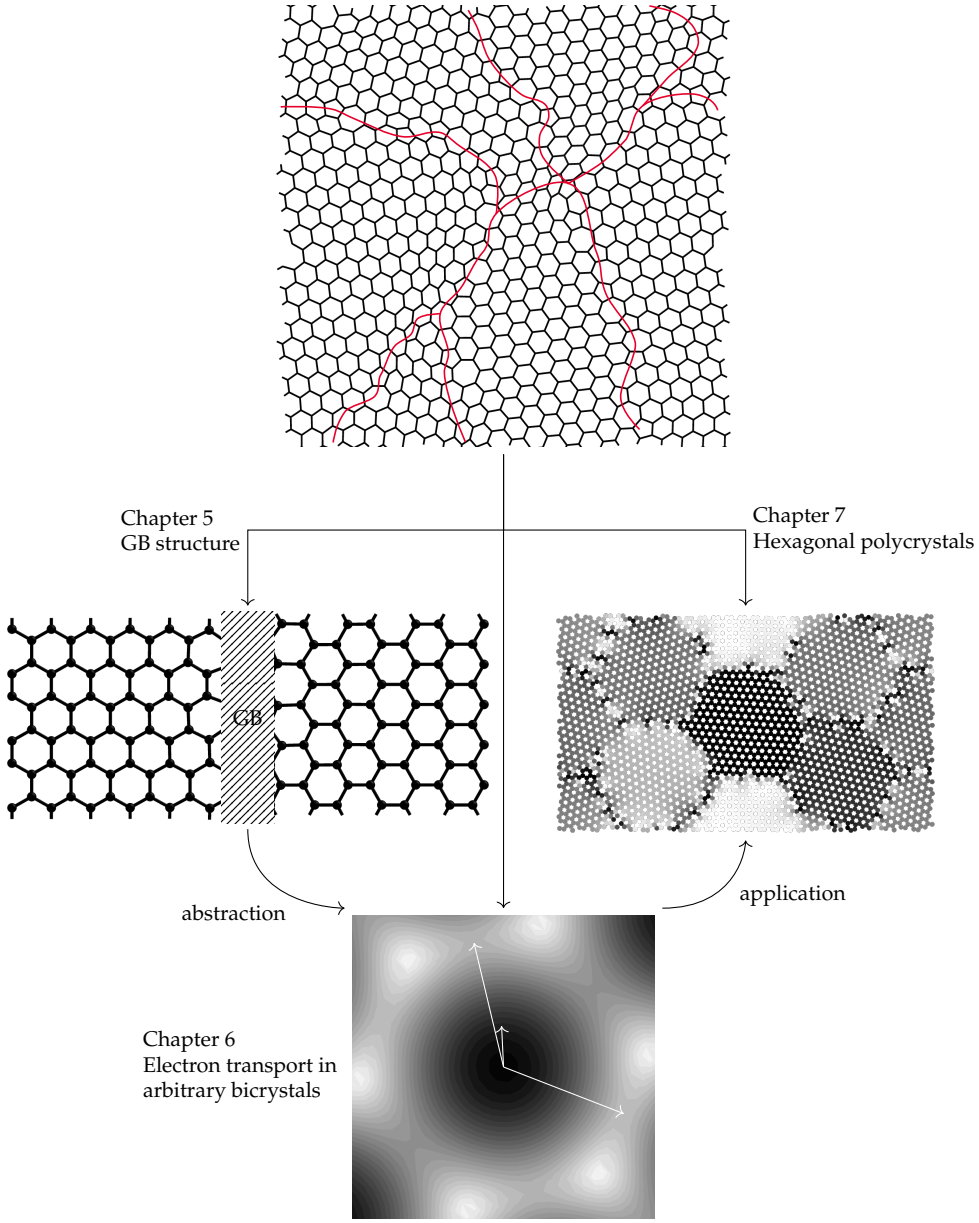

FIGURE 1.11 | Decomposition of the problem of mechanically modulated electron transport in NCG into: the influence of the local GB structure on transport (Ch. 5), abstraction of bicrystal transport to arbitrary misorientations and strains (Ch. 6), ballistic transport in structurally simplified polycrystal models (Ch. 7).

The ground-state electronic structure is a prerequisite for transport calculations. In this chapter we sketch two methods to compute the electronic structure: density functional theory (DFT) and the tight binding (TB) approximation. DFT calculations carried out in this work are based on the open source Fortran code SIESTA [84, 85]. After a brief summary of general DFT in Sec. 2.1, we show specific features of SIESTA DFT calculations relevant to our work in Sec. 2.2. This concerns the nature of the SIESTA Hamiltonian and how the band structure, density of states and the atomic forces are calculated.

Conceptually, the TB approximation is closely related to the linear combination of atomic orbitals (LCAO) used by SIESTA to generate the system's wave functions. In fact, the TB approximation is usually understood to be just a simplified LCAO model based on empirical data. This simplification means that TB Hamiltonians typically deal with nearest-neighbor couplings only and that there is no overlap between different atomic wave functions. In Sec. 2.3, we illustrate these aspects of the TB method with numerical calculations of simple models (1D atomic chain, pristine graphene) using the open source Python code SISL [86].

In a broader sense the TB approximation is the foundation of all transport calculations performed in this work. Chapter 3 will make this clearer.

2.1 DENSITY FUNCTIONAL THEORY

Increasing computer power and efficient numerical algorithms have made DFT the standard method for electronic structure calculations used in solid state research today. At the heart of DFT lies a publication from 1964 by Hohenberg and Kohn [87]. It states the following two theorems:

Theorem 2.1.1 *The ground-state electron density $n_0(\mathbf{r})$ determines the external potential V_{ext} uniquely, apart from a constant.*

Theorem 2.1.2 *There exists a functional of the electron density $E[n(\mathbf{r})]$ which is minimized by the ground-state density $n_0(\mathbf{r})$. This functional corresponds to the ground-state energy.*

The Hohenberg-Kohn theorems establish that the electron density can replace the ground-state wave function [88]. However, the exact form of the ground-state density functional is generally unknown. Reformulating the many-body problem in terms of the electron density therefore does not yield an immediate gain.

Practical DFT calculations need a specific set of equations to minimize the energy functional numerically. Kohn and Sham proposed an ansatz in which the many-body wave function is decomposed into one-particle wave

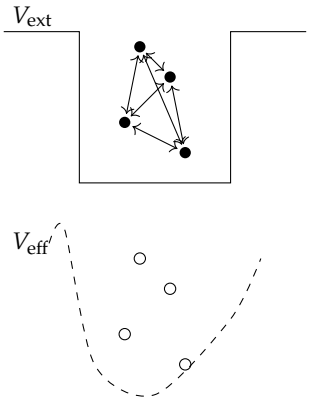

FIGURE 2.1 | The Kohn-Sham ansatz transforms the difficult problem of interacting particles • within an external potential to the simpler problem of non-interacting particles ○ within an effective potential. Adapted from Ref. [91].

functions subject to an effective potential [89, 90]. In this way, the n-body Schrödinger equation separates into n single-particle Schrödinger equations (see also Fig. 2.1):

$$\mathcal{H}^{\text{KS}}\phi_i = \epsilon_i\phi_i. \tag{2.1}$$

The Kohn-Sham Hamiltonian $\mathcal{H}^{\text{KS}}$ reads as: $\mathcal{H}^{\text{KS}} = T[n] + V_{\text{eff}}$ with $V_{\text{eff}} = V_{\text{H}}[n] + V_{\text{ne}}[n] + V_{\text{xc}}[n]$. All operators depend on the electron density. The kinetic energy operator $T[n]$ is expressed using single particle wave functions instead of the kinetic energy of the homogeneous electron gas thereby curing a major defect of the Thomas-Fermi approximation [92, 93]. The effective potential V_{eff} consists of the Hartree potential $V_{\text{H}}[n] = e^2 \int \mathrm{d}^3r' \, \frac{n(\mathbf{r}')}{\mathbf{r}-\mathbf{r}'}$, the external potential between the nuclei and the electrons $V_{\text{ne}}[n]$, and the exchange-correlation potential $V_{\text{xc}}[n]$ which comprises all many-body effects. The kinetic energy of the nuclei and the electrostatic potential between the nuclei do not explicitly enter the Kohn-Sham Hamiltonian due to the Born-Oppenheimer approximation.[†] The total energy therefore depends only parametrically on these quantities. The electron density is obtained from the one particle wave functions, $\phi_i(\mathbf{r})$, as

$$n(\mathbf{r}) = \sum_i^N f_i |\phi_i(\mathbf{r})|^2, \tag{2.2}$$

where f_i is the occupation number.

An important step from the Hohenberg-Kohn theorems to the Kohn-Sham equations is the introduction of the exchange-correlation energy, $V_{\text{xc}} = \delta E_{\text{xc}}/\delta n$. Since E_{xc} by definition contains all many-body effects of the interacting electron gas it seems that the difficulties have just been shifted. Again a practical calculation needs a concrete form of E_{xc}. To this day no exact form for the exchange-correlation energy is known, however, and approximations are required. A first approximation of E_{xc} is to consider local properties of the homogeneous electron gas leading to the *local density approximation* (LDA)

$$E_{\text{xc}}^{\text{LDA}} = \int \mathrm{d}\mathbf{r} \, \epsilon_{\text{xc}}[n(\mathbf{r})]n(\mathbf{r}), \tag{2.3}$$

where ϵ_{xc} is the exchange-correlation energy per particle. Surprisingly, the LDA is already a very good approximation yielding accurate results for many systems. This property of the LDA results from an implicit *sum rule*: Given an electron at a point $\mathbf{r}$, the electron density around this point of all other electrons is reduced with regard to the average density such that integrated with the hole density it is unity [90]. Often, however, the LDA can be improved by more involved techniques to yield more accurate values of specific quantities—for example lattice parameters. Such an improvement consists in expanding the electron density in a gradient series. The generalized gradient approximation (GGA) is such a refined approximation for the exchange-correlation energy.

[†]The Born-Oppenheimer approximation states that the electronic degrees of freedom are decoupled from the nuclear degrees of freedom owing to the large mass difference between electron and proton.

In the case of graphene studied with SIESTA we found a lattice parameter of 1.442 Å for GGA while LDA gives 1.453 Å which is atypical since LDA is known to generally underestimate the lattice parameters [88]. Therefore, we use the GGA exchange-correlation functional for all subsequent DFT calculations in the parametrization of Perdew, Burke, and Ernzerhof [94].

2.2 DFT CALCULATIONS WITH SIESTA

The evaluation of the matrix elements of the single-particle operators in Eq. (2.1) requires a specific set of basis functions. There are many different schemes available, but three popular choices are: expansion in plane waves, finite differences, and expansion with linear combination of atomic orbitals (LCAO). The LCAO is used by SIESTA [95]. The electron density is determined self-consistently from the one particle wave functions starting with some trial wave functions—for example a superposition of atomic wave functions. A useful quantity that expresses the electron density via the atomic orbitals is the *density matrix*:

$$\rho_{\mu\nu} = \sum_i c_{\mu i} n_i c_{i\nu}. \tag{2.4}$$

Here, c_μ and c_ν are expansion coefficients of the ith wave function $\Psi_i = \sum_\mu \phi_\mu(\mathbf{r}) c_{\mu i}$ with atomic orbitals $\phi_\mu(\mathbf{r})$ and occupation number n_i.

The representation of core states requires a large number of basis functions because of the oscillatory character of these states. Rather than simply use more basis functions, which is computationally expensive, it is more sensible to separate core and valence states. While the latter are described by basis functions, the former are included into an additional potential—the pseudopotential. In SIESTA norm-conserving Troullier-Martins pseudopotentials are used. For a norm-conserving pseudopotential the integrals of real and pseudo charge density are identical between 0 and radius r if r is bigger than some core radius r_c [96]. This is the case for all valence states and represents the norm conserving property. Additional properties of norm-conserving pseudopotentials are:

- (i) real and pseudo valence eigenvalues are identical for a particularly chosen atomic configuration;
- (ii) real and pseudo atomic wave functions are the same beyond r_c;
- logarithmic derivative and first energy derivative of real and pseudo wave function fit for $r > r_c$ [97].

In SIESTA the pseudopotential is decomposed into a local and a non-local part. The non-local pseudopotential takes the form proposed by Kleinman and Bylander [98]. The neutral-atom potential hides the local part of the pseudopotential. To screen the local pseudopotential beyond a cutoff radius

an atomic screening potential is used consisting of the electron density of the specific atom—taking into account the basis set. In other words, $V_I^{\mathrm{NA}}(\mathbf{r}) = V_I^{\mathrm{local}}(\mathbf{r}) + V_I^{\mathrm{atom}}(\mathbf{r})$.

The basis of all DFT codes are the Kohn-Sham equations [Eq. (2.1)], but the specific form of the Hamilton operator and the wavefunctions differs among codes. The Kohn-Sham Hamiltonian in SIESTA, incorporating the pseudopotential formalism, takes the form

$$\hat{H} = T[n] + \sum_I V_I^{\mathrm{KB}} + \sum_I V_I^{\mathrm{NA}}(\mathbf{r}) + \delta V^{\mathrm{H}}(\mathbf{r}) + V^{\mathrm{xc}}(\mathbf{r}), \tag{2.5}$$

where $T[n]$ is the kinetic energy operator, V^{KB} is the non-local part of the pseudopotential (see above), V^{NA} is the neutral-atom potential, δV^{H} is a modified Hartree potential, and $V^{\mathrm{xc}}(\mathbf{r})$ is the exchange-correlation potential. The index I refers to atoms. The Hartree potential is computed from the electron density difference $\delta\rho(\mathbf{r})$ between self-consistent electron density $\rho(\mathbf{r})$ and the superposition of atomic densities $\rho^{\mathrm{atoms}} = \sum_I \rho_I^{\mathrm{atom}}(\mathbf{r})$. The kinetic energy and the Kleinman-Bylander potential are determined from two-center integrals. Here, the matrix elements usually involve the overlap matrix between basis functions or possible other functions. The overlap matrix is determined from a convolution of basis functions in reciprocal space and tabulated as a function of distance before the self-consistent calculations take place. Arbitrary points between tabulated values are obtained by a spline interpolation. The remaining terms in Eq. (2.5) are computed on a real-space grid. The neutral atom potential is tabulated for each atom I at various distances. The Hartree and the exchange-correlation potentials are obtained from the charge density which is expressed from the density matrix and the basis functions at a point $\mathbf{r}$ as

$$\rho(\mathbf{r}) = \sum_{\mu\nu} \rho_{\mu\nu} \phi_\nu^*(\mathbf{r}) \phi_\mu(\mathbf{r}). \tag{2.6}$$

The Hartree potential is then calculated by solving the Poisson equation using Fast-Fourier-Transformation. The *mesh grid size* is the parameter used in the SIESTA input file to tune the fineness of the real space grid; it is specified as a cutoff energy for the maximum Fourier component of the plane wave expansion.

The basis set used in SIESTA to expand the single-particle wave functions are numerical atomic orbitals. This means that an atomic orbital $\phi_{Ilmn}(\mathbf{r})$ is the product of a numerical radial function $\phi(\Delta\mathbf{r})$ and a spherical harmonic Y as

$$\phi_{Ilmn}(\mathbf{r}) = \phi_{Iln}(\mathbf{r} - \mathbf{R_I}) Y_{lm}(\mathbf{r}_I / r), \tag{2.7}$$

where the combined index $Ilmn$ stands for atom I, angular momentum lm, and principal quantum number n. The radial function is centered around the nuclear position R_I. Multiple ζ orbitals are included to improve the basis size convergence in a variational way [95]. Polarization orbitals provide

a larger angular freedom for bond formation and are usually necessary to achieve a better approximation for the bonds observed in solids under various environments such as surfaces, defects or grain boundaries.

The most common outputs of electronic structure calculations are the k-dependent energy eigenvalues, i.e. the band structure, the density of states via a weighted sum of the eigenvalues in the first Brillouin zone,[†] and the total energy. The latter is the basis for numerous derived quantities which in the context of this work are forces and stresses for structural relaxation (see below) and formation energies for grain boundaries and surfaces (see Ch. 5). The Kohn-Sham total energy in SIESTA is

[†]The efficient evaluation of Brillouin zone integrals comprises many different techniques that also depend on particular material classes. For our calculations we use the Monkhorst-Pack scheme [99].

$$E^{\mathrm{KS}} = \sum_{\mu\nu} H_{\mu\nu}\rho_{\nu\mu} - \frac{1}{2}\int V^{\mathrm{H}}(\mathbf{r})\rho(\mathbf{r})\,\mathrm{d}^3\mathbf{r} + \int [\epsilon^{\mathrm{xc}}(\mathbf{r}) - V^{\mathrm{xc}}(\mathbf{r})]\rho(\mathbf{r})\,\mathrm{d}^3\mathbf{r} + \sum_{I<J}\frac{Z_I Z_J}{R_{IJ}}. \tag{2.8}$$

Here, $H_{\mu\nu}$ and $\rho_{\nu\mu}$ are the Hamiltonian from Eq. (2.5) and the density matrix defined in Eq. (2.4), respectively; $\epsilon^{\mathrm{xc}}(\mathbf{r})\rho(\mathbf{r})$ is the exchange-correlation energy density and the last term refers to the nuclear electrostatic potential between atom I and J with corresponding pseudoatom charges Z_I and Z_J. Due to the long-range Coulomb interaction this last term is actually further transformed. We will not present these technicalities here, the detailed transformation steps are given in Ref. [84].

The total energy calculated in Eq. (2.8) is the basis for structural relaxations and thermodynamic calculations. Usually, the atomic positions and cell parameters of the input structure originate either from experimental data or from atomistic calculations. But even if the structure is obtained from another DFT code an optimization of the internal and external degrees of freedom for a given atomic basis set, pseudopotential and exchange-correlation functional is required. The theoretical foundation for structural relaxations is the Hellmann-Feynman (HF) theorem [100, 101]. It states that the derivative of the energy for some parameter λ can be obtained from the Hamiltonian:

$$\left\langle \phi \left| \frac{\partial H}{\partial \lambda} \right| \phi \right\rangle = \frac{\partial E}{\partial \lambda}. \tag{2.9}$$

The HF theorem allows to compute for example the forces a particle experiences due to the presence of all other particles directly from the Hamiltonian—in this case λ in Eq. (2.9) is the particle position. The forces are then minimized with some optimization routine by successive displacement of the atoms. Structural relaxation thus comprises two steps: (1) a ground-state DFT calculation with force output, (2) a displacement of atomic positions according to a minimization routine. Apart from the relaxation of internal degrees of freedom, namely the atom positions, the crystal cell may be relaxed as well. Cell degrees

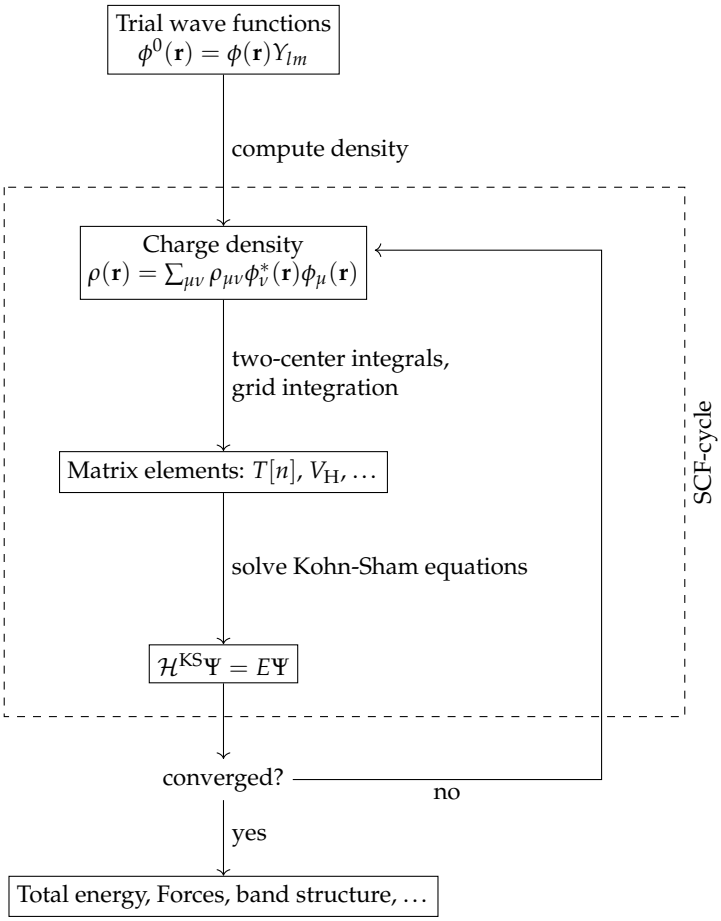

FIGURE 2.2 | Flow chart of a ground-state SIESTA DFT calculation. A large range of input parameters control individual steps with much more detail. The essence of a ground-state calculation is the self-consistency loop.

of freedom can be relaxed either by a parametrical scaling and fitting to an equation of state, or by evaluation of stresses from the Hamiltonian.

A flow chart of a ground-state SIESTA DFT calculation is given in Fig. 2.2 summarizing the governing equations described above.

2.3 TIGHT BINDING

The tight binding (TB) approach to the electronic structure problem starts by writing the Hamiltonian in terms of atomic-orbital like wave functions,[†]

$$\mathcal{H} = \sum_i |\phi_i\rangle\, \epsilon_i\, \langle\phi_i| + \sum_{ij} |\phi_i\rangle\, V_{ij}\, \langle\phi_j| \,. \tag{2.10}$$

[†]A concise and thorough discussion of the TB method is given in chapter 5 of Ref. [102]. Our notation follows that reference.

The matrix elements of the Hamiltonian in Eq. (2.10) can be obtained by different methods: using tabulated values like the well-known Slater-Koster

tables [103], via empirical data, or fitting to other electronic structure methods [104]. Multiplying Eq. (2.10) by $\langle\phi_i|$ from the left and by $|\phi_j\rangle$ from the right, the matrix elements of the Hamiltonian are

$$\langle\phi_i|\mathcal{H}|\phi_j\rangle = \epsilon_i\delta_{ij} + V_{ij}. \tag{2.11}$$

The matrix elements of Eq. (2.11) are of two types: the ϵ_i are *onsite* energies that is the potential energies of individual atoms. The second type are *hopping* matrix elements that represent the electron transfer integral between atoms i and j.

In principle, the TB model is not limited to any number of interactions and in this sense it can achieve the same precision as a DFT calculation. The price for this increased accuracy is the density of the Hamiltonian which increases the computational cost. Therefore, the idea behind the LCAO method for DFT and the TB approximation is the use of sparse Hamiltonians that can be diagonalized efficiently.

A simple and quasi-tridiagonal form of the Hamiltonian is achieved by the following assumptions:

- all ϵ_i are the same—since there is only one chemical species—and can be set to zero for convenience,
- the hopping integral V_{ij} decays fast enough that it is zero beyond nearest-neighbor distances.

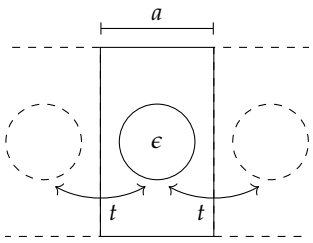

FIGURE 2.3 | One dimensional homogeneous chain.

To illustrate the TB approach, we first consider the homogeneous 1D chain (Fig. 2.3). Here, atoms are connected to each other along one space direction with a bond length a. We assume periodic boundary conditions in this direction such that the primitive cell contains one atom. To start, we consider that every atom has one orbital orthogonal to all other atoms, and that interactions are only between nearest neighbors. The onsite energy is defined to be $\epsilon = 0$, the nearest neighbor hopping term is t and all other $V_{ij} = 0$. In this case the spectrum of the 1D chain takes the following form with the 1D wave vector k:

$$E(k) = \epsilon + te^{ika} + te^{-ika} = \epsilon + 2t\cos(ka). \tag{2.12}$$

The density of states (DOS) is defined as $D(\bar{E}) = \sum_k \delta[\bar{E} - E(k)]$. Inserting $E(k)$ from Eq. (2.12) leads to

$$\begin{aligned} D(\bar{E}) &= \sum_k \delta[\bar{E} - \epsilon - 2t\cos(ka)] \\ &\approx \frac{2}{\pi}\int_{\mathrm{FBZ}} \mathrm{d}k\ \delta[\bar{E} - \epsilon - 2t\cos(ka)] = \frac{\theta(1 - |\bar{E}|/2)}{2\pi\sqrt{1 - (\bar{E}/2)^2}}, \end{aligned} \tag{2.13}$$

where we ultimately dropped ϵ because we set it priorly to zero. The 1D chain has a cosine-like spectrum with a band width of $4t$. Figure 2.4 shows the

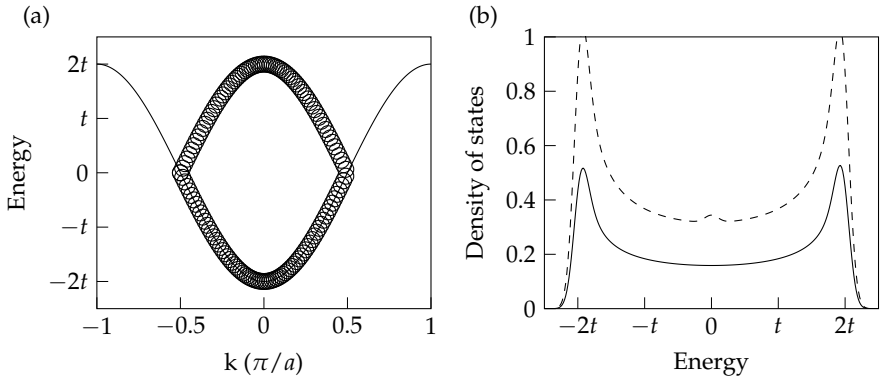

FIGURE 2.4 | Numerically calculated band structure (a) and density of states (b) in the full Brillouin zone of the homogeneous 1D chain. The dashed line represents the density of states for a system with two atoms in the unit cell, the solid line is normalized to one orbital.

spectrum together with the density of states (DOS). The DOS has two maxima, i.e. van Hove singularities at $-2t$ and $+2t$ for the occupied and unoccupied states. These singularities mark the band on- and offset. Figure 2.4 also displays the effect of making the unit cell larger—here containing two atoms instead of one. Since the real space cell is doubled in length the reciprocal space cell is half as long as in the first case. Therefore, the part of the cosine-band extending beyond the new first Brillouin zone is folded back creating a second band (open circles) and band degeneracies at the zone edges. The unnormalized DOS [Fig. 2.4 (b)] shows twice as many states as in the first case, as expected. In other words, the integrated DOS over the energy to the Fermi level yields the number of electrons per unit cell.

It is insightful to consider the 1D chain with the following modifications: (a)

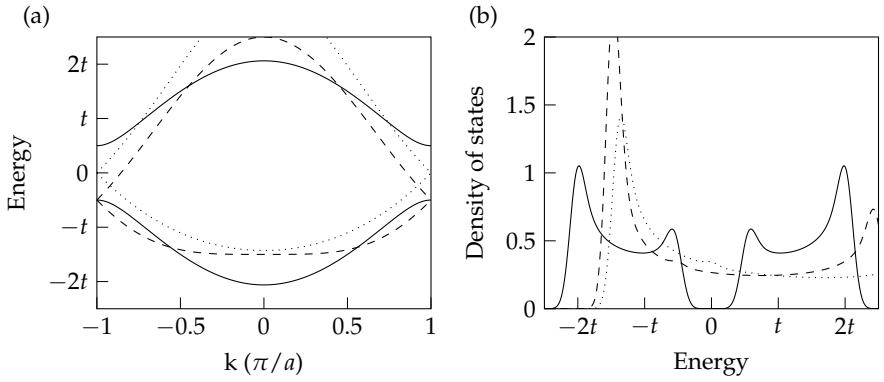

FIGURE 2.5 | Band structure (a) and DOS (b) for the following modifications of the 1D chain: different onsite energies (solid line), next-nearest-neighbor coupling (dashed line), non-orthogonal basis (dotted line).

different onsite energies $\epsilon_1 \neq \epsilon_2$, (b) couplings beyond nearest neighbors, (c) non-orthogonal orbitals. Figure 2.5 presents the band structure and the DOS for these cases. (a) Different onsite energies shift valence and conduction band rigidly and here for $\epsilon_1 = -\epsilon_2$ a band gap of 2ϵ opens. (b) Coupling beyond nearest-neighbors (here second nearest neighbors) results in an asymmetry of valence and conduction band. (c) Non-orthogonal orbitals also lead to such an asymmetry. In general, a better agreement of the TB approach compared to first-principles electronic structure methods is reached by including more interactions and non-orthogonal orbitals. Obviously, these modifications make the corresponding matrices denser diminishing the advantage of the TB method with regard to accessible system sizes. Moreover, certain technical definitions, e.g. self-doping, or bond-currents (see Ch. 3), are only strictly valid for orthogonal orbitals.

Based on the modifications of the 1D chain we now consider graphene. The influence of next-nearest neighbor interactions and non-orthogonal orbitals for graphene is illustrated in Fig. 2.6. We show the band structure along the zigzag direction of pristine graphene in a rectangular unit cell. For comparison the full band structure from a SIESTA DFT calculation with a single-ζ basis set is depicted in Fig. 2.6 (a). Bands with a dominant p_z-character are highlighted by solid lines. Figure 2.6 (b) compares these bands against the conventional nearest-neighbor TB model (TB nn), a next-nearest neighbor TB model (TB nnn), and a non-orthogonal next-nearest neighbor TB model (TB non-orthogonal). The numerical parameters of the TB models are taken from Ref. [105]. The zigzag direction contains two important points in reciprocal

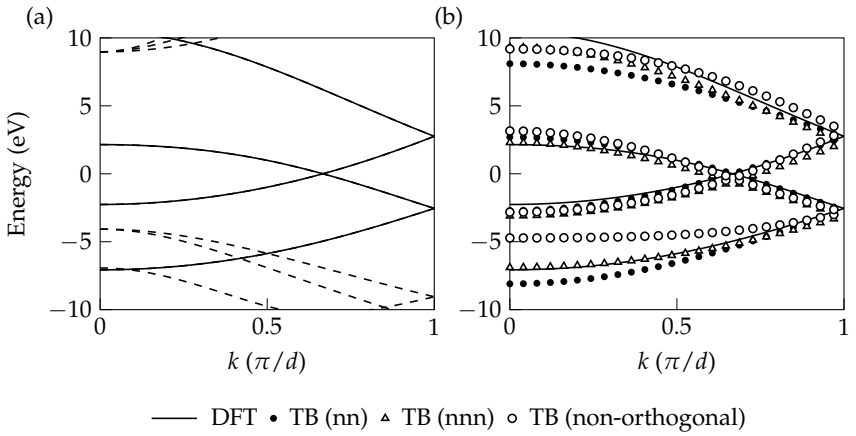

FIGURE 2.6 | DFT (a) vs. tight binding (b) band structure of pristine graphene along the zigzag direction of the rectangular unit cell. The TB models use the following levels of approximation: Nearest neighbor orthogonal (TB nn), next-nearest neighbor orthogonal (TB nnn), and next-nearest neighbor non-orthogonal (TB non-orthogonal). The dashed lines in (a) indicate bands with non-p_z-character.

space: the Γ-point and the *K*- or Dirac-point. Focusing first on the Dirac-point, Fig. 2.6 (b) shows that the TB nn model fits the DFT bands quite well. The TB nnn model, in contrast, exhibits a slight energy shift around the Dirac point, while the TB non-orthogonal model approximates the DFT bands decently. It is important that the orthogonal nearest-neighbor TB model already gives a very close fit on the Dirac point. Since low-energy electron transport occurs around this point, this result indicates that the simple TB approximation is sufficient in this energy regime.

Moving from the Dirac-point to the Γ-point shows that the TB nn model cannot capture the band dispersion properly anymore. Foremost, the nearest-neighbor interaction imposes a symmetry between valence and conduction band that is not present when including interactions from further neighbor shells. Evidently, the other two TB models, which account for second-nearest neighbors, give better approximations to the bands in the vicinity of the Γ-point. However, also these models show pronounced deviations from the DFT bands. There are several reasons for this result: The nnn and non-orthogonal model mix the band character of *s*- and *p*-orbitals resulting in effective bands that do no necessarily fit the distinct *s*- or *p*-bands of the DFT band structure. For instance the lowest *p*-band in the energy interval from $-7\,\mathrm{eV}$ to $-4\,\mathrm{eV}$ is not well captured by the non-orthogonal TB model because this model implicitly mixes *s*-bands with higher energy into an effective band. Showing only the band structures of a DFT and a TB calculation can therefore be misleading since Brillouin zone integrated quantities could be better represented by TB models that appear inadequate.

Summary Over the years, a large arsenal of methods has been developed to derive TB models from first-principles electronic structure calculations [23, 105, 106]. These methods range from fitting to band structures to the Wannier function formalism. In the last paragraphs of this chapter we have shown how simple modifications of TB parameters impact the electronic structure *qualitatively*. Already the 1D-chain exhibits the essential features: Implicit band symmetries in nearest-neighbor models are broken by including additional neighbor shells; onsite energies can shift bands rigidly or open band gaps when site-dependent; non-orthogonal TB models further evoke band asymmetries and energy shifts. These results are directly relatable to graphene. The important conclusion from these computational experiments is that a rather fine tuning of the band structure is obtained by simple means whose physical meaning is clear. More refined tuning, on the other hand, sacrifices this clarity. In this regard the choice for the nearest-neighbor p_z-orbital model in graphene is not only motivated by computational efficiency but also by the fact that such a model is physically intuitive and captures the essential electronic properties at low energies around the Fermi level. This energy region, after all, is the most relevant for low bias electron transport.

Macroscopically, Ohm's law describes the linear response of bulk materials towards an electric bias. With the ongoing reduction of the feature size of electronic components it is clear that quantum mechanical effects become significant below certain length scales and that Ohm's law is no longer directly applicable. Phrased differently, at the atomic level current flow is a non-equilibrium, quantum-mechanical many-body problem. While this sounds intimidating, for many practical purposes approximations of varying degrees can be used. These approximations simplify the quantum mechanical transport problem considerably.

In this chapter we consider the Green function formalism as a technique for transport calculations. This formalism covers a broad range of complexity from static quasi non-interacting to dynamic multiple-interaction transport. Here, however, we will not discuss the Green function formalism beyond the elementary level of quantum transport without phase or momentum relaxation. The computational analysis of electron transport in nanocrystalline graphene in this work is thus based on the *ballistic* transport approximation. As just mentioned, we neglect any inelastic contributions such as electron-electron or electron-phonon scattering.

Section 3.1 sketches a transport theory due to Landauer that establishes basic facts about ballistic transport. The Landauer approach is a prelude to the more involved Green function formalism on which the transport calculations of this work are built upon. In Sec. 3.2 we summarize important definitions and concepts of the Green function formalism from the perspective of the computer codes SIESTA, TBTRANS, and SISL used in this work. Using pristine graphene and the Stone-Wales defect as model systems we show how the relevant equations—Hamiltonians, density matrices, transport functions—are implemented.

Under non-equilibrium the transmission function can be used to generate current-voltage characteristics. These characteristics probably come closest to conventional experimental transport measurements. We present briefly in Sec. 3.3 the Landauer-Büttiker formula to obtain the current from the transmission function and the electrode Fermi distribution functions. Since bias calculations require to solve the Poisson equation self-consistently we apply them only to small-sized problems. For large scale structures like polycrystals we use bond current maps to complement the global transmission function or density of states. The concept of bond currents is outlined in Sec. 3.4 again using a Stone-Wales defect as example.

3.1 LANDAUER APPROACH TO TRANSPORT

In a 1957 paper [107], Landauer made the following point: It is generally not valid to assume a homogeneous field distribution when obtaining the conductivity—in particular if the sample contains localized scatterers. He proposed to consider electron transport based on transmission probabilities instead of the external electric field. Effectively, this viewpoint swaps the perspective: Instead of taking the response of a sample towards a macroscopic electric field and define the conductivity then as the proportionality factor between the field strength and the current, the conductivity is thought to be composed of individual microscopic channels that pass electrons with a specific probability.

In the absence of any scattering Landauer's transport picture is particularly simple: the so-called ballistic limit. Here, the conductivity is proportional to the number of modes M, i.e. transmission channels, with the quantum of conductance, $G_0 = 2e^2/h$, as a prefactor: $G = G_0 M$.[†] Every mode transmits electrons ideally which means that the transmission probability is one. An experimentally established fact, however, is that a ballistic conductor exhibits a *finite* conductivity. Apparently, this contradicts the ideal transmission of a ballistic conductor. In fact it has been realized that the *contact* resistance causes a finite conductivity in accordance with the experimental observations. The resistance can be written as: $R = h/2e^2M$. The resistance thus decreases with increasing number of modes and if only one mode is available the resistance takes the value: $R_0 = h/2e^2 \approx 12.9\,\mathrm{k}\Omega$. The number of modes is, to a first approximation, proportional to the width W[‡] and the Fermi wave length k_F of the conductor. Metals, for instance, have a low contact resistance because of their short Fermi wave lengths and corresponding large number of modes. Semiconductors, on the other hand, have considerably fewer transverse modes. This fact motivated several experiments in the 1980s on semi-conductor structures which showed conductance quantization via point contact transport measurements [110, 111].

If the transmission probability T for electrons is less than unity, for example due to reflections, the conductance formula is modified as:

$$G = \frac{2e}{h} MT. \tag{3.1}$$

Equation (3.1) is the *Landauer* equation.

The conductance is affected by the number of modes and the transmission probability. It is, however, more practical to calculate a transmission *function* $T(E)$, that is the average transmission probability per mode times the number of modes. In most of the transport calculations to follow, this function will be of keen interest. Redefining quantities is, however, not enough. We need the computational tools to calculate transmission functions from electronic

[†] Our presentation is based on chapter 2 of the book by Datta [108] and chapter 3 of the book by Di Ventra [109]. Since conceptual aspects are emphasized, mathematical derivations are left out. The cited books, especially by Di Ventra, give a more rigorous account of the Landauer approach and should be consulted for further reference.

[‡] In the 2D case. In 3D this would be the contact area.

structure calculations. The next section gives details about this process based on the Green function formalism.

3.2 GREEN FUNCTION BASED TRANSPORT

Green functions are a versatile tool in mathematical physics. In the context of transport calculations, however, we use them in a narrow sense, defined as the inverse operators of a Schrödinger-like equation. Actually, Green functions used in this way are not Green functions in the original sense within the theory of differential equations, but the name has been used for historic reasons.

The Schrödinger equation for a transport problem takes into account both the special geometry of an electrode-device setup and the associated boundary conditions. The simplest transport setup is the two terminal configuration shown in Fig. 3.1. The corresponding Hamiltonian can be written symbolically in a matrix representation

$$H = \begin{pmatrix} H_{\mathrm{L}} + \Sigma_{\mathrm{L}} & V_{\mathrm{LD}} & 0 \\ V_{\mathrm{LD}}^{\dagger} & H_{\mathrm{D}} & V_{\mathrm{DR}} \\ 0 & V_{\mathrm{DR}}^{\dagger} & H_{\mathrm{R}} + \Sigma_{\mathrm{R}} \end{pmatrix}, \tag{3.2}$$

which contains the following submatrices: the (bulk) Hamiltonians of the left electrode (H_{L}), the device (H_{D}), and the right electrode (H_{R}), the coupling

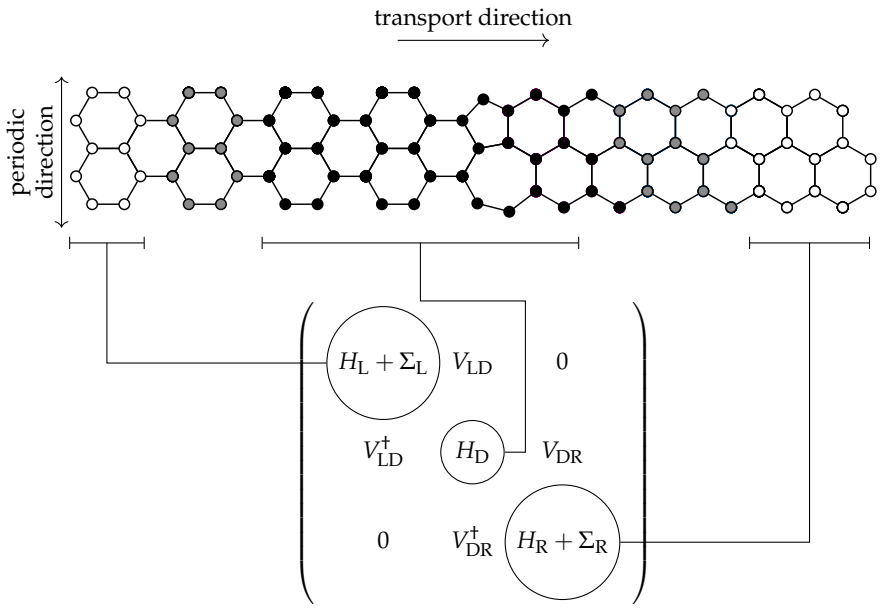

FIGURE 3.1 | Two-terminal transport calculation setup for a graphene bicrystal. The bicrystal is decomposed into electrode-device-electrode segments. Electrodes are comprised of bulk graphene while the device contains the GB. The full Hamiltonian contains the individual Hamiltonians and coupling terms as expressed in Eq. (3.2).

matrices between left/right electrode and device ($V_{\mathrm{L/R,D}}$), and the self energy matrices $\Sigma_{\mathrm{L/R}}$. Whereas the Hamiltonians and the coupling matrices have straightforward meanings, the meaning of the self-energies might not be immediately clear. The given transport problem assumes electrodes that extend semi-infinitely into the positive and negative transport direction. The effect of a semi-infinite coupling is generated by the self-energy which renormalizes the spectrum of the electrode. Since the self-energy is in general not Hermitian its eigenvalues are complex and the states injected by the electrons can be regarded as quasi-particles with finite life-time.

To illustrate the Green function transport formalism specifically, two examples are used: (i) transport in pristine graphene, (ii) transport through a Stone-Wales defect in graphene. Both examples are treated within the TB approximation and under zero bias.

Transport in pristine graphene

The band structure and DOS of pristine graphene (see Fig. 1.3, p. 4) show two prominent features: (1) No states exist at the Fermi level and (2) van-Hove singularities appear at $\pm t$, with $t = -2.7\,\mathrm{eV}$. With these features we expect that transmission is suppressed at the Fermi energy and exhibits local extrema at the van-Hove singularities. For a simple system like pristine graphene the transmission function should therefore follow the DOS closely.

Figure 3.2 shows the result of a transport calculation using TBTRANS. The transport setup consists entirely of pristine graphene with the transport direction coinciding with the armchair direction. Periodic boundary conditions are applied along the y direction. The transmission function [Fig. 3.2 (b)] confirms that no transport occurs at the Fermi level and that transmission maxima are located at $\pm t$. In Fig. 3.2 (c) the transmission eigenvalue at the Γ point is shown.

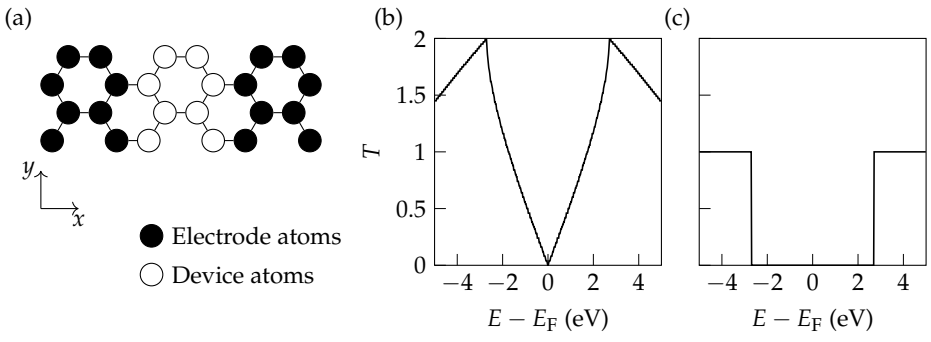

FIGURE 3.2 | Bulk transport in graphene. (a) Both device and electrode regions consist of pristine graphene. Transport is along the x direction, periodic boundary conditions apply along the y direction. (b) Transmission function averaged over k-points perpendicular to the transport direction. (c) Transmission eigenvalue at the Γ-point.

Transmission eigenvalues can be regarded as probabilities—assuming values between 0 and 1—for transport and together with the number of modes they form the total transmission. Notably, at the Γ point the transmission has a large gap of $2t$ that can easily be inferred from the DOS resolved in momentum space perpendicular to the transport direction (Fig. 3.3).

We use this specific transmission eigenvalue to illustrate how it can be computed from the building blocks of transport calculations based on Green functions, that is the Green, self-energy and spectral-density functions (see below). We choose the Γ point quite arbitrarily only to exclude explicit k-point integration that must in the general case be performed. To represent the components and operations of transport calculations we employ numerical matrices that can readily be implemented for example in PYTHON.

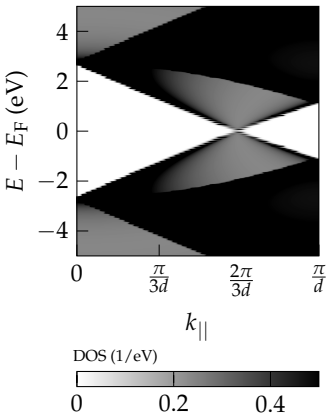

FIGURE 3.3 | Momentum-resolved DOS along the perpendicular transport direction of pristine graphene.

The two-terminal transport problem can be expressed as a quantum mechanical problem. Instead of the Schrödinger equation, however, we formulate the problem in terms of a Green function G as

$$G = [ES - H]^{-1}, \tag{3.3}$$

where E is the energy, S is the overlap matrix—in our tight binding model this is the unit matrix—, and H is the Hamiltonian. Equation 3.3 means that the Green function is the differential operator that solves the Schrödinger equation. Formulating the problem in terms of a Green function does not help us immediately. The underlying problem is that the electrodes extend semi-infinitely in the transport direction, so that the matrices are infinite. It is primarily this peculiar boundary condition that motivates the use of Green functions.

The key ingredients to approach the semi-infinite boundary condition problem are the *self-energies* $\Sigma_{L,R}$ determined for the left and right electrode, respectively. The self-energy is in general a non-Hermitian matrix, contrary to the Hamiltonian. Put in other words this means that Σ has complex eigenvalues that can be associated with states possessing a finite life time—analogous to the general complex solutions of a damped oscillator. This property is exactly what we try to model: Injection of electron states with finite life time that propagate through a device region. The self-energy is a concept that has historically featured prominently within quantum field theory [112]. From this theory we can borrow the concept of renormalization into the transport problem which expresses that the self energy renormalizes the electronic structure of the electrode to account for its semi-infinite extension. Therefore, all k-point dependence along the transport direction is integrated out and the self-energy only depends on the energy and possibly transverse k-points. To calculate the self-energy a widely used iterative procedure exists that computes surface Green functions by a so-called decimation approach [113]. Details of this method are technical and we assume in this section that such a method is

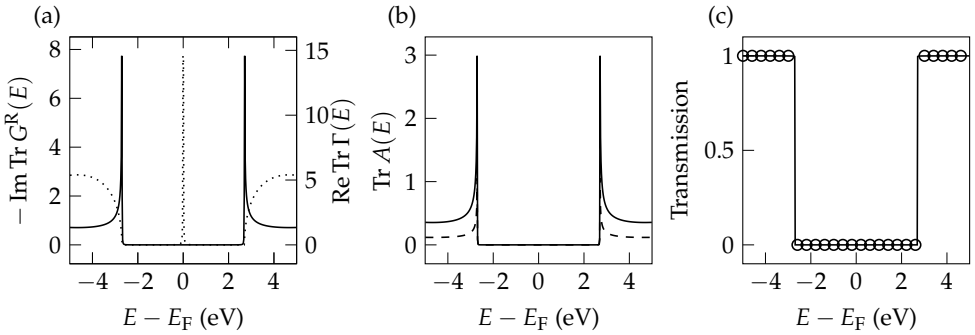

FIGURE 3.4 | Components of Green function based transport calculations. (a) Trace of imaginary part of the Green function (solid line) and broadening function (dotted line). (b) Spectral density of states from Eq. (3.7) (solid line) and from TBTRANS (dashed line). (c) Transmission eigenvalues calculated by Eq. (3.10). Open circles represent a TBTRANS based calculation.

directly available to us. With the self-energies we rewrite Eq. (3.3) as

$$G(\mathbf{r}) = [ES - H_{\mathrm{D}} - \Sigma_{\mathrm{L}} - \Sigma_{\mathrm{R}}]^{-1}, \tag{3.4}$$

with the device Hamiltonian H_{D} (see Fig. 3.1).

In Eq. (3.4) the semi-infinite boundary conditions are accounted for with the self energies and the Green function becomes finite. All physical properties of the electrode-device-electrode system are encoded in G—which we write in the following in matrix form G_{ij} for convenience. For instance, the total density of states is given as

$$\mathrm{DOS}(E) = -\frac{1}{\pi} \operatorname{Tr}\operatorname{Im}[G_{ij}(E)]. \tag{3.5}$$

Figure 3.4 (a) shows Eq. (3.5) applied to Γ point transport in bulk graphene. The DOS [solid line in Fig. 3.4 (a)] resembles the DOS obtained from a conventional electronic structure calculation. This is no surprise as we are probing pristine graphene with pristine graphene electrodes whose boundary conditions effectively establish full periodic boundary conditions.

An important ingredient to obtain the transmission function is the broadening function $\Gamma_{\mathrm{L,R}}(E)$ for the left/right electrode. This function is defined in terms of the self energy as

$$\Gamma_{\mathrm{L,R}}(E) = i[\Sigma_{\mathrm{L,R}}(E) - \Sigma^{\dagger}_{\mathrm{L,R}}(E)]. \tag{3.6}$$

It describes the coupling strength between electrodes and device. In Fig. 3.4 (a) it is plotted by a dashed line. The broadening function is peaked at the Fermi energy, which means that the coupling is weak and the energy is well localized. Since at this energy no states exist, there is no transport. On the other hand, around $\pm t$ the coupling strength increases and beyond the energy gap of $2t$

states are propagated. Similar information is provided by the spectral density of states $A_{\mathrm{L,R}}(E)$ defined as

$$A_{\mathrm{L,R}}(E) = G(E)\Gamma_{\mathrm{L,R}}(E)G^{\dagger}(E). \tag{3.7}$$

Equation 3.7 describes the coupling strength in a more general fashion which is related to spectral theory. It can, for example, also express the total density of states [see Fig. 3.4 (b)]:

$$\mathrm{DOS}(E) = \frac{1}{2\pi}\,\mathrm{Tr}\,A^{ij}_{\mathrm{L,R}}(E). \tag{3.8}$$

The actual transmission function $T(E)$ is given by the quadruple matrix product,

$$T(E) = \mathrm{Tr}\Big[\Gamma_{\mathrm{L}}(E)G^{\dagger}(E)\Gamma_{\mathrm{R}}(E)G(E)\Big], \tag{3.9}$$

that can be written in a more compressed way as

$$T(E) = \mathrm{Tr}[\Gamma_{\mathrm{L}}A_{\mathrm{R}}]. \tag{3.10}$$

The physical interpretation of the matrix product in Eq. (3.10) is not intuitive [108]. However, A_{R} can be regarded as a generalized density of states and Γ_{L} as the number of modes such that Eq. (3.10) is analogous to Eq. (3.1) from the Landauer formalism.

Eventually, we can compute the transmission eigenvalue at the Γ-point from the previously defined matrices. The result is shown in Fig. 3.4 (c) together with the transmission obtained directly from TBTRANS. The exact matching confirms that the matrices are correctly implemented. The purpose of this section was to show that the Green function technique for transport problems is no black art. The ingredients are rather straightforward and bear in most cases a clear physical meaning. Naturally, only general aspects of the Green function formalism have been discussed here. But practically all applications in this work require merely the above set of equations.

Transport through a Stone-Wales defect

Transport in pristine graphene is not spectacular. By inserting a Stone-Wales type of defect into the device region a more interesting case is investigated. Apart from examining the computational probes of transport calculations this subsection addresses general aspects of topological defects for transport characteristics that are relevant to graphene GBs as well.

Figure 3.5 (a) shows how the device region is modified compared to Fig. 3.2 (a). In Fig. 3.5 (b) the Stone-Wales defect is placed such that the symmetry along the transport direction is broken. This case is examined at last. Figure 3.6 (a) shows the DOS of the device region together with the electrode DOS. The electrode is pristine graphene and the DOS shows nothing unfamiliar so far.

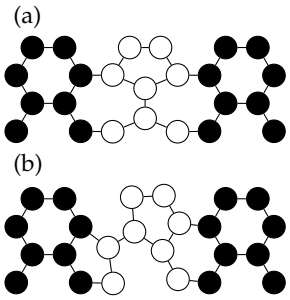

FIGURE 3.5 | Stone-Wales defects in device region. (a) The Stone-Wales defect is symmetrical along the transport direction (SW-I). (b) The defect breaks the symmetry along the transport direction (SW-II).

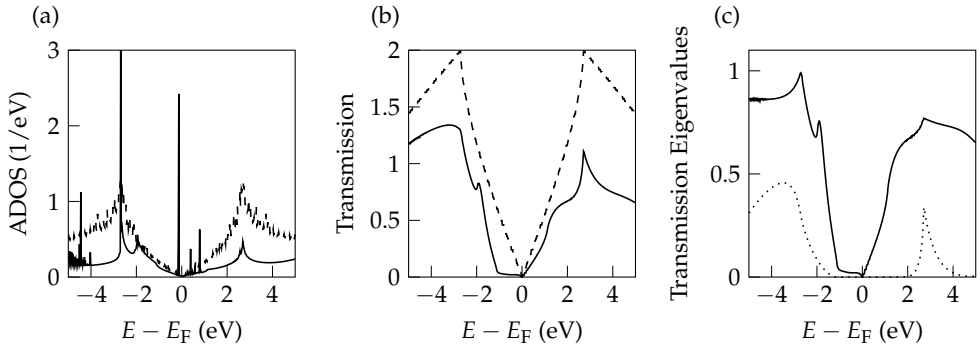

FIGURE 3.6 | Transport through Stone-Wales defect. (a) Comparison of electrode DOS (pristine graphene, dashed line) and spectral DOS (solid line). (b) Transmission function of Stone-Wales defect (solid line) and pristine graphene (dashed line). (c) First two transmission eigenvalues of Stone-Wales defect.

The device DOS, on the other hand, shows a strong resonance in the vicinity of the Fermi level indicating the defective nature of the sample. Moreover, the symmetry between electrons and holes is broken. This symmetry-breaking is a consequence of the topological nature of the Stone-Wales defect. It means that not the coordination but the connectivity among lattice sites is altered compared to pristine graphene. In other words, the sublattice symmetry is broken. This feature is also present in graphene GBs because GBs exhibit a topological nature as well (see Ch. 4). Consequently, the transmission function and the transmission eigenvalues are distorted compared to pristine graphene [Fig. 3.6 (b) and (c)] and the overall transmission is notably reduced.

Lastly, we observe how transport is affected if the Stone-Wales defect breaks the symmetry along the transport direction. Effectively, this setup means a rotation of the transport direction. Figure 3.7 compares the Green function DOS,

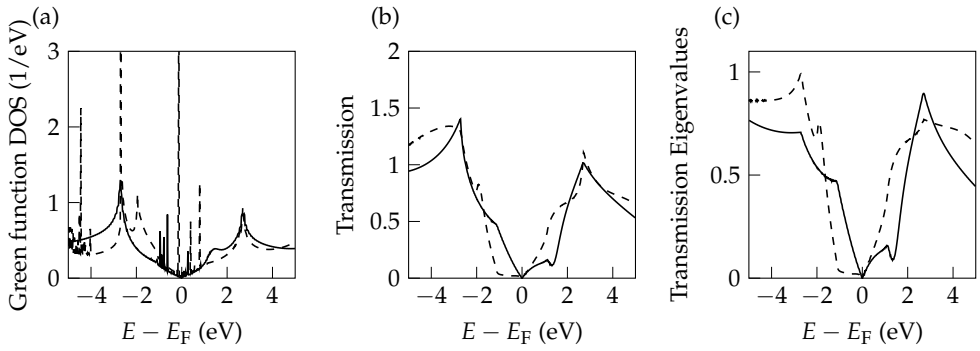

FIGURE 3.7 | Transport through a rotated Stone-Wales defect. Comparison of Green function DOS (a), transmission function (b), and first transmission eigenvalue (c) between SW-I (dashed line) and SW-II (solid line).

transmission and transmission eigenvalues of the two differently oriented Stone-Wales defects. Because the defect type has not changed the quantities share many similarities, for instance the kinks of the transmission functions. Differences occur at the exact energy location of these features. These differences are reflected in the spectral density of left and right electrode (Fig. 3.8). Until the last structure this DOS has always been identical because of the structural symmetry along the transport direction. Figure 3.8 shows that this is not the case for the setup of Fig. 3.5 (b).

In this last example the effect of transport direction on transport properties may appear trivial. It should, however, be kept in mind that transport direction can be an important factor for transport through structures with topological defects. This observation, among other considerations, motivates the use of different transport setups discussed in Ch. 7.

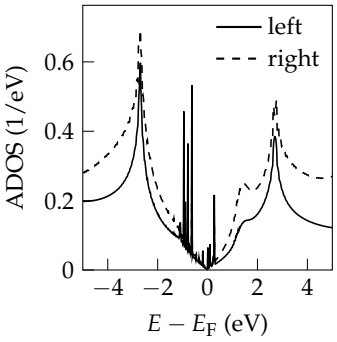

FIGURE 3.8 | Spectral density of states of left and right electrode for the asymmetric Stone-Wales defect.

3.3 BIAS CALCULATIONS

The power of the Green function technique unfolds more significantly for non-equilibrium calculations. For transport calculations this mostly translates to calculations at finite bias voltages—although thermal transport is another popular application field. We sketch here the main equations for biased transport calculations following the canonical references of the SIESTA and TRANSIESTA method [114, 115].

For non-equilibrium calculations it is advantageous to resort to density matrices (see Ch. 2). The density matrix represents the statistical ensemble of the system states. It is given in terms of the spectral density matrix and the electrode Fermi distribution function $n_F^{L,R}(\epsilon)$ as

$$\rho = \frac{1}{2\pi} \iint_{BZ} d\mathbf{k}\, d\epsilon\, A_{ij,\mathbf{k}} n_F^{L/R}(\epsilon) e^{-i\mathbf{k}\cdot\mathbf{R}}. \tag{3.11}$$

Under non-equilibrium the density matrix can be split into an equilibrium part and a correction term:

$$\rho = \rho^{eq}_{L/R} + \Delta_{R/L}. \tag{3.12}$$

Note that the non-equilibrium density matrix of the left (right) electrode contains the correction term from the right (left) electrode. The equilibrium density matrix can be obtained purely from the Green functions,

$$\rho^{eq}_{L/R} = \frac{1}{2\pi} \iint_{BZ} d\mathbf{k}\, d\epsilon \left[G_{ij,\mathbf{k}}(z) - G^{\dagger}_{ij,\mathbf{k}}(z) \right] n_F^{L/R}(\epsilon) e^{-i\mathbf{k}\cdot\mathbf{R}}, \tag{3.13}$$

with the complex energy z.

From the density matrix the energy spectrum, forces and the electron density can be calculated under non-equilibrium boundary conditions. This allows to

determine the self-consistent charge redistribution with an applied bias or to perform structural relaxation under an external bias.

The calculation of currents is similar to the calculation of conductance at zero bias. Apart from the quadruple matrix product, containing the non-equilibrium quantities, the electrode distribution functions $n_{\mathrm{F,L/R}}$ are required. The distribution functions are located at the electrochemical potential $\pm V/2$ for a given bias V. The current is therefore written as

$$I_{\mathrm{L/R}}(V) = \frac{2G_0}{e} \iint \mathrm{d}\mathbf{k}\, \mathrm{d}\epsilon\, T_{\mathrm{L/R},\mathbf{k}} \left[n_{\mathrm{F,R}}(\epsilon) - n_{\mathrm{F,L}}(\epsilon) \right], \tag{3.14}$$

where the quadruple matrix product of Eq. (3.9) has been condensed into $T_{\mathrm{L/R},\mathbf{k}}$.

3.4 BOND CURRENTS

The transmission function, the spectral density of states and the Green function based density of states are typically the most important quantities in transport studies. They give a good overview of transport characteristics because of their global nature.[†] In many cases global transport properties need to be supplemented with local transport information to have more insight into the relationship between structure and transport behavior. It is obviously important for our work to discriminate between grain and GB transport properties.

[†] *Global nature* refers to the k-point averaged quantities.

Local transport characteristics can be obtained with different approaches. Perhaps the easiest is to use a local density of states. Here the already computed density of states (spectral or from the Green function) is projected onto either position wave functions or atomic wave functions. The choice depends on the intent: the DOS resolved either structurally or in energy space. A drawback of the local density of states is the choice of appropriate projection functions. While in LCAO-based DFT calculations the projection functions are usually just the atomic orbitals, tight-binding based calculations can use different forms of projection functions such as Slater-type atomic orbitals or Gaussians. A particular choice, therefore, depends on additional factors.

Another approach is to calculate *bond currents*. Here all ingredients are available from the conventional transport calculation: the spectral density of states $A_{ij}(E)$ and the Hamiltonian $H_{ij}(E)$. In other words, no additional projection functions need to be introduced, nor a complicated extraction must be performed.

The bond current J_{ij}, associated with the left/right electrode, between orbitals i and j is defined as [116, 117]

$$J^{\mathrm{L/R}}_{ij,\mathbf{k}} = \frac{1}{\hbar} \operatorname{Im}\left[A^{\mathrm{L/R}}_{ij,\mathbf{k}} H_{ji,\mathbf{k}} - A^{\mathrm{L/R}}_{ji,\mathbf{k}} H_{ij,\mathbf{k}} \right], \tag{3.15}$$

where all quantities depend on energy. When displaying bond currents, the k-point dependence is typically integrated out over the first Brillouin zone:

$$J_{ij}^{\mathrm{L/R}} = \int_{\mathrm{FBZ}} \mathrm{d}\mathbf{k}\, J_{ij,\mathbf{k}}^{\mathrm{L/R}}. \tag{3.16}$$

Strictly speaking, bond currents are only defined for orthogonal basis sets because the orbital population for such a basis set is unambiguous. It follows that the resulting bond current is uniquely determined as well. In the general case of non-orthogonal basis functions, however, a definite orbital population depends on the choice of projection functions. The overlap matrix S_{ij} would then enter Eq. (3.15) but the equation would be invalid in a strict sense. In this work we will not deal with this complication since all bond currents are calculated for tight binding models with orthogonal basis functions. Nevertheless, if the models are extended to include buckling or defect absorption resulting in non-orthogonal basis sets, the aforementioned point must be kept in mind.

We illustrate the usage of bond currents with the already familiar Stone-Wales defect. We embed a Stone-Wales defect in a large sheet of pristine graphene [see Fig. 3.9 (a)]. The transmission function in Fig. 3.9 (b) suggests four energies of interest: (A) -1 eV, (B) -0.6 eV, (C) 0.5 eV, (D) 1.0 eV. Already from the k-averaged transmission function it is apparent that the Stone-Wales defect breaks the electron-hole symmetry that is present in pristine graphene with a nearest neighbour tight binding model (see Ch. 4 for an additional discussion of this matter).

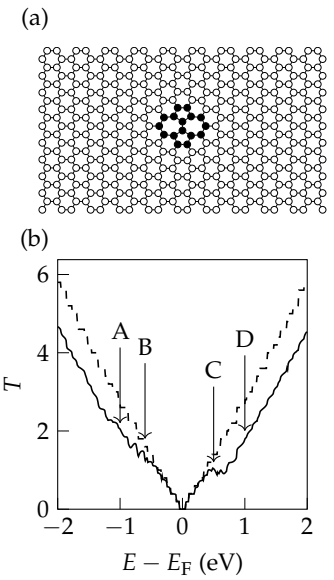

FIGURE 3.9 | (a) Stone-Wales defect embedded in a sheet of pristine graphene. (b) Average transmission function of the structure from (a) (solid line) and pristine graphene transmission (dashed line).

To investigate further Fig. 3.10 shows the bond currents corresponding to the highlighted energies in Fig. 3.9. We combine a vector current representation with the net current on each atom. This means that the line width of each arrow indicates how much current flows through this bond. Bear in mind, however, that the bond currents are obtained from an unbiased calculation and are therefore no physical currents. In Fig. 3.10 (a) the energy is -1 eV meaning that we are considering hole transport. At this energy and at lower energies the transmission slope is bulk graphene like. The transmission itself is reduced by nearly a constant. We see that major transport channels are open below and above the Stone-Wales defect. Since the defect is very localized these bulk-like transport channels are nearly unperturbed, but of course the transmission is reduced compared to pristine graphene since the middle channels are unavailable. Closer to the Fermi level, Fig. 3.10 (b) shows the bond currents at -0.6 eV, the transmission slope starts to deviate from the bulk case. The corresponding bond currents show reduced current flow along the pristine graphene channels and more localization around the Stone-Wales defect. The defect itself has low transmission. Fig. 3.10 (c) and (d) depict bond currents for electron transport. While the general transport behavior is analogous to hole transport the broken electron-hole symmetry is reflected in the details of the bond currents. Figure. 3.10 (c) in particular shows a strong localization of

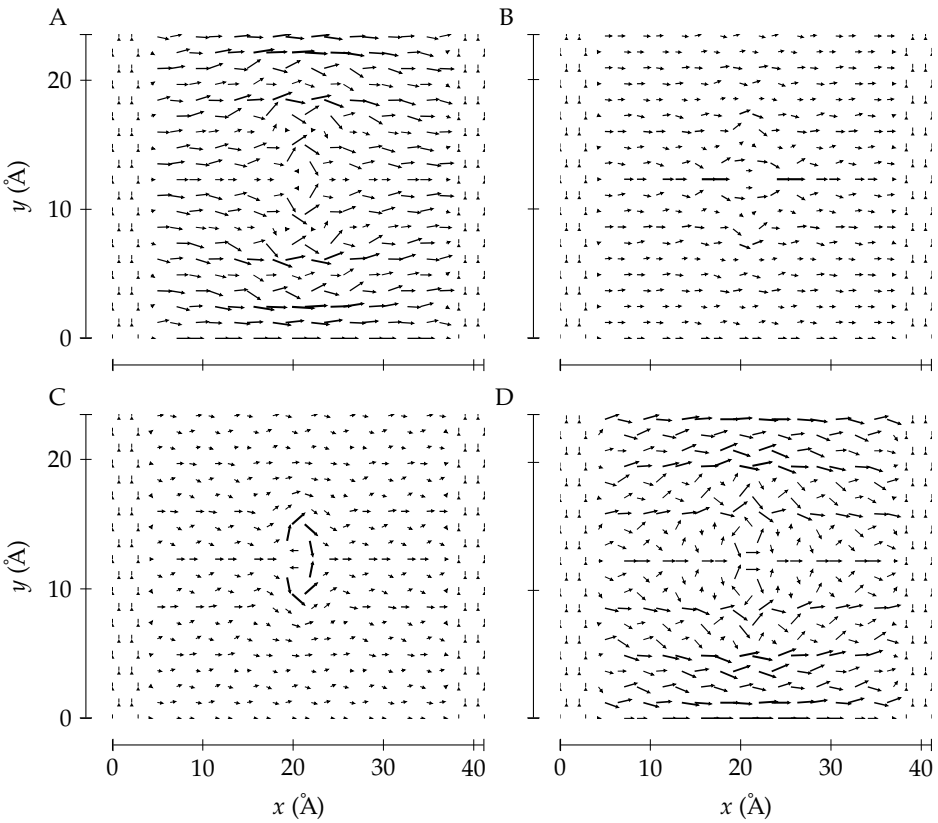

FIGURE 3.10 | Bond currents of a Stone-Wales defect at energies selected from Fig. 3.9 (b).

current flow within the pentagons of the Stone-Wales defect. At 1.0 eV current starts again to flow primarily along the pristine transport channels.

The example of transport through a Stone-Wales defect is simple-minded. Yet it shows that bond currents yield an insightful complementary picture to averaged transport quantities such as the transmission function. In many cases the bond currents can confirm or dismiss the importance of certain structural features for overall transport.

Figure. 3.10 also indicates a challenge for the analysis of transport via bond currents: an adequate visualization. The first approach for visualizing bond currents is presented in Fig. 3.10, namely utilizing vectors and possibly line width to represent current magnitude. This approach is viable for structures containing at most a few hundred atoms. In the case of the structure of Fig. 3.9 (a) this seems to be already the limit. In Ch. 7 we deal with systems containing a few thousand atoms. Using little arrows in these cases is insensible. Instead, we average over individual atoms resulting in faceted bond current maps. This approach has been developed in the work of Calogero [118] and adopted for our purposes. For the system discussed in this chapter this ap-

proach is shown in Fig. 3.11. Because the system contains only a few hundred atoms the averaged bond current map is here rather coarse.

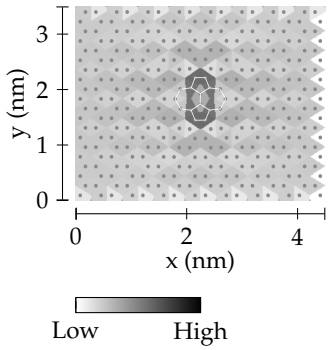

FIGURE 3.11 | Bond current map at 0.5 eV of the structure from Fig. 3.9 (a). The bond currents are averaged over atomic sites and indicated qualitatively.

Summary In this chapter we outlined quantum mechanical transport calculations based on the Green function formalism. We emphasized the practical side of such calculations from a user perspective. As example systems we used pristine graphene and graphene sheets containing Stone-Wales defects to illustrate how the pertinent equations look for specific transport problems relevant to this work. It is important for this chapter and for the rest of this work that all transport equations are represented as matrix equations. This means that wave functions are most naturally based on atomic orbitals or the tight binding approximation and that operators are used within a finite difference representation. The matrix form of the transport equations is especially useful for numerical calculations since several computationally efficient algorithms exist for various matrix operations.

Starting from the Hamiltonians of the electrode-device-electrode system we built up the equations towards the transmission function. This function, both averaged over k-points and k-point resolved, takes the central role in the analysis of transport of bi- and polycrystals in our work. To a lesser extent we regard current-voltage characteristics (see Ch. 5). Biased calculations require DFT calculations within our setup so that the Poisson equation can be solved self-consistently. While this is computationally feasible for the bicrystals analysed in Ch. 5, it is unfeasible for the polycrystals treated in Ch. 7. Instead, we complement the transmission function in polycrystals with bond current maps. These maps give insight into the relation between structural features, e.g. the GB network, and transport behavior and are particularly useful for extended structures. The basics of bond currents were shown in this chapter for a Stone-Wales defect. We showed how bond currents are calculated from the spectral density matrices and the Hamiltonian and how bond currents reveal that structural features—here the Stone Wales defect— affect the transport properties.

For the analysis of ballistic transport we therefore have primarily the transmission function, possibly at a finite bias, and bond currents. As an auxiliary quantity we have the spectral density function which is closely related to the density of states and the bond currents.

4| GRAPHENE GRAIN BOUNDARIES: PROPERTIES AND MODEL GENERATION

Due their 1D nature, graphene grain boundaries (GBs) have a distinct composition and offer different properties compared to GBs in bulk 3D materials. The reduced dimensionality also motivates a specific notation based on geometric relations of the honeycomb lattice. Such a notation is at first sight different from the coincidence site lattice (CSL) picture conventionally used to classify grain boundaries.[†]

Section 4.1 takes again the Stone-Wales (SW) defect to illustrate how non-hexagonal polygons within the atomic structure affect the electronic structure. These polygons, such as pentagons and heptagons, are the main constituents of graphene GBs. To classify graphene bicrystals this sections also introduces a specific notation commonly used in the literature. The construction of bi- and polycrystal models requires to assign an atomic structure to the interface region where the pristine graphene grain lattices interpenetrate each other. Here, a simulated-annealing-type optimization is presented that prepares all graphene GB models studied in this work. The optimization is outlined in Sec. 4.2 alongside example structures of bi- and nanocrystals.

[†]There exists a one-to-one relation between CSL theory and the graphene GB notation described here, see for example Ref. [72]. CSL theory in graphene only covers symmetric GBs and is thus not suited for an analysis of general graphene GBs.

4.1 STRUCTURE OF GRAIN BOUNDARIES

Chapter 1 has introduced graphene GBs on a phenomenological basis. In this section we look more closely at structural aspects of GBs, outline a practical notation for general graphene bicrystals, and consider the relation between atomic and electronic structure of the GB.

Grain boundaries that are only composed of n-gons and hexagons have an important property: All atoms are threefold coordinated just as in pristine graphene. The SW defect in Fig. 4.1 illustrates this fact nicely.

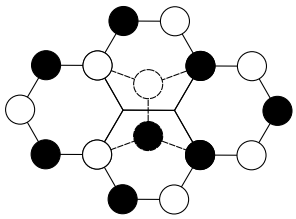

FIGURE 4.1 | A bond rotation changes the connectivity of the sublattices. A black atom has now two white and one black nearest neighbors instead of only white nearest neighbors as in the pristine system.

This defect is generated by a 90°-rotation of a carbon-carbon bond. In effect, the four hexagons sharing the initial bond are transformed into two pentagons and two heptagons.[‡] This operation does not change the individual coordination of atoms because two of the initial hexagons loose a vertex and two hexagons receive a vertex such that the total number of vertices—and thus the coordination—is unaffected compared to the pristine configuration.

If the SW defect does not change the coordination compared to pristine graphene it is perhaps not immediately clear why such a defect changes the electronic structure at all, as seen in Fig. 4.2 (b). Within the nearest neighbor TB model every atom is still connected to three other atoms, only the bond angles and bond distances have changed. However, a static hopping integral value ignores these changes. The reason for the strong impact of the SW defect or in general of the presence of n-gons in graphene is that the sublattice symmetry is broken. As stated in Ch. 1 graphene consists of *two* hexagonal sublattices.

[‡]In fact, Fig. 4.2 (a) shows two pentagons and two *octagons* due to the short x dimension of the supercell. If one or more unit cells are added along the x direction, the octagons become heptagons.

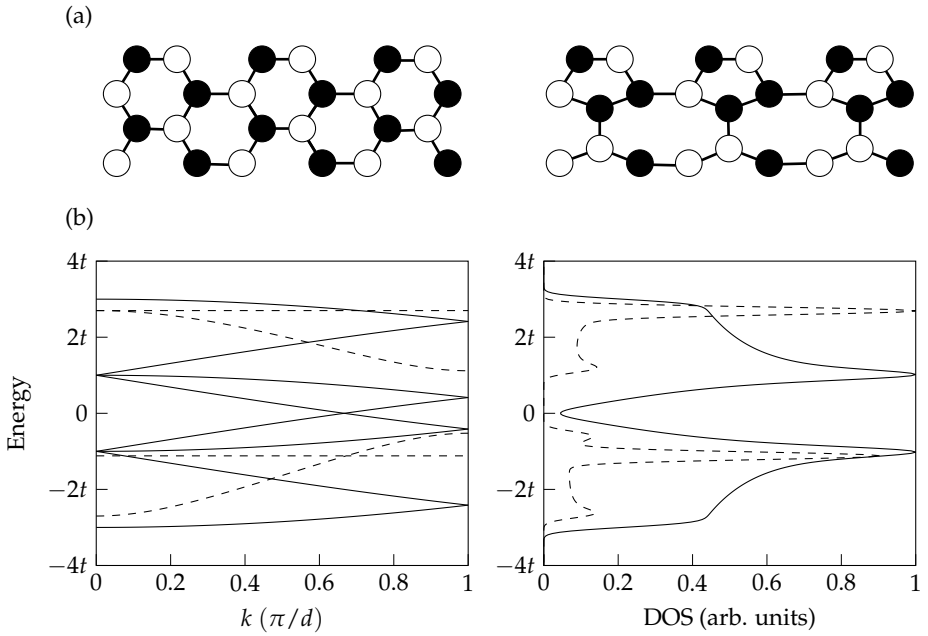

FIGURE 4.2 | Influence of a Stone-Wales defect on the electronic structure of graphene. (a) Emergence of the SW defect from pristine graphene in a 1×2 rectangular graphene cell. (b) Band structure along k_y in the rectangular first Brillouin zone and density of states over the full first Brillouin zone for pristine graphene (solid line) and the SW defect (dashed line).

Although there is only one kind of atom, namely carbon, each sublattice can be seen as containing one type of atom, ●-type and ○-type. In pristine graphene a ●-type atom is directly surrounded by ○-type atoms only. Now the SW defect breaks this symmetry, or in other words changes the topology (Fig. 4.1). This topological nature of graphene GBs has already been mentioned in Ch. 1 under the perspective of disclinations. The changed sublattice connectivity induced by n-gons is another aspect of the topological nature of these defects.

While n-gons are important to the electronic structure in graphene, a characterization of GBs solely based on the patchwork of n-gons is not useful. Instead, polycrystals are better characterized by the interface dimension and orientation relation of the grains. We consider bicrystals in the following but an application to polycrystals is straightforward, if irregular GBs are ruled out.

In a bicrystal two pristine grains are stacked next to each other. These grains define the misorientation angle θ and the interface length d. The interface is assumed to be a straight line segment of length d—the actual interface, however, might be wavy and, if straightened out, larger than d. In a supercell bicrystal model the interface length is also the repeat length since the bicrystal is extended infinitely along the GB direction.[†] It is convenient to express the misorientation angle θ measured against the x direction individually for

[†]Technically, this is achieved by periodic boundary conditions.

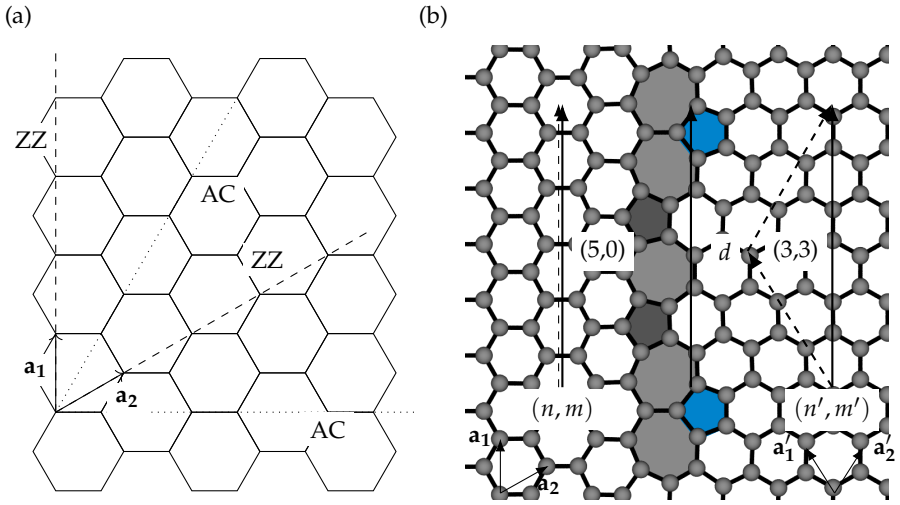

FIGURE 4.3 | High symmetry directions—armchair (AC) and zigzag (ZZ)—in the graphene lattice (a) and GB notation for a $(5,0)|(3,3)$ bicrystal (b).

each grain, that is $\theta = \theta_L + \theta_R$. With these definitions a GB notation can be established that consists of a vector for each grain that represents the interface length and the misorientation angle in terms of the graphene primitive unit cell. With the integers m, n, m', n' this notation takes the form: $(m,n)|(m',n')$.

Figure 4.3 shows this construction for a $(5,0)|(3,3)$ bicrystal. The starting point is the hexagonal graphene lattice with the armchair direction arbitrarily chosen along the x axis. The hexagonal symmetry implies that the zigzag direction lies 30° against the armchair direction and that a second armchair and zigzag direction within the first quadrant are located at 60° and 90°, respectively. All possible bicrystal misorientations lie therefore in the interval $[0°, 60°]$. An arbitrary interface line—that is a line of given angle θ and length d—can be constructed on the hexagonal grid based on an integer combination of the basis vectors of the primitive graphene unit cell:

$$\mathbf{r}^{GB}[\theta; d] = m\mathbf{a}_1 + n\mathbf{a}_2. \tag{4.1}$$

Due to the restriction that m and n are integers, it is clear that arbitrary repeat lengths and misorientation angles can only be reached approximately, leading to potentially huge super cells that would not be observed in real samples.[†] Intrinsic lattice incommensurability of the grains of a finite bicrystal evokes a mismatch strain that can be reduced by increasing the repeat length. Only in the limit of infinite repeat length, though, would this strain approach zero. In reality, the mismatch strain would be resolved at some repeat length by an additional dislocation.

[†]The epitome of this case are armchair-zigzag GBs which will be discussed at length in Ch. 5.

Equation (4.1) suggests that a graphene bicrystal can be constructed from two grains which share the vector $\mathbf{r}^{GB}$ while having different values for m and

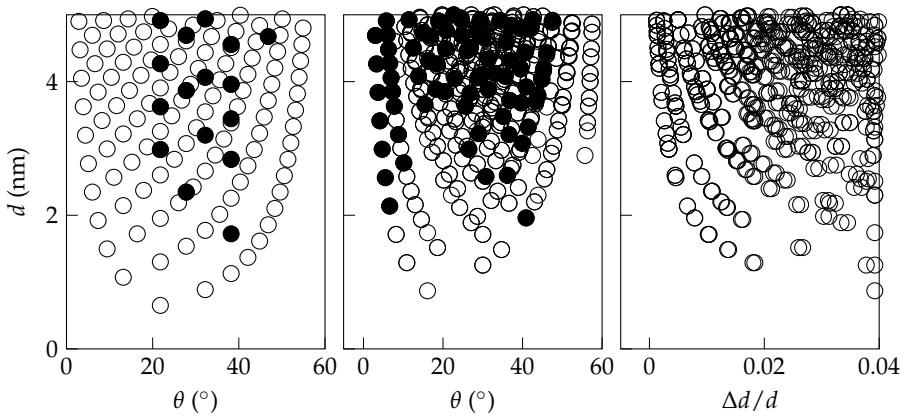

FIGURE 4.4 | Repeat lengths, misorientation angle, and mismatch strain for different GB classes in graphene following Ref. [82]. Open circles represent symmetrical bicrystals, filled circles asymmetrical bicrystals.

n. This further motivates the notation $(m,n)|(m',n')$ for arbitrary bicrystals. Expressing graphene GBs in terms of integer linear combinations of the hexagonal basis vectors has the advantage that many interesting properties of GBs can be related to particular values of these integers (see also Ch. 5). To be able to relate the integers m and n to the usually specified quantities for GBs, the repeat length d and the misorientation angle θ, the following equations are used:

$$d = d_{\mathrm{CC}}\sqrt{3}\sqrt{m^2+mn+n^2} \tag{4.2}$$

and

$$\theta = \arctan\left(\frac{2m+n}{\sqrt{3}n}\right). \tag{4.3}$$

Figure 4.4 gives an overview of the repeat length as a function of misorientation angle and mismatch strain for different classes of GBs given as combinations of the integers m, n, m', n'.

In Ch. 2 it was remarked that the electronic structure of graphene GBs is to a large extent determined by the low energy (linear) dispersion around the Dirac points. This assertion is justified by considering the band structure of pristine graphene in a rectangular unit cell with different repeat lengths along the y axis (Fig. 4.5). This setup corresponds to an $(n,0)$ grain in in a bicrystal and is representative for other grains due to the isotropic nature of the Dirac cones at low energies.

For any repetition n where $n \neq 3q$ with integer q the Dirac cone lies at 2/3 of the Brillouin zone. If $n = 3q$ the Dirac cone lies at the Γ point. This can be seen by translating for instance K' in Fig. 4.5 (a) by twice the vector from Γ to the dash-dotted zone boundary. Twice this vector is a reciprocal lattice vector of one third of the original Brillouin zone. The translation puts K' exactly at the Γ point within the one-dimensional Brillouin zone $\Gamma \to Y$. Independent

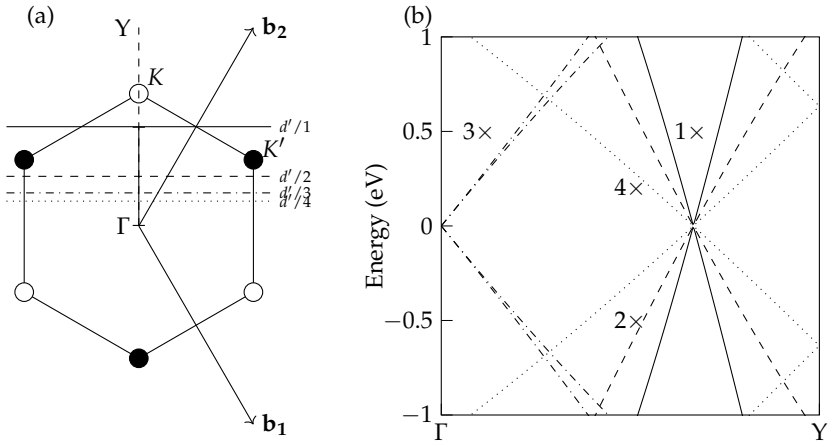

FIGURE 4.5 | Graphene band structure along k_y for multiplications of $1\times$ to $4\times$ of the rectangular unit cell along the zigzag direction. (a) Zone boundaries in the two dimensional schematic Brillouin zone. The dash type corresponds to the calculated band structures in (b).

of the location of the Dirac cone, Fig. 4.5 (b) clearly shows that the dispersion of the maximum valence band and minimum conduction band are to a good approximation linear for half of the Brillouin zone. This is sufficient since the electronic structure of a bicrystal will be determined by two Dirac cones—one associated with each grain—such that the maximum intersection distance between the Dirac cones is in the middle of the Brillouin zone.

4.2 SIMULATED ANNEALING

In this work GBs are optimized by simulated annealing. We use an in-house computer code (see Fig. 4.6) that is based on molecular static structural optimization and energy calculation [119] and a set of structure manipulations to minimize a target energy. The optimization program takes an initial atomic configuration. This system is decomposed into two groups: (1) atoms that are *not* manipulated and fixed during the first structural relaxation run, (2) atoms that can be manipulated and that are relaxed during the first molecular static optimization. Apart from the structure input the optimization code takes a set of weights for the individual structural operations and target values for atomic composition and coordination. Lastly, the number of run steps and the Boltzmann factor β are set. Every optimization begins by a molecular static structural relaxation of the initial configuration. This relaxation itself consists of two runs. The first run relaxes only atoms of group (2), the second run both groups. Additional constraints such as completely fixed atoms can be specified within the first group. The energy optimization is typically constrained by a target composition or a target coordination. For the case of graphene GBs considered in this work we aim for ideal threefold coordination. Therefore,

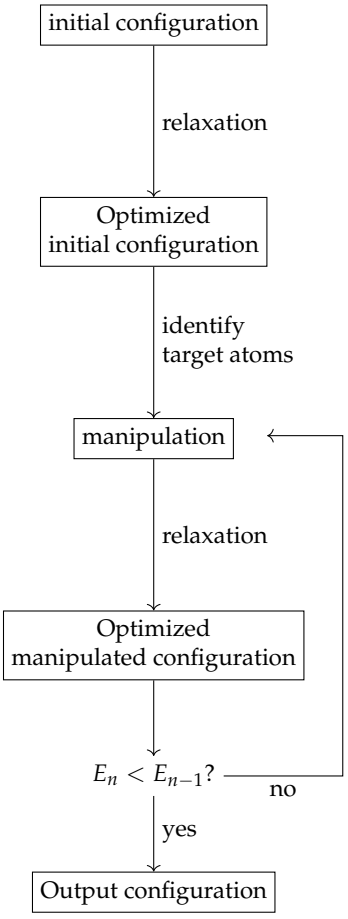

FIGURE 4.6 | Flow diagram for optimization.

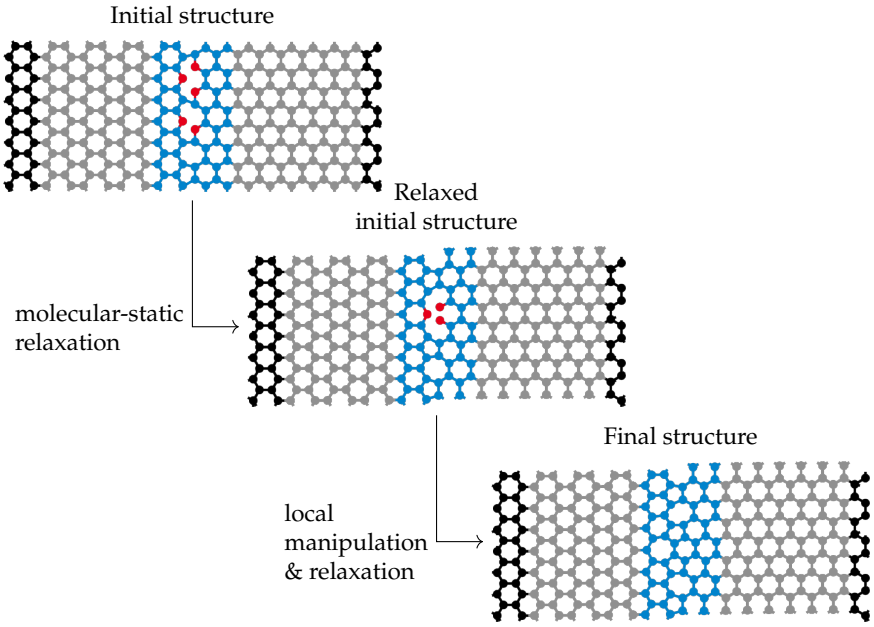

FIGURE 4.7 | Simulated annealing optimization of an armchair-zigzag grain boundary.

only the target coordination is set. The initial relaxation is succeeded by an identification of atoms which are falsely coordinated. For this identification the radial distribution function is computed. The cutoff for the inclusion of nearest neighbors is the mean between the first two peaks of the radial distribution function. This cutoff is used to determine the neighbor list of all atoms within group (2). Atoms that do not fulfill the target coordination are added into a manipulation group for the current run step. By drawing two random numbers one or more atoms of the manipulation group and one operation are chosen. The operations consist of two types: the first type comprises addition of a new neighbor or deletion of the selected atom. The second type comprises geometric operations of the selected atoms and its immediate neighborhood: mirroring, reflection, translation. After the manipulation a new molecular static run is performed from which the new energy (for example interface energy) is calculated and accepted if it is lower than the previous energy or accepted with a Boltzmann factor. If neither cases are fulfilled the structure is rejected. This process is iterated for the desired number of run steps.

To illustrate the procedure the $(7,0)|(4,4)$ system is considered. Initially, two grains of armchair and zigzag orientation are placed next to each other such that no atoms overlap. This arrangement is the initial configuration for the optimization procedure. Figure 4.7 shows that the initial structure has five atoms (marked red) that are falsely coordinated. An atom is falsely coordinated (in this example) if it has not three neighbors within a cutoff of 1.6 Å—the bulk carbon-carbon bond length being 1.42 Å. Before further

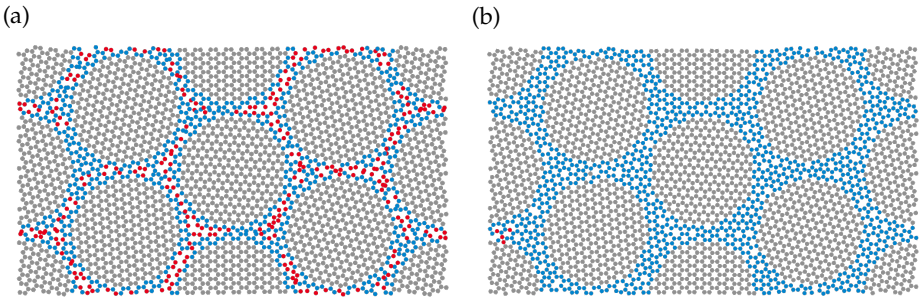

FIGURE 4.8 | Structural optimization of a graphene polycrystal comprised of hexagonally shaped grains. (a) Initial structure prior to optimization. (b) Final structure after 78 iterations representing a local minimum of the potential energy landscape. Grey atoms are kept fixed during optimization while blue atoms are manipulated and relaxed by molecular statics calculations. Red atoms represent miscoordinated atoms.

manipulations of the atomic structure an initial structural relaxation (molecular statics) is performed. There exist several choices for interatomic potentials of carbon-based materials. A rather popular is the bond-order potential by Brenner *et al.* [120]. The simulated annealing method requires high through-put molecular static optimizations for systems containing up to several thousand atoms. Additionally, we require only a minimum accuracy to ensure threefold coordination. Taking these considerations together we choose a Tersoff-type silicon-carbide potential by Erhart and Albe [121] instead of the bond order potential gaining roughly a factor of four in speed. The initial relaxation already reduces the number of miscoordinated atoms to three. Apart from the orientation relation between the grains the relative displacement along the interface determines the (initially) falsely coordinated atoms. In the current example this displacement already minimizes the number of miscoordinated atoms. The initial relaxation is succeeded by a random choice of operations that manipulate the atomic structure around falsely coordinated atoms. Since in the given example all three falsely coordinated atoms are close to each other the insertion of an additional atom already renders all remaining atoms perfectly coordinated. In this case the simulated annealing consisted of one step.

The optimization shown in Fig. 4.7 can in principle be carried out entirely manually. It serves thus, in the first place, to demonstrate the core steps during the simulated annealing optimization. A more involved example is the optimization of a polycrystal as shown in Fig. 4.8. Figure 4.8 (a) depicts the polycrystal as initially constructed. In Ch. 7 the detailed construction procedure is presented. Here, it is only relevant to see that the initial interfaces are badly connected. Blue atoms represent atoms that will be subjected to the optimization run and red atoms show miscoordinated atoms. The gray atoms, which mainly form the grain interiors, are fixed. It is evident that

the initial density of miscoordinated atoms is high since GBs are cut sharply per construction. Optimizing the polycrystal via the simulated annealing technique yields after 78 iterations the structure shown in Fig. 4.8 (b). It is noteworthy that no perfect coordination is achieved after 78 iterations. A remedy could be to simply append more iterations. On the other hand, the optimization may get stuck around peculiar structures. In any case, it may be justified to include some structural irregularities since real polycrystalline samples exhibit many irregularities themselves. In this work, however, we target perfect coordination as much as possible since we have no tight binding model of the various structural defects.

Summary We have established several simple yet important properties of graphene GBs that will indirectly appear in many of the subsequent chapters dealing with explicit transport calculations. GBs are *topological* defects and the profound impact of this fact on the electronic structure could already be demonstrated with a Stone-Wales defect. For graphene bicrystals a dedicated notation apart from the commonly used coincidence site lattice is useful. We employ the GB repeat length and the misorientation angle throughout Chs. 5 and 6. The generation of reasonable structure models is the basis for all calculations. Whereas bicrystals could be created manually, stitching together thousands of atoms in a graphene polycrystal by hand is hopeless. We have therefore sketched a simulated annealing optimization that we use in our work to ensure threefold coordination at the GB. All structures treated in Ch. 7 are generated by this method.

5| STRUCTURE-DEPENDENCE OF TRANSPORT ACROSS GRAIN BOUNDARIES

In this chapter the influence of the local atomic grain boundary (GB) structure on the electronic transport properties of graphene bicrystals is investigated. Since the repeat length and the misorientation angle only fix the macroscopic grain cells, the detailed realization of the GB is subject to some degree of freedom. In Sec. 5.1 we show different realizations of armchair-zigzag bicrystals studied in the further course of this chapter. To characterize these systems thermodynamically, we calculate the GB formation energies in Sec. 5.2. While it is established in the literature that transport gaps are determined by the geometric parameters of a graphene bicrystal, we take this ballistic transport picture to separate the transmission function into two regimes: a structure-independent gap regime and an ohmic region that depends on the structure. This distinction is presented at zero bias in Sec. 5.3. In Sec. 5.4 we supplement our calculations by current-voltage characteristics that allow, in principle, a direct comparison with experimental transport measurements. In the final section, Sec. 5.5, we try to relate structural features at the GB to prominent transport features. The results of this chapter have been published in D. Perera and J. Rohrer, *Physical Review B* **98**, 155432 (2018) [122].

5.1 MODELS

The freedom of choosing a specific atomic composition of the GB, while the misorientation relation is fixed, is the starting point of this chapter. When we employ the simulated annealing optimization (Ch. 4), we can stop at arbitrary optimization steps and extract different GB configurations. In this chapter we focus exclusively on the armchair-zigzag misorientation relation. Figure 5.1 shows the armchair-zigzag graphene bicrystal models studied in this chapter. Structure A is a well-known model discussed by Yazyev and Louie [82], while structures B and C are new structures. Bicrystal B has been generated with a method suggested by Ophus *et al.* [68] while bicrystal C is obtained from our simulated annealing optimization. The latter method is also used for the remaining structures D-G′ which have already been identified by Schusteritsch and Pickard [123] using a similar approach.

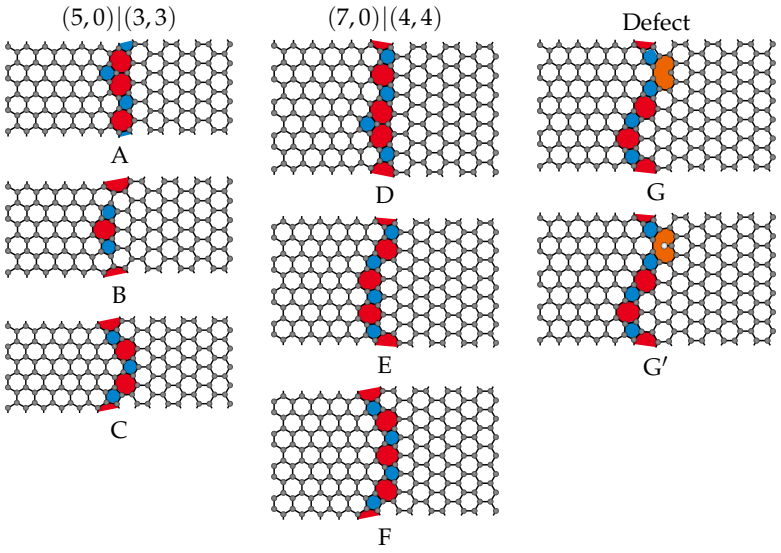

FIGURE 5.1 | Graphene bicrystal models studied in this chapter. The models are all armchair-zigzag bicrystals with a repeat length of 12.7 Å (A-C) and 17.4 Å (D-G′). Every GB consists of a distinct patchwork of pentagons (blue) and heptagons (red). The coordination defect in structures G and G′ is highlighted in orange.

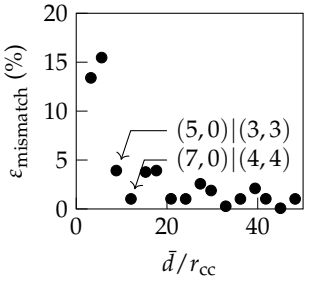

FIGURE 5.2 | Mismatch of armchair-zigzag graphene GBs.

Armchair-zigzag GBs have a mismatch strain along the interface direction due to the incommensurability of the lattices. This mismatch arises from the geometric fact that the ratio of the basis vectors of the rectangular graphene unit cell is $\sqrt{3}$. To minimize the mismatch strain, the two supercell multiples of the grains, m and m', need to be chosen such that their ratio $m/(\sqrt{3}m') \to 1$. Of course, no integers exist that make the limit exact. For the bicrystals in Fig. 5.1 $m = 5$ and $m' = 3$ for the first GB group and $m = 7$, $m' = 4$ for the second group. The second group has a smaller mismatch strain since $7/4$ is a closer approximation to $\sqrt{3}$ than $5/3$. With the GB notation introduced in Ch. 4 the armchair-zigzag systems read as $(m,0)|(m',m')$. Using this notation Eqs. (4.2) and (4.3) can readily be applied.[†] Figure 5.2 shows the mismatch strain for different combinations of m and m' in a similar fashion than Fig. 4.4, p. 40, but restricted to armchair-zigzag systems. Beyond the $(7,0)|(4,4)$ all bicrystals have a mismatch strain below 1%. However, the repeat length of the next GB with substantially lower mismatch strain than the $(7,0)|(4,4)$ GB is already too large for calculations on the DFT level. For the model construction we use the mean value of the GB length from the respective armchair and zigzag grain.

[†]Equation (4.3) has a singularity for an $(m,0)$ grain which is reflected by the grain being oriented 90° towards the x axis. Note, however, that the equivalent direction in graphene is 30° which is obtained by inserting $(0,m)$ into Eq. (4.3).

5.2 GB FORMATION ENERGIES

Since different types and arrangements of n-gons at the GB can be chosen for a given repeat length and misorientation angle, the formation energy of each system serves as a criterion of relative stability. For a periodic system we define the GB formation E^{GB} as

$$E^{\mathrm{GB}} = \frac{E^{\mathrm{tot}} - nE^0}{2l}, \tag{5.1}$$

where E^{tot} is the total energy, E^0 is the bulk graphene energy, n is the number of atoms, and l is the length of the GB .[†] As we are dealing with a two-dimensional system the formation energies have the dimension of force and not of force per length as in the more familiar three-dimensional cases.

[†]For a periodic system two GBs are present resulting in the factor 2 in Eq. (5.1).

We regard bicrystals that are not periodic perpendicular to the GB direction. To calculate the properties of a single GB two surfaces are introduced as shown in Fig. 5.3 (a). Surface states from dangling bonds are reduced by saturating the edge atoms with hydrogen. For this setup we can compute the formation energy of a single GB with Eq. (5.1) by adding surface energy terms. Here these terms are zigzag and armchair surface energies saturated with hydrogen atoms—again these are dimensionally forces. Including the terms σ^{ac}, σ^{zz} and the chemical potential of hydrogen μ_{H}, Eq. (5.1) becomes

$$E^{\mathrm{GB}} = \frac{E^{\mathrm{tot}} - nE^0 - m\mu_{\mathrm{H}}}{l} - \sigma^{\mathrm{zz}} - \sigma^{\mathrm{ac}}. \tag{5.2}$$

Table 5.1 shows the GB formation energies for all bicrystals of Fig. 5.1. We split the energies into two types: formation energies *with* strain contribution and *without* strain contribution. Formation energies calculated without strain contribution do not include the mismatch strain of the bicrystal within the surface terms. As a result, these formation energies can only be compared within a given GB family, for instance only within the $(5,0)|(3,3)$ GBs. By including strain in the surface terms a comparison among all bicrystals is possible. The data of Tab. 5.1 reveal that the mismatch strain strongly influences the formation energy. Apart from the defective structures, G and G′,

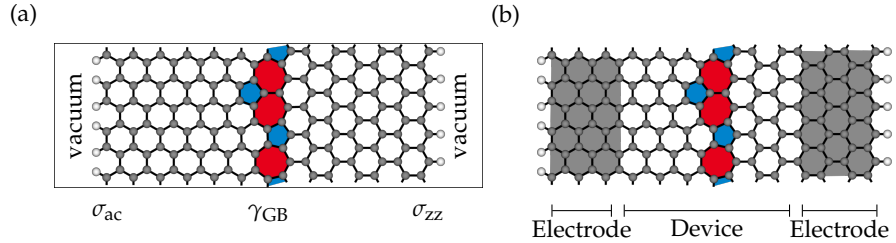

FIGURE 5.3 | System setups to calculate GB formation energies (a) and transport properties (b) of graphene bicrystals.

TABLE 5.1 | Calculated GB formation energies γ (without strain contribution) and $\tilde{\gamma}$ (with strain contribution) of all structures investigated in this work.

GB type	Structure	γ (meV/Å)	$\tilde{\gamma}$ (meV/Å)
$(5,0)\|(3,3)$	A	417	560
	B	500	650
	C	**289**	**439**
$(7,0)\|(4,4)$	D	431	433
	E	394	395
	F	310	**312**
	G	694	694
	G′	565	564

all $(7,0)|(4,4)$ GBs have a lower formation energy than their counterparts with smaller repeat length. Within a GB family meandering GBs have lower formation energies than straighter interfaces. The explanation for this result is related to the mismatch strain. A meandering interface accommodates the interface strain over an effectively longer interface line which reduces the strain per unit length and thereby the formation energy.

5.3 ZERO-BIAS TRANSMISSION

The electron transmission function T of the bicrystal models is calculated with the methods described in Ch. 3. First, we consider the transmission of bicrystal (A) in detail. This means to look at the transmission function *and* the density of states, calculated from the Green function, resolved in momentum space. Since the bicrystal is periodic only along the GB the resulting Brillouin zone is one-dimensional.

Figure 5.4 (a) shows the transmission function averaged in momentum space. Most notably, the transmission function has an energy gap of roughly 1 eV. Above the gap the transmission function rises monotonically while below the gap it is not monotonous. To better understand the energy gap in the transmission function—for short the *transmission gap*—, we consider the momentum-resolved transmission function [Fig. 5.4 (b)]. Here, two triangles can be identified.[†] We make three observations based on the schematized transmission function [Fig. 5.4 (c)]:

[†] Closer inspection reveals secondary triangles resulting from higher order Brillouin zones. This detail, however, is not regarded further.

1. The triangle peaks are separated by the energy gap size.
2. The triangle edges are rather sharp.
3. The triangles are nearly mirrored around the Fermi energy.

The first observation suggests that the total bicrystal transmission is composed of the individual grain transmissions and since both grains are rotated against

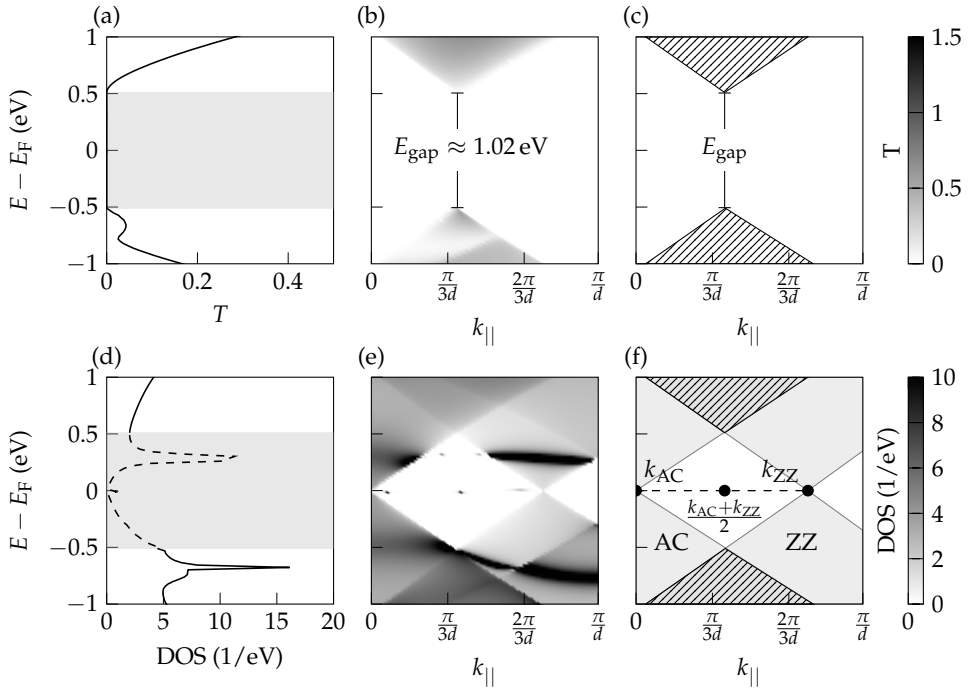

FIGURE 5.4 | Detailed transport properties of GB (A). Electron transmission function averaged in momentum space (a) and k-resolved (b). (c) Abstraction of the k-resolved transmission function. Density of states averaged in momentum space (d) and k-resolved (e). (f) Schematic DOS indicating the location of Dirac cones from individual grains and their overlap within the first Brillouin zone. The overlap region determines the transmission window of (c) due to energy and momentum conservation.

each other these grain transmissions are partially suppressed. The sharp edges and the mirrored appearance of the triangles indicate that Dirac cones might be involved.

The location of the Dirac cones of the individual grains can be observed in the Green function based density of states, given in Figs. 5.4 (d-f). Surprisingly, the k-averaged density of states shows a peak within the energy gap. On first sight this seems contradictory since no traces of this peak appear in the transmission. The k-resolved density of states [Fig. 5.4 (e)] and its schematic reduction [Fig. 5.4 (f)] help to understand what is going on: Each grain represents pristine graphene with an associated Dirac cone that we name ZZ for a zigzag orientated grain and AC for an armchair orientated grain. The AC Dirac cone is located at the Γ point of the Brillouin zone, while the ZZ Dirac cone lies at $2/3$ of the one dimensional Brillouin zone. Note, however, that due to the mismatch strain, the ZZ Dirac cone is slightly shifted from its theoretical location. The crucial point is that the AC and ZZ Dirac cones are displaced within the shared Brillouin zone. An incoming electron state, say from the AC grain, propagates into the ZZ grain, if its energy and mo-

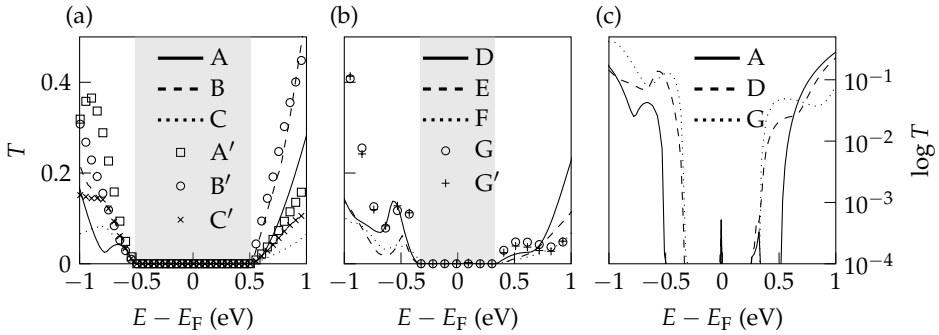

FIGURE 5.5 | Electron transmission functions for $(5,0)|(3,3)$ (a) and $(7,0)|(4,4)$ (b) bicrystals. (c) Semi-logarithmic transmission functions of selected systems. The structure labels correspond to Fig. 5.1. Primed system labels refer to additional tight binding calculations.

mentum are matched by the ZZ Dirac cone. Geometrically, this means that an *overlap* between the two Dirac cones [hatched areas in Figs. 5.4 (c) and (f)] is necessary to enable electron transport. Assuming that the Dirac cones are isotropic at low energies, the smallest energy separation, i.e. the transport gap, lies in the middle between AC and ZZ Dirac cone momentum. Now it is clear that the density of states peak within the transport gap plays no role in the transmission: Any states with these energies cannot propagate through the bicrystal. The use of energy and momentum conservation combined with the mismatch of Dirac cones to explain transport gaps has been established by Yazyev and Louie [82]. Novel aspects of this idea are discussed in the following paragraphs by considering how the local GB structure enters the transport properties.

In Fig. 5.5 we compare the transmission functions of structurally different bicrystals with the same orientation relation and two different repeat lengths. Keeping in mind that low-energy transport is governed by the overlap of the grain Dirac cones, it is expected that the transport gap size is *not* affected by the individual structure of the GB. Figure 5.5 confirms the expectation and shows zero transmission within a constant energy window determined by the repeat length. More interesting is the transport regime beyond the transport gap: Here, the GB structure has a considerable influence on the transmission. For the $(5,0)|(3,3)$ the situation above the Fermi-level—which is the more relevant region for electronic application—is straightforward. For all individual bicrystals the transmission rises monotonically, only the slopes are different. Thus, the $(5,0)|(3,3)$ bicrystals behave like ohmic conductors with different resistances. On the other hand, the situation is quite different for the $(7,0)|(4,4)$ bicrystals. Here, the transmission functions can behave monotonically [bicrystal (D)] or non-monotonically [bicrystals (E-G')]. The presence of defects [bicrystals (G) and (G')] has virtually no effect on the transmission.

The semi-logarithmic transmission plot [Fig. 5.5 (c)] summarizes nicely how the gap size is changed by the repeat length. Moreover, it shows that transmission onset is narrowly localized on the energy scale such that at the gap edge transmission really switches from off to on.

An interesting side note is the localized peak at the Fermi energy. This peak may be interpreted as leakage transmission. We do not know its origin exactly—potential causes can be the finite scattering region, strain effects or too coarse k-point sampling. However, since the leakage is small and very localized it shall not concern us further.

5.4 BIAS TRANSMISSION

From a practical perspective zero-bias transmission is mainly interesting as a material property, the zero-bias conductance. In real devices a bias voltage is applied across the sample and current-voltage characteristics are measured. To mimic such experiments on the computer, we calculate the transmission function under non-equilibrium conditions based on the non-equilibrium Green function (NEGF) formalism (see Sec. 3.3, p. 31). Figure 5.6 shows current-voltage curves of all bicrystals discussed so far. The most prevalent feature of these curves is the current suppression within the transport gap. This region is highlighted by the hatched area in Figs. 5.6 (a) and (b). From the preceding section it is clear that the zero current window size is only determined by the repeat length and not by the individual GB structure. Conversely, the current-voltage curves beyond the threshold bias are strongly affected by the individual GBs. In contrast to the zero-bias transmission function, however, the overall impression of the current-voltage curves is more homogeneous. All curves are monotonic and differ only in the slope.

A qualitative understanding of biased transport can be gained from snapshots at specific bias levels of the momentum-resolved transmission function and density of states. Figure 5.6 (c) shows the evolution of the density of states at three different bias voltages. We use as the starting point the zero-bias state already discussed in Sec. 5.3. At zero bias, i.e. at the Fermi level, the Dirac cones do not overlap and therefore no current passes. The next snapshot is taken at 0.4 V. The individual Dirac cones are displaced out of equilibrium by ± 0.2 V along the y axis. Still, there is no overlap of the Dirac cones within the energy integration region so that no current passes through the bicrystal. The final snapshot is taken at 1.4 V. This voltage is notably beyond the transport gap. As a consequence, the Dirac cones overlap within the energy interval, the energy integral is finite or with other words—current flows. In Fig. 5.6 (d) the effective overlap of the Dirac cones over the energy interval of ± 2 eV is shown—this is just the transmission function. From these pictures it can be concluded that a continuous transmission within the applied bias window is required for current to flow. This requirement is only fulfilled at 1.4 V in Fig. 5.6.

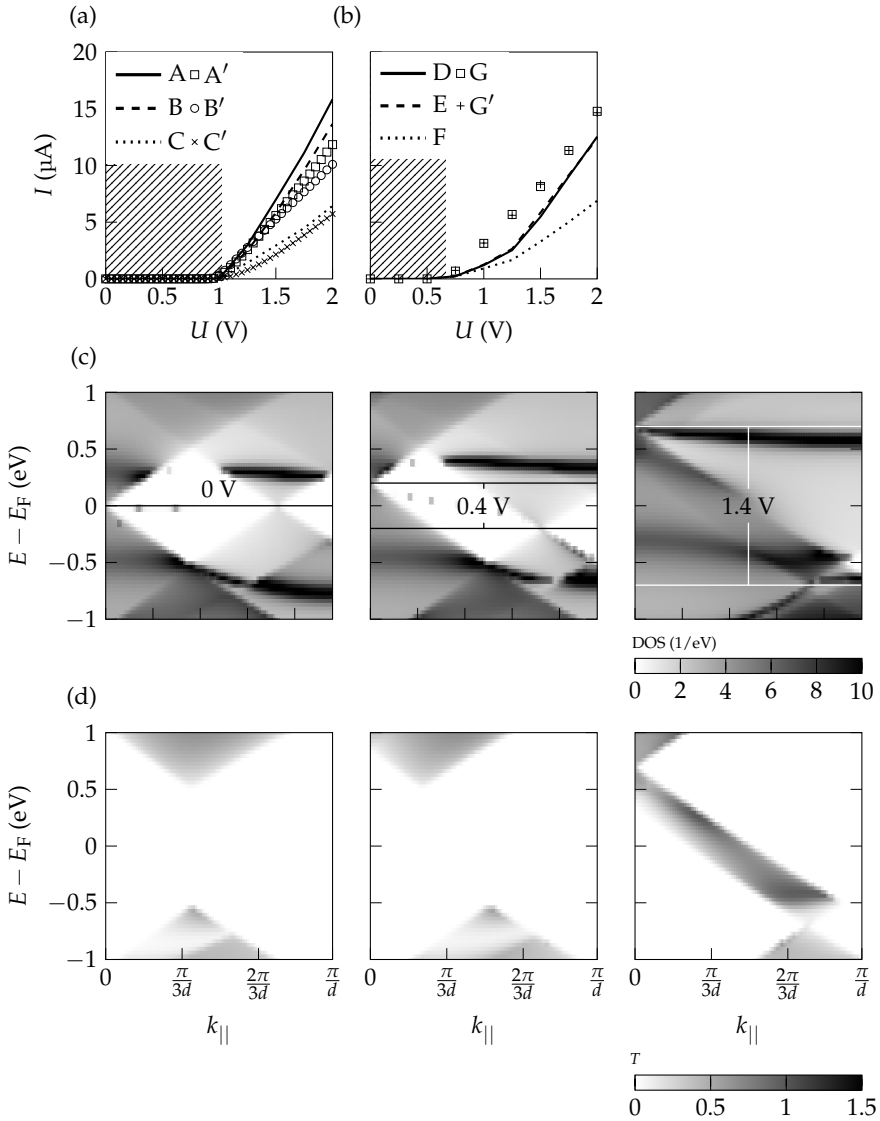

FIGURE 5.6 | Transmission under external bias voltage. Current-voltage characteristics of $(5,0)|(3,3)$ (a) and $(7,0)|(4,4)$ (b) bicrystals. Momentum resolved DOS (c) and transmission (d) at different bias voltages.

5.5 ELECTRONIC STRUCTURE AT THE GB

The transport gap size is governed by the geometric properties of the bicrystals. Outside the gap region, however, the local structure of the GB strongly affects the overall transport properties. Section 5.3 has shown that the transmission function can already look very differently for minor changes of the interface composition. The sensitivity of the transmission function is averaged out

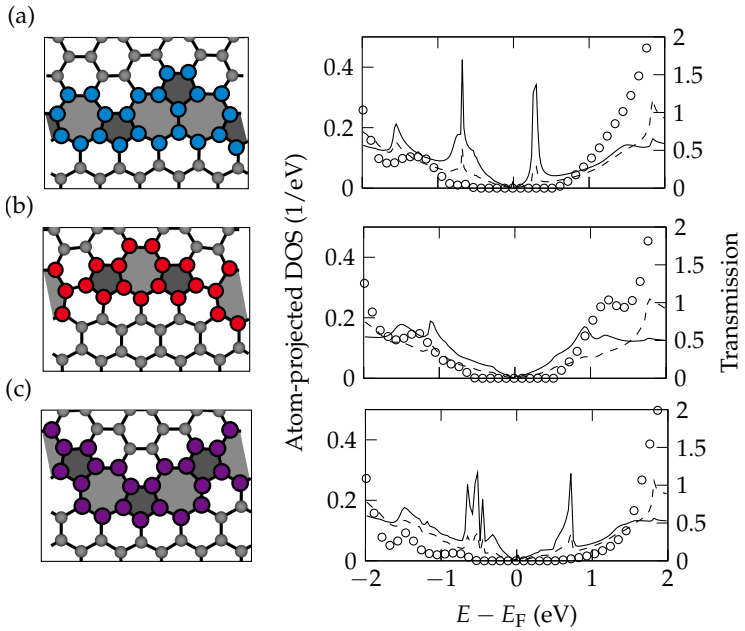

FIGURE 5.7 | Atom-projected density of states for the bicrystals of the $(5,0)|(3,3)$ type. The DOS of highlighted atoms is limited to those belonging to penta- or heptagons (solid line). The grain DOS (dashed) is obtained from all remaining atoms. Open circles represent the respective transmission functions.

when finite biases are considered and the impact of the local structure on the current-voltage characteristics is more subtle. It is still interesting to look in detail if individual features of the GB can be related to notable points in the electronic structure. To carry out such an analysis we use the DOS of the bicrystal projected onto individual atoms. Figure 5.7 shows this DOS with the following grouping: atoms belonging to the GB (colored atoms) or to a grain (uncolored atoms). The largest deviations between grain and GB DOS occurs in all cases around the transport gap edges—of course any resonances within the gap are irrelevant for transport, for instance the local peak in Fig. 5.7 (a) at 0.3 eV. There is, however, no correlation between resonances of the DOS and local extrema of the transmission function. While at first sight this may seem surprising, it must be remembered that the transmission function is obtained from the triple matrix product of the broadening matrix and the device Green function (see Eq. (3.9), p. 29). The DOS itself, on the other hand, is generated directly from the Green function. In this sense the DOS indicates possible transmission states but the coupling between electrodes and device determine actual transmission states.

Figures 5.7 (a) and (c) suggest similarities between the shape and position of DOS resonances and shared structural elements at the GB. The shared structure element is the alternation of pentagons and heptagons. In contrast

to this, Fig. 5.7 (b) presents a GB with disconnected pentagons and heptagons. Interestingly, for this structure the resemblance with pristine graphene is the strongest.

Summary While the transport gap is determined solely by the overlap of the adjacent Dirac cones and thus any local structure effects are suppressed, transport beyond the gap is notably affected by the composition of the GB. With regard to sensing application this raises the question which transport region is more relevant. From the current-voltage characteristics the region influenced by the GB structure appears ohmic. An ohmic regime exhibits rather low response factors in strain gauges comparable to pure metals. It seems therefore that the gap region would be more interesting for sensing operating on the on/off edge of the $I - V$ curve. To this end the next chapters considers the emergence and strain modulation of transport gaps for arbitrary GBs in more detail.

6| GEOMETRIC APPROACH TO TRANSPORT GAP MODULATION

In Ch. 5 we established that the detailed atomic structure of the grain boundary (GB) does not affect the transport gaps around the Fermi level. In most technological applications this is the most relevant energy regime, and we consider the properties of transport gaps in bicrystals now in detail. In particular, we address how external mechanical strain modulates the transport gap which is a key issue of piezoresistivity. Based on the ballistic transport picture from Ch. 5 the size and modulation of transport gaps are determined by the repeat length d and misorientation angle θ of the GB. In other words, the transport gap properties can be inferred by combining geometrical analysis with the bulk graphene band structure. Additionally, by computing the effect of a general two-dimensional strain on the bulk band structure, we can determine the strain-induced transport gap modulation. The major part of this chapter deals with the details of what we call *semi-analytical* method for transport gaps in graphene bicrystals. In Sec. 6.1 we survey how strain modulates the transport gap of graphene using a specific bicrystal as an example. Since the semi-analytical approach is based on transformation of both the electronic structure and the lattice geometry of graphene under strain, Sec. 6.2 presents the relevant definitions and equations. In Sec. 6.3 these definitions and equations are synthesized into the semi-analytical method to calculate transport gap modulations. Finally, Sec. 6.4 shows the application of the semi-analytical method on various bicrystals and strain states. The results of this chapter have been published in D. Perera and J. Rohrer, *Nanoscale* **13**, 7709-7713 (2021) [124].

6.1 BICRYSTAL TRANSPORT GAP UNDER STRAIN

The key ingredients to calculate transport gaps in graphene bicrystals implicitly are the position and slope of the Dirac cones associated with the individual grains. Taking the familiar $(5,0)|(3,3)$ bicrystal from Ch. 5, Fig. 6.1 (a) depicts where the Dirac cones of the $(5,0)$ grain and the $(3,3)$ grain are located within the one-dimensional GB Brillouin zone. The $(5,0)$ grain has zigzag orientation along $k_{||}$ and the Dirac cone lies at $2/3$ of the GB Brillouin zone. For the $(3,3)$ grain the Dirac cone is located at the Γ point of the GB Brillouin zone. Since ballistic transport can only occur in the overlap region of the Dirac cones, as shown in Sec. 5.3 of Ch. 5, the transport gap lies in the middle between $2/3d$ and the Γ point, i.e. at $1/3d$.[†] The size of the transport gap is determined by the slope of the Dirac cones. Since the projection of the Dirac cones onto the plane results in line segments, the transport gap is effectively given by the crossing of these lines.

[†]The given values are only ideally true. In the real bicrystal the mismatch strain displaces the Dirac cones from the ideal positions. Moreover, the slopes of the respective cones may not be identical such that the crossing point does not lie in the middle. These points are discussed in Sec. 6.2.

Under an external mechanical strain the Brillouin zones and the Dirac cones of the graphene grains are deformed. The position of the strained Dirac cones are, however, in general not at the vertices of the deformed Brillouin zone as

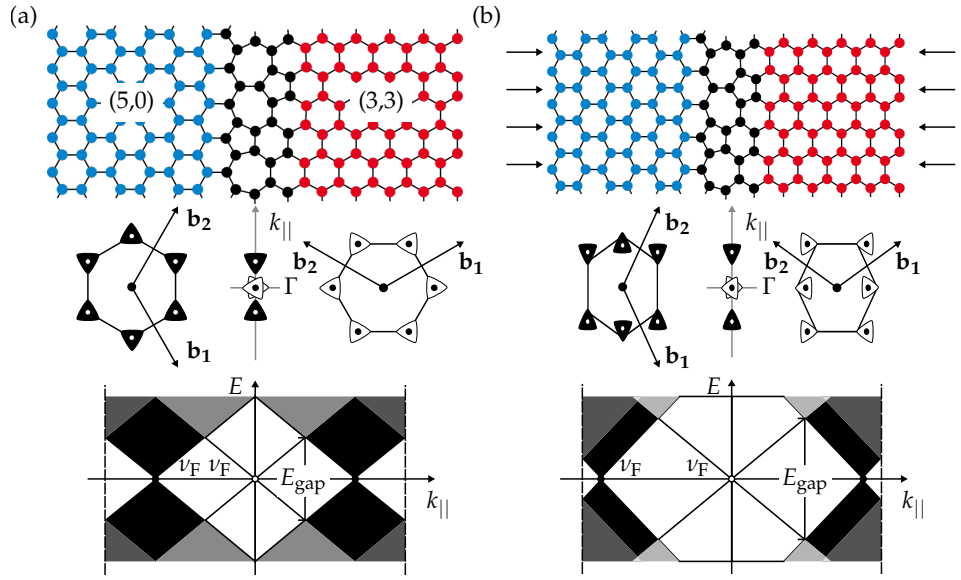

FIGURE 6.1 | Effect of uniaxial strain on an armchair/zigzag GB. (a) Unstrained bicrystal. (b) Strained bicrystal. The white and black Dirac cones correspond to the first Brillouin zone. The light gray shade indicates the Dirac cone overlap while the dark gray shade represents higher order Brillouin zone contributions.

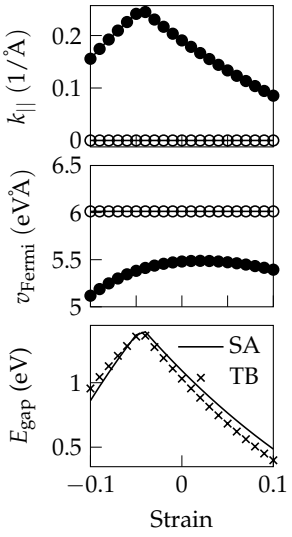

FIGURE 6.2 | Strain modulation of projected Dirac point position, Fermi velocity and transport gap of a $(5,0)|(3,3)$ GB calculated by explicit tight binding transport calculations and by the semi-analytical method presented in this chapter.

indicated in Fig. 6.1 (b). Since the transport gap is still given by the overlap of the Dirac cones, the strain modulation of gaps is just a function of the Dirac cone positions and slopes under strain. In Fig. 6.2 we show the position and slopes (i.e. the Fermi velocities) as functions of strain for the $(5,0)|(3,3)$ GB.

By applying an external strain perpendicular to the GB, the Dirac cone of the $(5,0)$ grain moves along $k_{||}$ whereas the Dirac cone of the $(3,3)$ grain remains stationary. The Dirac cone of this grain moves along the perpendicular GB direction, i.e. parallel to the strain, and thus all modulations are projected out. Similarly, the Fermi velocity is only affected along $k_{||}$ for the $(5,0)$ grain, but not as strongly as the Dirac cone position. Taken together, the transport gap modulation is only determined by the strain modulation of the $(5,0)$ grain and specifically by the modulation of the Dirac cone position along the GB BZ. This finding implies a complex but in principle trackable picture of transport in more extended polycrystalline graphene structures under strain: Transport gaps open or close, modulations of the electronic structure of individual grains might be completely projected out depending on the orientation relation and in summary transport paths *across* GBs fluctuate.

Since the transport gap modulation is determined by geometric parameters (strain direction, lattice deformation) and the electronic structure under strain, the remainder of this chapter deals with the problem how these quantities can be computed without explicit transport calculations. With such a method the gap modulation for arbitrary GBs and strains can easily be obtained.

6.2 STRAINED GRAPHENE

Electronic structure under strain

Graphene has no intrinsic band gap up to a strain of ≈29 % [45]. For most applications such high strains are unfeasible and we restrict the strain magnitude to 10 % for the following analysis—which means that no intrinsic gap opens. The position of the Dirac cones inside the Brillouin zone as well as the Fermi velocity around the Dirac points, on the other hand, change considerably even under small strain. It may seem that the Dirac cones at the vertices of the hexagonal Brillouin zone are simply shifted to the vertices of the deformed Brillouin zone. This intuitive notion, though, is incorrect (see Fig. 6.3).

Instead, the Dirac cones move away from the vertices of the Brillouin zone. Within a tight binding nearest neighbor approximation the strain-dependent position of the Dirac cones can be calculated analytically [45, 83]. For our study, however, we prefer to compute the (strain-dependent) bulk electronic structure numerically. This approach has two advantages:

1. Any modulation of the electronic structure can be modelled.
2. Any electronic structure method can be used depending on the desired accuracy.

In the context of this chapter, we employ a tight binding level description of the electronic structure and consider strain-induced modulation.

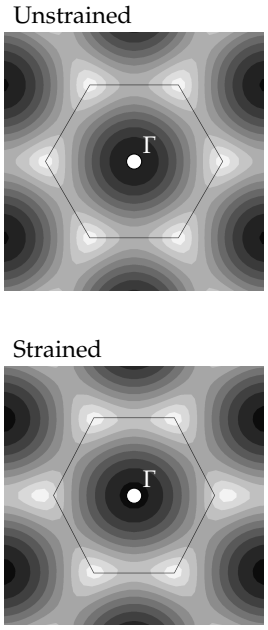

FIGURE 6.3 | Pristine graphene band structure in two dimensions. The Dirac cones do not, generally, coincide with the Brillouin zone vertices under strain.

While first-principles calculations automatically include strain effects, tight binding models require an explicitly strain-dependent hopping integral t. However, there exists no general implementation rule. Harrison proposed a strain-dependence of t as a function of interatomic distance r in relation to the equilibrium bond distance r_0 of the form: $t(\mathbf{r}) \propto (r/r_0)^{-2}$ [104]. Although this relation has been used for graphene [83], a graphene-specific dependence has been suggested by Pereira and Castro Neto [45]: $t(\mathbf{r}) = t_0 \exp[-\alpha(r/r_0 - 1)]$. This relation reproduces experimental differential current voltage curves via the parameter α. For an equilibrium carbon-carbon bond distance $r_0 = 1.42$ Å it is set to 3.37. Figure 6.4 shows a comparison of the different parametrizations as a function of interatomic distance.

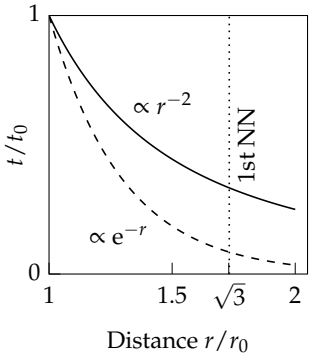

FIGURE 6.4 | Quadratic *vs* exponential scaling of the hopping integral.

Lattice deformation

Geometrically seen, applying a strain ε at an angle ϕ transforms the unit cell vectors $\mathbf{a}_i$ of the hexagonal primitive cell by the following equation (see Fig. 6.5 for definitions):

$$\mathbf{a_i}(\theta, \varepsilon, \phi) = [\varepsilon S(\phi) + I_2] \cdot [R(\theta) \cdot \mathbf{a_i^0}]. \tag{6.1}$$

In Eq. (6.1) $R(\theta)$ is a two-dimensional rotation matrix, [†] I_2 is the two-dimen-

[†] We define $R(\theta) = \begin{pmatrix} \cos(\theta) & -\sin(\theta) \\ \sin(\theta) & \cos(\theta) \end{pmatrix}$.

sional identity matrix, and $S(\phi)$ is given by (see Ref. [45]):

$$S(\phi) = \begin{pmatrix} \cos^2\phi - \nu\sin^2\phi & (1+\nu)\cos\phi\sin\phi \\ (1+\nu)\cos\phi\sin\phi & \sin^2\phi - \nu\cos^2\phi \end{pmatrix}, \tag{6.2}$$

The elastic properties along the high symmetry directions in graphene, i.e. armchair and zigzag direction, are not identical. However, their elastic moduli are very similar until 5% strain and we disregard the differences when we deal with possible mismatches between grains in polycrystals.[†] There are two more mechanical effects that are not included in our analysis of strain-dependent transport properties: Poisson contraction and buckling. The Poisson ratio in graphene is $\nu = 0.15$ [125]. Within our tight binding model we calculated that Poisson contraction affects the transport behavior not more than 10 meV and therefore we ignore it. Neglecting the buckling of the polycrystalline graphene sheet is a pragmatic decision, although real graphene is buckled at finite temperatures even as a single crystal due to unstable in-plane modes [77]. Buckling, however, drastically complicates parametrized electronic structure calculations. For large-scale tight binding calculations we have no generic parametrization of the hopping integral between sites that are displaced out-of-plane.

[†]Practically, this means that we use the mean value of the lattice constants instead of a weighted mean.

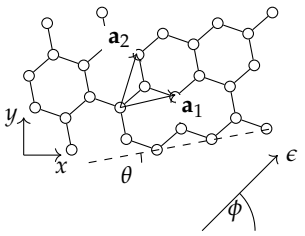

FIGURE 6.5 | Pristine graphene lattice subjected to a general strain state with strain amplitude ε and strain angle ϕ. The unit cell is rotated by an angle θ.

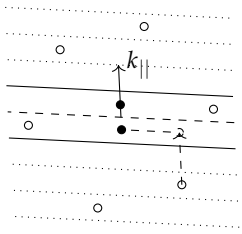

FIGURE 6.6 | Schematic illustration of the Dirac points in strained bulk graphene (open circles) and the zone folded Dirac point positions (filled circles) within the one-dimensional GB BZ. For one of the unfolded Dirac points the folding and projecting onto the GB BZ ($k_{||}$) is indicated by dashed arrows.

6.3 SEMI-ANALYTICAL METHOD FOR TRANSPORT GAP MODULATION

By calculating the electronic structure of bulk graphene strained by the strain state (ε, ϕ) and applying a rotation by θ we obtain the positions of the six Dirac points shown as open circles in Fig. 6.6. From the explicit calculation of the two-dimensional band structure of pristine graphene [Fig. 6.7 (a)] we get the dispersion around any of the Dirac cones. We assume that *all* Dirac points are equivalent for our purposes so that the particular choice of a Dirac point is arbitrary. The Fermi velocity v_{Fermi} is determined by a linear fit to the band as shown in Fig. 6.7 (c). This is valid at low energies close to the Dirac point based on the expansion to first order [35] in Eq. (6.3),

$$E_{\pm}(\mathbf{q}) \approx \pm v_{\text{F}} q + O[(q/K)^2], \tag{6.3}$$

where the momentum $\mathbf{q}$ is measured with respect to the Dirac point $\mathbf{K}$ and we set $\hbar = 1$. Thereby, the Fermi velocity v_{F} is the slope along $k_{||}$ as shown in Fig. 6.7 (c) of highest occupied valence band or lowest unoccupied conduction band around one of the Dirac points.

With this procedure we know k_{Dirac} and v_{Fermi} for bulk graphene strained by (ε, ϕ) and rotated by θ. In other words, we know the relevant quantities that determine transport gaps in bicrystals for *one* grain. The effective k_{Dirac} and v_{Fermi} within the bicrystal are fixed by the repeat length d. Therefore the Dirac points are folded into and projected onto the one-dimensional BZ, which is

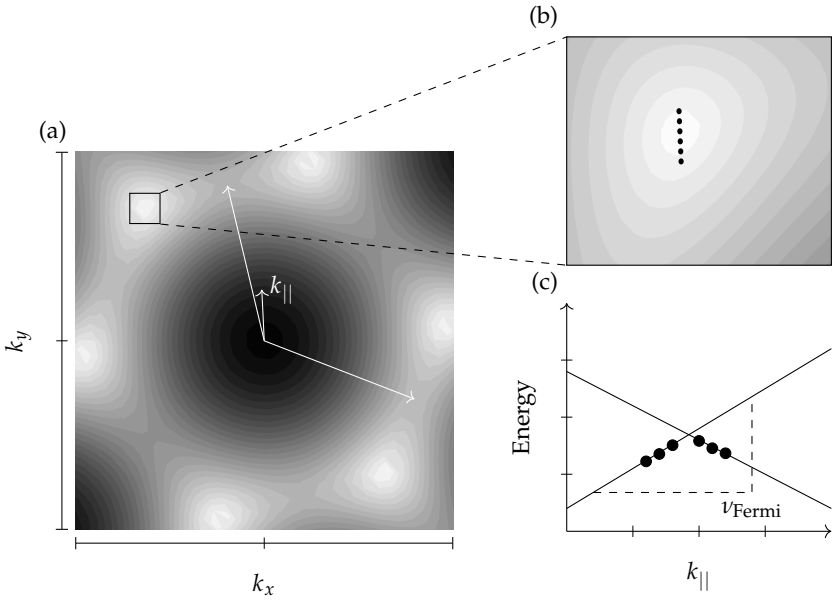

FIGURE 6.7 | Electronic structure of graphene under strain. (a) Calculated dispersion of the highest valence band in the two-dimensional BZ of the grain in Fig. 6.5 based on a nearest neighbor tight binding model. The Fermi velocity is determined within the magnified area (b) marked by the black rectangle and the band structure along $k_{||}$ (c).

depicted by the dashed arrows and the filled circles in Fig. 6.6. Similarly, the Fermi velocity is fitted along $k_{||}$ as seen in Fig. 6.7 (b) and (c).

Based on k_{Dirac} and v_{Fermi} for arbitrary ε, ϕ and θ, we obtain the following relation for transport gap momentum k_{gap} and transport energy gap E_{gap} in a bicrystal,

$$k_{\text{gap}} = \frac{v_{\text{F}}^{\text{L}}|k^{\text{L}}| - v_{\text{F}}^{\text{R}}|k^{\text{R}}|}{v_{\text{F}}^{\text{L}} - v_{\text{F}}^{\text{R}}} \tag{6.4}$$

and

$$E_{\text{gap}} = 2v_{\text{F}}^{\text{L}}(k_{\text{gap}} - |k^{\text{L}}|). \tag{6.5}$$

In Eqs. (6.4) and (6.5) we use the superscripts L and R to denote left and right grain, respectively. Of course this choice is completely arbitrary. Note that the factor 2 in Eq. (6.5) results from the electron-hole symmetry of the nearest neighbor tight binding model.

6.4 APPLICATION TO VARIOUS BICRYSTALS

The semi-analytical method presented for a $(5,0)|(3,3)$ GB in Sec. 6.2 is now applied to a selection of other bicrystals and external strains. First, we compare the transport gap modulations obtained by the semi-analytical method (solid line in Fig. 6.8) with explicit tight binding transport calculations (filled circles

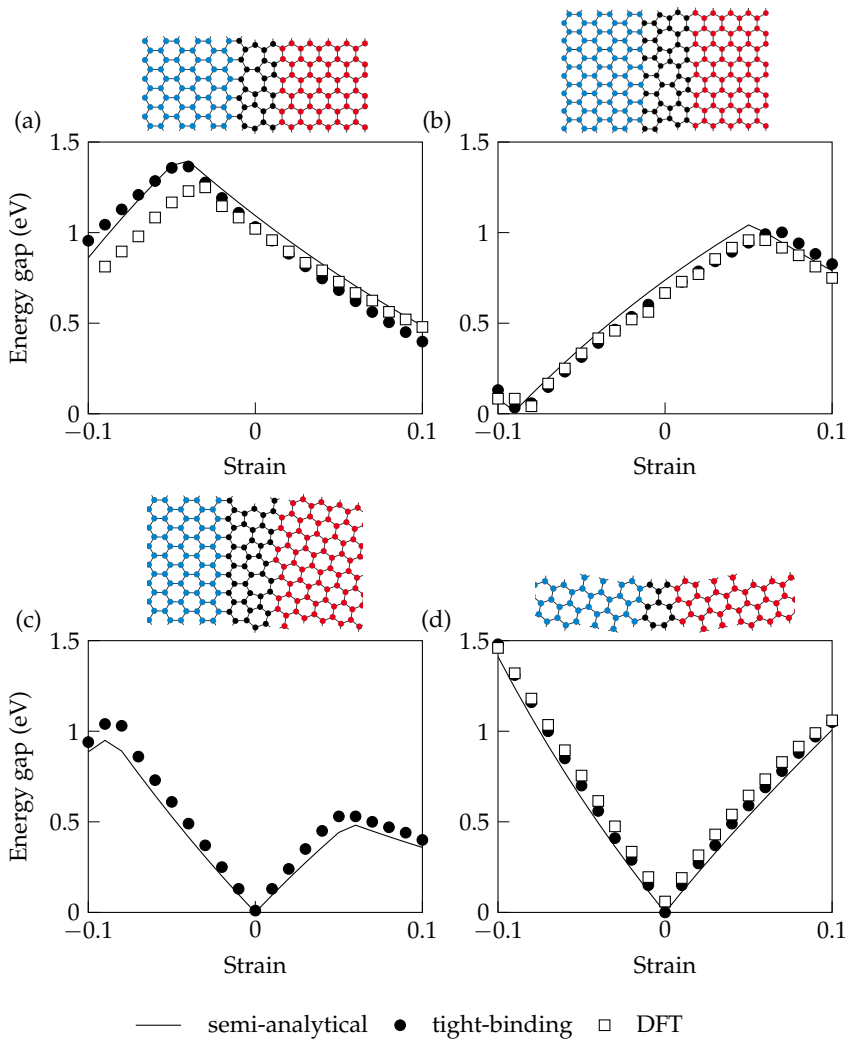

FIGURE 6.8 | Transport gap modulation of different graphene bicrystals. We compare our semi-analytical method to full transport calculations based on tight binding and DFT and results from the literature. The structure models above the modulation curves depict the region around the GB. The bicrystals in (a)-(c) are subjected to a strain perpendicular to the GB, whereas the strain angle in (d) is $\pi/4$ with respect to the x axis. DFT calculations for (c) are computationally too expensive due to the size of the full transport setup and are not included.

in Fig. 6.8). For all investigated bicrystals both methods yield identical modulation behavior. Numerical deviations arise in two forms: (1) displacements around the maxima of the transport gaps, (2) nearly constant offsets for the overall modulation. We assign these deviations to technicalities involved in the determination of the transport gap from calculated transmission functions. The calculated transmission function is sampled on a finite energy grid and we use a threshold value to determine the energy points (left and right to the

Fermi energy) below which the transmission is assumed to be zero. The absolute difference between the energy points yields the transport gap. However, we use a strain-*independent* threshold value which can systematically over- or underestimate the transport gap.

The validity of all tight binding based calculations is shown by a close agreement with DFT calculations. These calculations were conducted for all systems in Fig. 6.8 except for Fig. 6.8 (c). Here, the fully periodic electrodes lead to a very large transport system that is computationally too challenging. Differences between tight binding and DFT calculations may be attributed to the electron-hole asymmetry for the DFT calculations. This asymmetry has a more profound influence in Fig. 6.8 (a) than in Fig. 6.8 (b) and (d) and could be related to the lattice mismatch strain for this bicrystal. While there is a lattice mismatch also present for the system in Fig. 6.8 (b) it is notably lower there since the lattice mismatch strain decays with the GB repeat length d as $1/d$. The systems in Fig. 6.8 (c) and (d) have commensurate lattices.

Summary Transport gaps in graphene bicrystals arise from the overlap of the Dirac cones of adjacent grains. In this chapter we have developed a semi-analytical method that can compute transport gaps for arbitrary bicrystal misorientation relations without the need for explicit transport calculations. This method is particularly interesting for the strain-induced modulation of transport gaps. The essence of our method is not affected by any field-induced alterations: We still project the Dirac cones of pristine graphene onto the GB Brillouin and determine the gap from the resulting Dirac cone overlap. In a strained bicrystal these input parameters are merely strained as well. Strain is, of course, only one possibility of external perturbation and our method works in principle for any field-induced modulation.

Our approach also emphasizes that the seemingly difficult transport characteristics of a defective graphene structure, namely a GB, can be reduced to essentially geometrical relationships which is conceptually more elegant than brute computations.

7 | BALLISTIC TRANSPORT IN GRAPHENE NANOCRYSTALS

In this chapter we try to understand the piezoresistive response of nanocrystalline graphene (NCG) using simplified graphene polycrystal models. Our models consist of a few thousand atoms with grain sizes between 2 nm to 4 nm—close to the lower bound of experimentally observed structures. In Sec. 7.1 we present the model preparation and in Sec. 7.2 the transport setup. Sections 7.3 deals with transport characteristics of a graphene polycrystal and draws comparisons with bicrystals. To supplement the classical two-terminal transport setup we introduce in Sec. 7.4 a setup that uses a complex absorbing potential. In this configuration the scattering region can be completely encapsulated with an absorbing electrode. Such a setup does not enforce periodic boundary conditions and can be seen as an alternative approach to ballistic transport calculations for structurally complex systems. The complex transport character of a single polycrystal suggests a more statistical approach. Sec. 7.5 presents this approach for differently sized polycrystals. Finally, to address the main question of this thesis, we calculate strain gauge factors for graphene polycrystals in Sec. 7.6.

7.1 CONSTRUCTION OF SIMPLIFIED GRAPHENE POLYCRYSTALS

A common method to construct polycrystal models is by Voronoi tesselation. In two dimensions the grain centers are placed randomly in the plane ensuring a minimal distance between them. To obtain the polygon forming a grain, the grain centers are connected with each other and the perpendicular bisector of all connection lines is constructed. The intersections of the bisectors define the vertices of the desired polygons. The result of this construction is seen in Fig. 7.1.

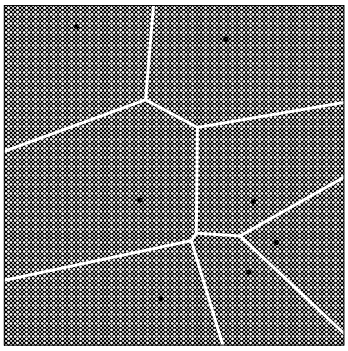

FIGURE 7.1 | Voronoi tesselation of randomly distributed points in the plane. The points can be regarded as grain centers and the surrounding polygons as grains.

While Voronoi tesselation can easily be used to construct graphene polycrystals, such polycrystals would generally have complicated GBs because the grain sizes are inhomogeneous. To avoid this complication we use a simpler approach summarized in Fig. 7.2: We place the grain centers on a rigid hexagonal grid. The Voronoi tesselation is trivial in this case yielding hexagonally shaped grains with uniform size r_{grain}. Additionally, we use a rectangular unit cell—although a hexagonal unit cell would be a more natural choice. While transport calculations for non-orthogonal cells can be performed with TBTRANS, analysis and the application of strain is easier with orthogonal cells.

The smallest rectangular cell containing fully periodic hexagons is a $\sqrt{3} \times 3$ cell in units of r_{grain}—denoted in the following simply as a 1×1 cell [Fig. 7.2 (a)]. This cell contains two seeds per unit cell. With periodic boundary conditions in the xy-plane both grains are in direct contact to their periodic images. Transport along the x direction would lead to two bulk strips where states could propagate without crossing any GB. In contrast, transport along the y direction

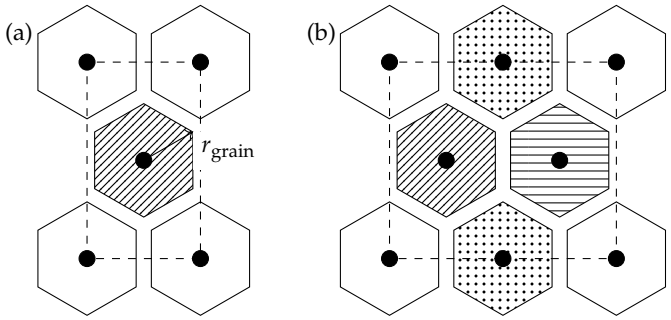

FIGURE 7.2 | Construction of a simplified graphene polycrystal. All crystallites are distributed on a regular hexagonal lattice; thus the grain size is fixed to a specific value r_{grain}. Each grain is rotated by an angle ϕ against the x axis. The interface regions are optimized by simulated annealing to enforce threefold coordination of all atomic sites.

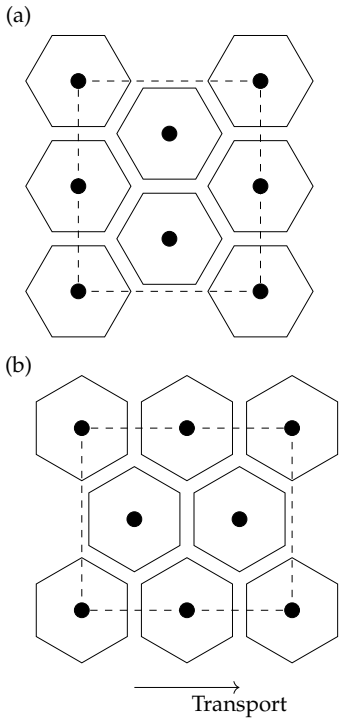

FIGURE 7.3 | Orientation of the hexagonal grains with respect to the transport direction.

resembles a mirrored bicrystal configuration with two GB segments also being mirror images of each other. In this case scattering states *would* cross GBs. Keeping the x direction as the transport direction a simple fix is to tile the unit cell. In this sense, the minimum cell size is a 2×1 cell [Fig. 7.2 (b)].

Based on the 2×1 cell the construction of the polycrystal proceeds as follows: A bulk graphene seed is placed on the four seed sites of the macroscopic cell. While the grain size is fixed by the choice of the macroscopic cell, the rotation angle of individual grains is a free parameter. We focus on the two cases shown in Fig. 7.3 for the transport analysis. To identify the atoms in the interface region, we loop over all atoms and classify atoms that are close to more than one grain center within a tolerance as interface atoms. The interface regions are then optimized with the simulated annealing procedure outlined in Ch. 4.

7.2 TRANSPORT SETUP

The transport setup for graphene polycrystals is not conceptually different to the setup for bicrystals. After initial preparation and optimization of the polycrystal, it is attached to bulk graphene electrodes and the resulting interface between bulk and polycrystal is optimized subsequently. The optimization target is again threefold coordination of all atoms.

After the optimization the transport models are rescaled to a carbon-carbon bond length of 1.42 Å which is in line with the conventionally used tight binding transfer integral [23]. Transport calculations themselves are performed in the same fashion as for bicrystals (see Ch. 5).

The interface between electrodes and scattering region cuts through the polycrystal grains and creates artificial boundaries. Most of the scattering states are therefore injected directly at such a boundary. This situation is more pronounced for smaller grain sizes where a significant portion of the scattering region consists of this additional interface.

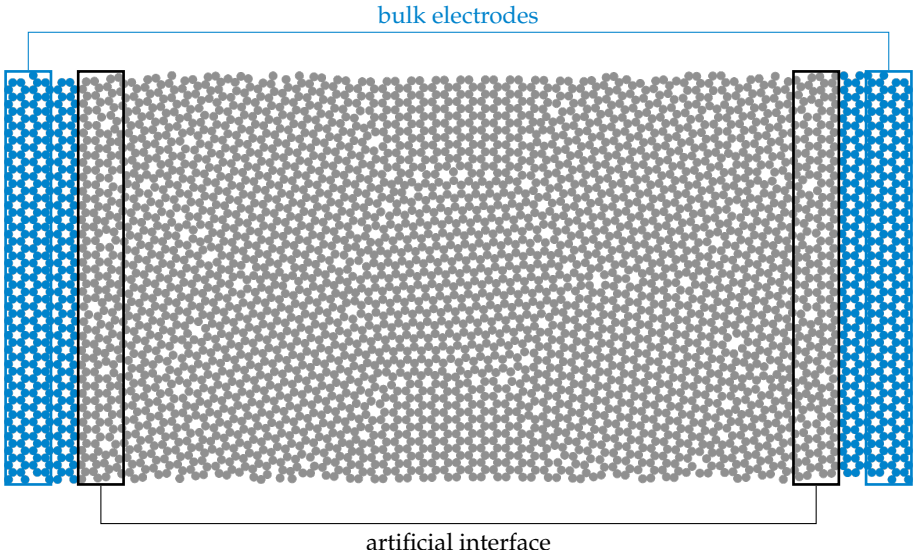

FIGURE 7.4 | Two-terminal transport setup for a graphene polycrystal. The electrodes are bulk graphene. The grain diameter is chosen to closely match the electrode dimension so that interface strain is minimized.

Figure 7.4 shows a polycrystal at the largest grain size investigated in this chapter. After structural optimization the grain orientation deviates from the initial orientation angle within a few degrees. Additionally, a slight curvature of GBs emerges.

7.3 TRANSPORT CHARACTERISTICS OF A GRAPHENE POLYCRYSTAL

We survey the transport characteristics of one polycrystal in detail. This polycrystal has the orientation indicated in Fig. 7.3 (a). Figure 7.5 shows the transmission function and the DOS per atom of this polycrystal. For reference the bulk transmission function and DOS are shown alongside (dashed lines in Fig. 7.5).

Generally, the polycrystal transmission is more reduced and noisy compared to the bulk. The electron-hole symmetry, present in pristine graphene for a nearest-neighbor TB model, is broken. The noisy transmission function results mainly from single scattering sources, i.e. states injected at the artificial GB. In an experimental setting this effect would be smoothened out. Such an effect could be achieved by phase relaxation via additional virtual probes. The implementation of this method, however, is not straight-forward and adds a considerable computational cost to transport calculations. Even without smoothening it can be seen that the transmission function is monotonically rising above the Fermi level. No clear energy gap region can be identified. This result suggests that transport *along* GBs is strong enough to create notable electron transfer.

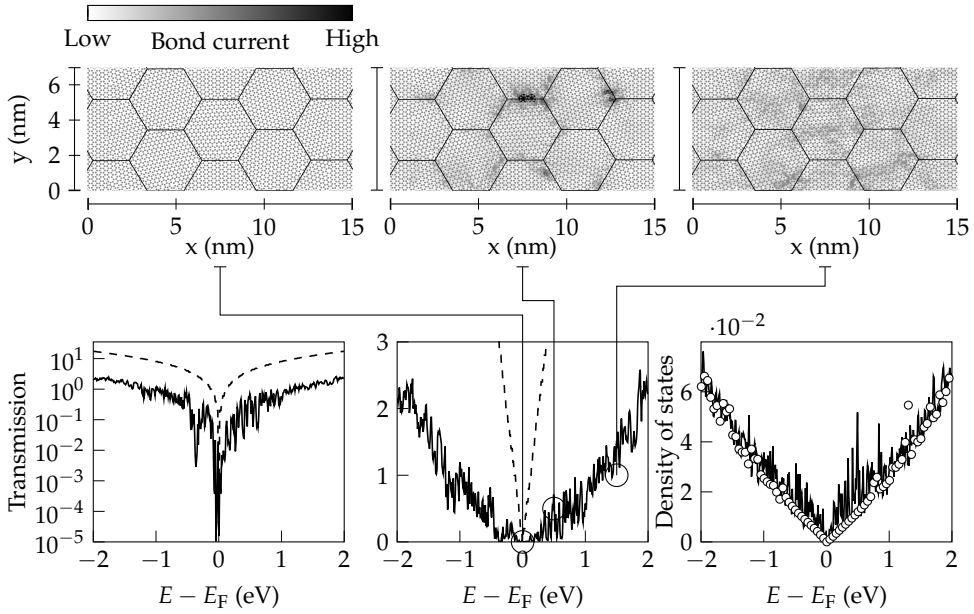

FIGURE 7.5 | Transport properties of a selected polycrystal model of Fig. 7.11. The transmission function (semi-logarithmic and regular y axis) of polycrystal (solid line) and pristine graphene (dashed line) are compared. The density of states per atom is shown for the polycrystal (solid line) and pristine graphene (white circles) alongside. Additionally, color maps of zero-bias bond currents at specific energies above the Fermi level are presented.

A closer inspection of the semi-logarithmic transmission function together with color maps of zero-bias bond currents at selected energies shows additional details: At the Fermi level there is no conducting channel, thus the semi-metallic nature of bulk graphene is also present in the polycrystal. At energies below 0.5 eV the transmission is very low but rather noisy, so that current leakage at these energies is expected. At 0.5 eV the bond-current map shows enhanced transmission at the GBs. Compared to the higher energy regime at 1.5 eV this suggests that transport is initiated through the GB network at first. With increasing energy more transport channels are opened including grain interiors. At energies beyond 1.5 eV no detailed transmission paths can be discriminated but both GBs and grain interiors participate in transport. Therefore, the transmission function rises almost monotonically above this energy entering an ohmic regime. The total DOS [Fig. 7.5] confirms the asymmetry between conduction and valence band not present in the bulk. However, the polycrystal DOS resembles the bulk DOS more closely than the transmission functions. Apparently, the total k-averaged DOS gives only a rough idea about the electronic structure of the polycrystal.

A more insightful DOS analysis is presented in Fig. 7.6. Here, the DOS is split into different classes of atoms [Fig. 7.6 (a)]. The polycrystal DOS consists of the grain DOS and the GB DOS. In general, the most pronounced differences

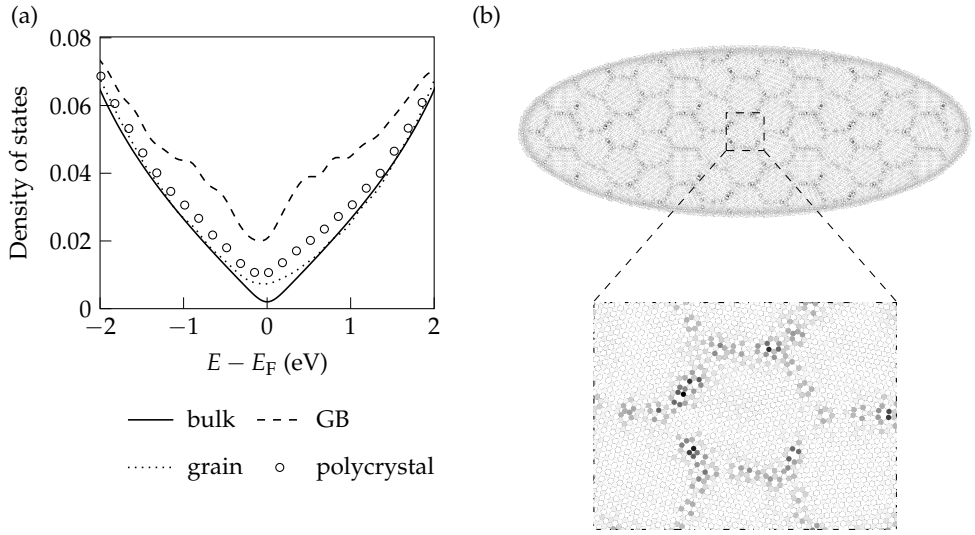

FIGURE 7.6 | Density of states analysis of a graphene polycrystal. (a) The DOS is resolved for different groups of atoms based on the classification during structure generation. (b) DOS as a means to identify GB atoms. Coloring corresponds to the DOS deviation compared to pristine graphene.

between bulk and polycrystal DOS are within ± 1 eV of the Fermi level. This energy window is usually the most relevant for sensing applications and electronics in general. The GB DOS exhibits the largest deviations from the pristine graphene DOS and it is also responsible for the broken electron-hole symmetry. This is expected remembering that topological changes from carbon hexagons break this symmetry (see Sec. 2.3, p. 18) and GBs typically contain large arrays of pentagons and heptagons. The grain DOS, in consequence, fits the pristine graphene DOS quite well—especially beyond ± 0.5 eV which indicates that the grain size is sufficiently large. Deviations at smaller energies are therefore traces of the grain edges. The DOS of the complete polycrystal naturally resembles more the grain DOS than the GB DOS due to the significantly higher fraction of grain atoms. But the GB impacts the polycrystal strongly. It breaks the electron-hole symmetry of the overall structure and provides a notable defect density of states.

Figure 7.6 (b) emphasizes an important observation, present in virtually all polycrystal models: The GB consists not exclusively of atoms that possess a GB-like electronic structure. This finding means that there are *bulk* holes that can connect the different grains and in consequence additional transmission paths are opened. To some extent this can be seen in the right-most bond current map of Fig. 7.5.

7.4 INTERLUDE: TRANSPORT WITH COMPLEX ABSORBING POTENTIALS

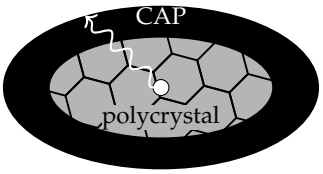

FIGURE 7.7 | Schematic depiction of a complex absorbing potential surrounding a polycrystal. States injected into the polycrystal leave the device reflectionless.

A complementary perspective on transport in extended structures such as polycrystals is the investigation of *finite* samples. In such a transport setup no artificial contact interfaces are introduced such as those described in the two-terminal configuration of Sec. 7.3. To obtain physically meaningful results, however, states injected within the sample need to leave it reflectionless. To ensure a reflectionless boundary the application of complex absorbing potentials (CAPs) is convenient (Fig. 7.7).

We use a formulation suggested by Xie *et al.* [126] where the position-dependent complex absorption potential $W(x)$ takes the form

$$W(x) = \frac{i\hbar^2}{2m}\left(\frac{2\pi}{\Delta x}\right)^2 f(x), \tag{7.1}$$

with $f(x)$ given as

$$f(x) = \frac{4}{c^2}\left[\left(\frac{\Delta x}{x_2 - 2x_1 + x}\right)^2 + \left(\frac{\Delta x}{x_2 - x}\right)^2 - 2\right]. \tag{7.2}$$

In Eq. (7.2) x_1 and x_2 mark the beginning and ending position of the CAP and $\Delta x = x_2 - x_1$; the constant c is set to one.

Here, and in the following, we use the CAP not only as an absorbing layer but as an *electrode*. To illustrate how CAPs are used as electrodes we consider again the one-dimensional carbon chain (see Sec. 2.3, p. 18). Figure 7.8 shows the transmission function and the density of states of a one-dimensional carbon chain within the nearest neighbor tight binding approximation. We plot the transmission function and DOS for different lengths of the CAP region and compare the results with a conventional two-terminal transport calculation.

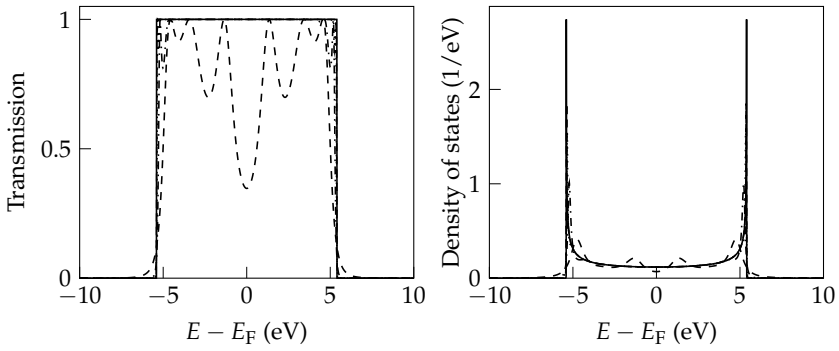

FIGURE 7.8 | Convergence of transmission function (a) and density of states (b) of CAP electrodes with increasing size (dashed line styles) compared to conventional semi-infinite electrodes (solid line).

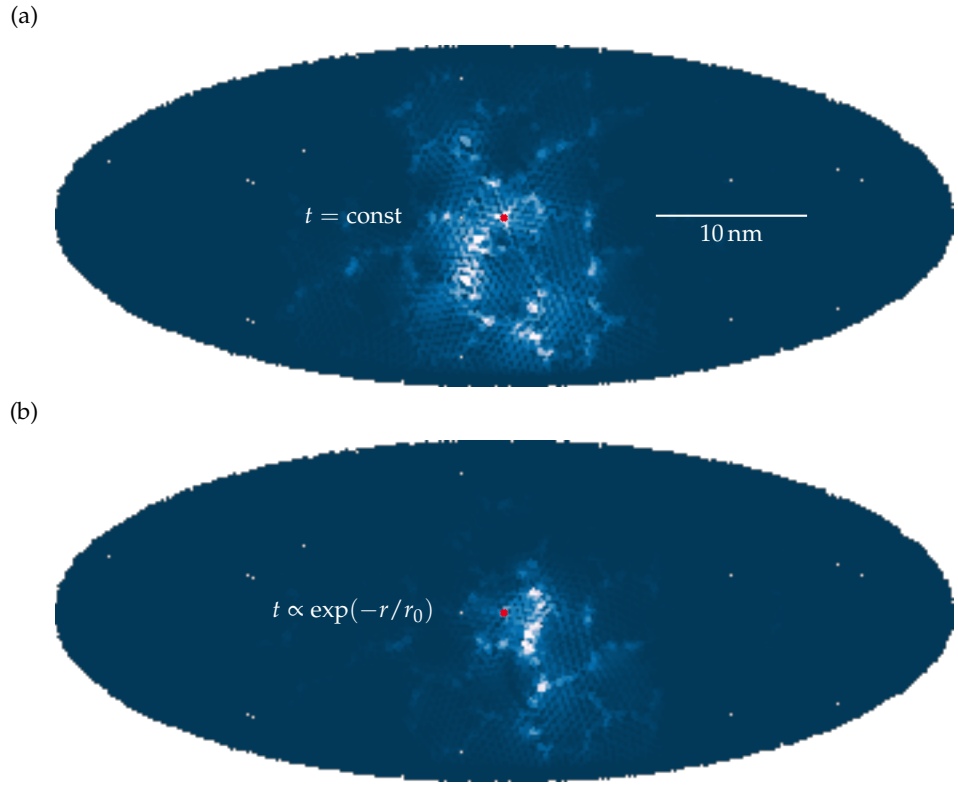

FIGURE 7.9 | Transport in a polycrystal via complex absorbing potential. The tight binding model uses constant (a) and strain-dependent (b) hopping. Color brightness indicates the bond current value, where high values are associated with bright color.

Apparently, both the transmission function and the DOS converge against the *normal* values with increasing CAP size. This result indicates that the simplicity of the electronic structure of the electrode, containing only the position dependent imaginary diagonal term of Eq. (7.1), is bought at the price of larger electrodes.

Figure 7.9 shows a bond current map of a transport setup where a single state is injected into the center of the device (red dot). We compare a fixed tight binding parameter with a strain-dependent parameter. The fixed hopping setup [Fig. 7.9 (a)] shows far reaching currents with significant contributions of the GBs. Taking the strain-dependence of the hopping parameter into account [Fig. 7.9 (b)] the bond currents are more confined to the center of the structure but transport via GBs still dominates.

From the results of Fig. 7.9 the question may arise how these observations are affected by the location of the injection site. Figure 7.10 shows four configurations in which electrons are injected north, south, east and west with respect to the grain center. Apart from injection at the south, the bond current maps look very similar. Apparently, the GB at the east is most conductive and

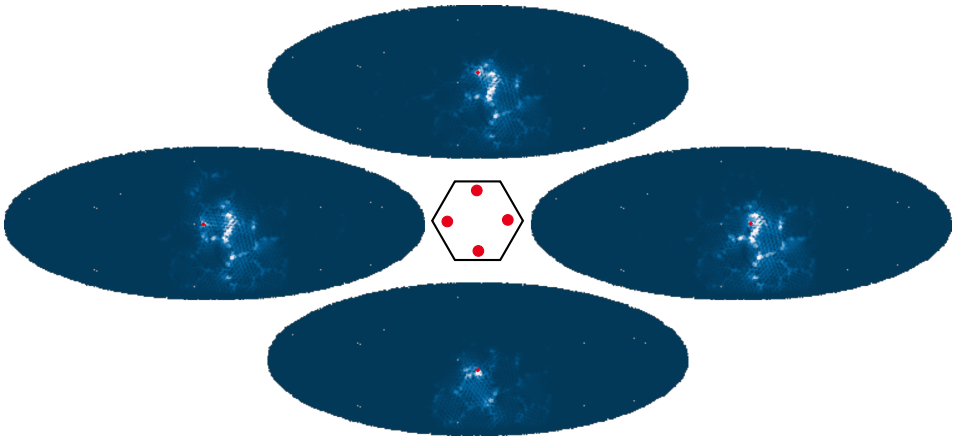

FIGURE 7.10 | Influence of injection sites on bond currents. The central scheme shows injection sites (filled red circles) relative to the grain center. Color maps of bond currents are shown correspondingly.

states injected at the north, west and east are transported via this GB. In the case of injection at the south the states reach another GB first and thus bypass the GB at the east. The general impression of enhanced conductivity at GBs is, however, uncontested if injection sites are changed.

The CAP transport setup demonstrates that GBs exhibit enhanced conductivity at low energies. All bond current maps in this section have been obtained at the Fermi-level. These calculations therefore support the impression already gained in Sec. 7.3 based on the conventional two-terminal setup.

7.5 TRANSPORT STATISTICS OF GRAPHENE POLYCRYSTALS

The noisy transmission function that may be caused by multiple effects—the artificial electrode-device interface, pronounced transmission along the GB, holes in the GBs—challenges our initial plan to relate the polycrystal transport to a network of individual bicrystal transports severely. We expected that distinct transmission regimes could be discriminated in which individual bicrystal transport sets on. In the remaining sections of this chapter we therefore resort to a statistical analysis of the transmission function in order to eventually compute strain gauge factors (Sec. 7.6).

We first consider the transport characteristics of polycrystals with grain orientation from Fig. 7.3 (a), in the following called *A-orientation*. We have chosen grain sizes between 1.48 nm to 3.93 nm and place the individual grains with random rotation. The rotation is drawn from the interval of $0° - 30°$ because of the intrinsic mirror plane in the setup. As shown in Fig. 7.11 the grains are constructed in such a fashion that an integer multiple of armchair graphene unit cells can be used as an electrode.

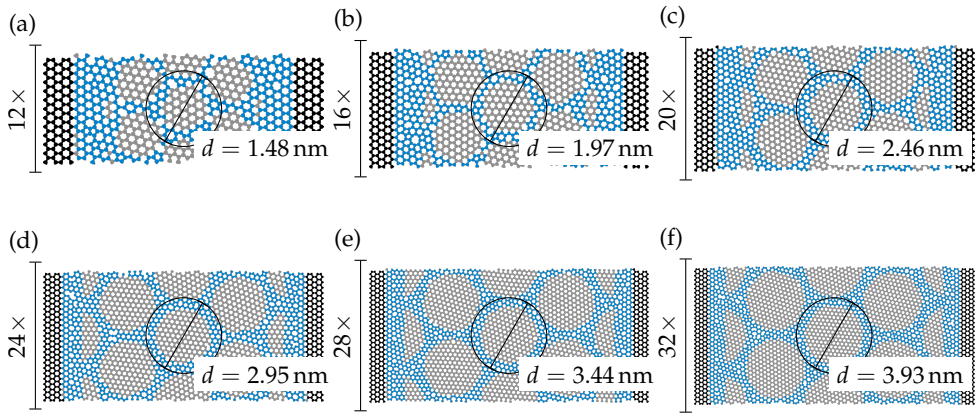

FIGURE 7.11 | Polycrystal structures for two-terminal transport calculations. The models are adapted to fit pristine graphene leads. On the left side of each structure the number of armchair graphene units is indicated.

Figure 7.12 shows the (logarithmic) transmission function averaged over differently oriented grains for a fixed grain size. Compared to the noisy transmission of a single polycrystal (Fig. 7.5), the statistical averaging has led to a notable smoothing. Nevertheless, no remarkable onset regions can be identified. Rather we see a grain size effect: For the polycrystals with grains at 3.93 nm diameter the transmission is very smooth but resembles neither bulk

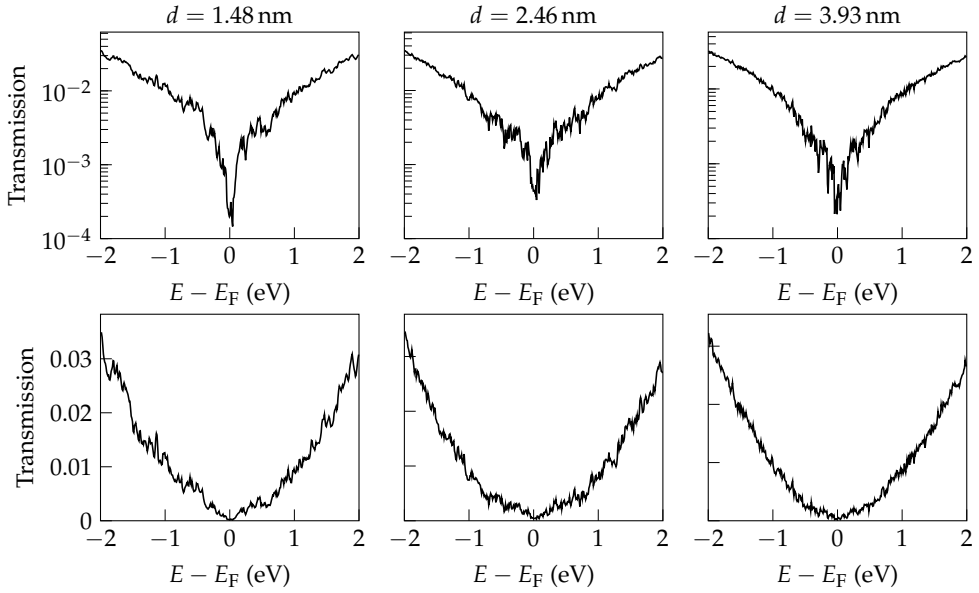

FIGURE 7.12 | Averaged transmission functions for the polycrystal setups in Fig. 7.3 (a) at different grain sizes. Twenty structures per grain size were are used for the averaging.

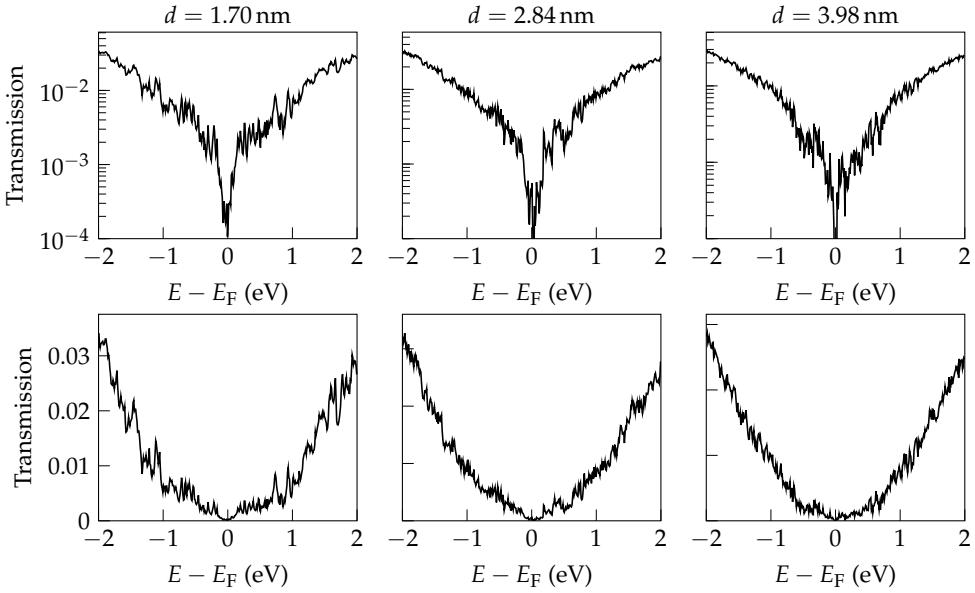

FIGURE 7.13 | Averaged transmission functions for the polycrystal setups in Fig. 7.3 (b) at different grain sizes. Ten structures per grain size were are used for the averaging.

graphene nor exhibits any pronounced features. The smoothing of the transmission functions with increasing grain size may be related to the increased bulk content.

Transport with the orientation based on Fig. 7.3 (b)—*B-orientation* for short—presents a very similar picture. Due to the hexagonally shaped grains the grain sizes for the B-orientation are slightly larger given the same pristine graphene electrode size. As for the A-orientation we show the smallest grain size together with a medium and the largest size in Fig. 7.13. The grain size effect on the smoothness of the transmission function corresponds to Fig. 7.12. However, the transmission functions are somewhat coarser so that the 3.98 nm grains in Fig. 7.13 resemble rather the 2.46 nm grains in Fig. 7.12. This difference may be related to the fact that within the B-orientation, GBs are not aligned along the transport direction. Since Secs. 7.3 and 7.4 have indicated that low energy transmission along GBs is significant, the B-orientation may therefore show reduced transmission at low energies compared to the A-orientation for the corresponding grain size.

7.6 PIEZORESISTIVITY OF NANOCRYSTALS

For the two sets of polycrystal orientations and grain sizes we compute the transmission function under a strain up to 0.5%. In Fig. 7.14 the strain gauge factors for the grain sizes of Fig. 7.12 and the orientations of Fig. 7.3 are shown as a function of strain. We determine these strain gauge factors from the

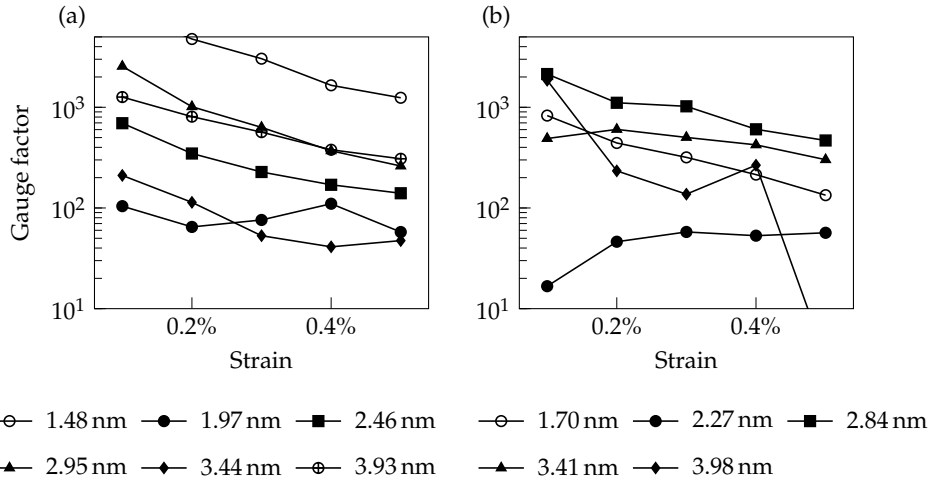

FIGURE 7.14 | Averaged strain gauge factor based on zero-bias conductance for differently sized polycrystals in A-orientation (a) and B-orientation (b).

zero-bias conductance [108, 127]

$$G^0 = \frac{2e}{h} \int \mathrm{d}E\, T(E) \left[-\frac{\partial f_0(E)}{\partial E} \right], \tag{7.3}$$

where $T(E)$ is the zero-bias transmission function and f_0 is the equilibrium Fermi distribution function. Since we are interested only in relative changes of G^0 at different strains, we drop the prefactor that ensures that G^0 is dimensionally a conductance.

Ideally, the gauge factor is constant with a high value. Figure 7.14 shows that the gauge factor is somewhat constant within a strain interval between 0.2% and 0.4% for most grain sizes and particularly for the B-orientation. The largest deviation occurs in the polycrystals with smallest and largest grain diameter. Of course, since the gauge factors are displayed on a semi-logarithmic scale the detailed values vary significantly. But here we are more interested in the order of magnitude. Comparing our gauge factors with experimental results (Fig. 1.10, p. 9) shows that nearly all polycrystals that we studied exceed experimental gauge factors considerably. Similar to these measurements our gauge factors drop at increasing strain. Unfortunately, we observe no trend with regard to the grain size. A possible explanation is that our models are too small to pass the threshold where a finite size effect can be identified.

Despite the missing size trend for our gauge factor and with some caution we are inclined to see the increased piezoresistive response of nanocrystalline graphene as a *finite size* effect: The higher density of GB atoms impacts both the transmission and the transmission under strain to a larger extent than in larger graphene samples. We believe that especially the significant contribution

of transport along the GB network to the overall transport behavior is an argument for the finite size effect.

Summary In this chapter we have investigated the enhanced piezoresistive response in nanocrystalline graphene. We reduced the structural complexity of real-world samples by designing hexagonally shaped grains with well defined orientation relations. Although structurally simple, transport calculations of the polycrystal revealed significant noise that we attribute to additional point scattering not present in bicrystals. In this context our initial plan to use the results of Ch. 6 to infer the transport characteristics of the polycrystal was premature. Transport in polycrystals at low energies is dominated by transmission along the GB network supported by an analysis using complex absorbing potential as a complementary transport setup. To remedy the transmission noise we averaged the transmission function at various grain sizes over a statistical ensemble of randomly orientated grains. This averaging smoothes the transmission curves but does not reveal any prominent transport regimes. Similarly, a grain size effect on the strain gauge factor could not clearly be identified. The absolute magnitude of the gauge factor is, however, large for the smaller grains which indicates that a size effect may cause the enhanced piezoresistivity of nanocrystalline graphene.

> To explain all nature is too difficult a task for any one man or even for any one age. 'Tis much better to do a little with certainty, & leave the rest for others that come after you, than to explain all things by conjecture without making sure of any thing.
>
> ISAAC NEWTON

Admittedly, we have not explained all nature, not even all graphene! But our goal was more modest from the beginning: We tried to explain the enhanced piezoresistivity of nanocrystalline graphene, observed experimentally, based on a quantum mechanical ballistic transport model.

To start, we considered graphene bicrystals with armchair/zigzag orientation. This orientation is interesting because it allows to tune the interface length without changing the orientation relation. Leaving the geometric aspects of the grain boundary (GB) aside, we focussed on the influence of local structural modifications at the GB on transport characteristics. We found that the transport response decomposes into two regimes that show very different sensitivity to the local structure. An energy gap region around the Fermi energy is completely insensitive to the detailed atomic structure at the GB, while the transmission and current-voltage characteristics beyond the energy gap are strongly affected.

The dependence of the transport energy gap solely on the geometric parameters of the bicrystal has motivated a more abstract treatment of the emergence and strain modulation of transport gaps for arbitrary graphene bicrystals. With this treatment we could show that transport gap modulations can be completely deduced by combining the electronic structure of pristine graphene with geometric manipulations without resorting to explicit transport calculations. This semi-analytical approach may be extended into arbitrary other field-dependent response functions in future work.

The detailed investigation of bicrystal transport properties has served as a prelude to the study of transport in polycrystalline graphene. In such extended structures the complexity of description increases drastically. To cope with these difficulties we employed a simple tight binding based electronic structure description and performed two-terminal transport calculations as well as more sophisticated calculations based on complex absorbing potentials. We used these transport configurations eventually to determine how strain modulates the conductivity in structurally simplified graphene polycrystals. We computed strain gauge factors for these systems bringing us technically

close to experimentally determined gauge factors of nanocrystalline graphene.

While we were unable to find a straightforward dependence of strain gauge factors on structural features of the polycrystal or completely reduce the transport behavior of a polycrystal to an equivalent resistor network, we could demonstrate that GBs play a decisive role at low bias electron transport due to their metallic nature induced by defect resonances of the density of states. A statistical analysis of transport in differently sized grains has shown an increasingly non-bulk behavior with decreasing grain size. From this observation we conclude that the enhanced piezoresistivity of nanocrystalline graphene is primarily a finite size effect.

We left out some aspects of the transport problem in nanocrystalline graphene for the sake of conceptual simplicity. Also, it is clear that a complex problem such as non-equilibrium quantum dynamics on extended defective structures can only be tackled step by step. New levels of complexity, however, can be added systematically based on the results and methods used in this work.

A prominent example is the buckling of the graphene sheet. The main difficulty for treating this problem is an efficient but realistic description of the electronic structure. Ideally, a parametrical tight-binding description, similar to the inclusion of strain dependence (Sec. 6.2) could be found. Having established a proper electronic structure of the buckled system, our transport models could be used directly.

Another interesting outlook is provided by the use of complex absorbing potentials (CAPs) in our polycrystal transport study. Indeed, CAPs have obtained specialized interest because they can be easily used in time-dependent transport problems. The emerging field of terahertz spectroscopy would be an interesting play-field for our methods.

Certainly, there are plenty of further details and questions that emerge from our work. As so often in science, we were able to provide answers to some of the questions that motivated our work initially, altered many questions during our work, and leave questions for new work.

CURRICULUM VITÆ

— RESEARCH EXPERIENCE

Scientific staff member (*Wissenschaftlicher Mitarbeiter*)
and study towards a doctoral degree, 2017–2023
Materials Modelling group (Prof. Karsten Albe)
Technische Universität Darmstadt, Germany

Visiting scientist (three months), 2019
Nanomaterials and Devices group (Prof. Mads Brandbyge)
Technical University of Denmark (DTU), Denmark

— EDUCATION

Study of materials science (M. Sc.), 2015–2017
Technische Universität Darmstadt, Germany

Study of materials science (B. Sc.), 2012–2015
Technische Universität Darmstadt, Germany

Secondary education (*Abitur*), 2003–2012
Heinrich-Mann-Schule, Dietzenbach, Germany

— PROJECT-RELATED PEER-REVIEWED PUBLICATIONS

D. Perera and J. Rohrer, *Semi-analytical approach to transport gaps in polycrystalline graphene*, Nanoscale **13**, 7709-7713 (2021).

D. Perera and J. Rohrer, *Structure sensitivity of electronic transport across graphene grain boundaries*, Phys. Rev. B **98**, 155432 (2018).

— OTHER PEER-REVIEWED PUBLICATIONS

S. Kumar, Y. Pramudya, K. Müller, A. Chandresh, S. Dehm, S. Heidrich, A. Fediai, D. Parmar, **D. Perera**, M. Rommel, L. Heinke, W. Wenzel, C. Wöll, and R. Krupke, *Sensing molecules with metal–organic framework functionalized graphene transistors*, Adv. Mater. **43**, 2103316 (2021).

M. Tran, A. Malik, M. Dürrschnabel, A. Regoutz, P. Thakur, T. Lee, **D. Perera**, L. Molina-Luna, K. Albe, J. Rohrer, and C. Birkel, *Experimental and theoretical investigation of the chemical exfoliation of Cr-based MAX phase particles*, Dalton Trans. **49**, 12215-12221 (2020).

F. Moitzi, D. Şopu, D. Holec, **D. Perera**, N. Mousseau, and J. Eckert, *Chemical bonding effects on the brittle-to-ductile transition in metallic glasses*, Acta Mater. **188**, 273-281 (2020).

R. Yekani, E. Rusak, A. Riaz, A. Felten, B. Breitung, S. Dehm, **D. Perera**, J. Rohrer, C. Rockstuhl, and R. Krupke, *Formation of nanocrystalline graphene on germanium*, Nanoscale **10**, 12156-12162 (2018).

— OTHER PUBLICATIONS

D. Perera, *Influence of Hydrogen on the Electronic Structure of Grain Boundaries in Graphene*, M. Sc. thesis, Technische Universität Darmstadt, June 2017.

D. Perera, *Density Functional Theory Calculations on Tilt Grain Boundaries in Graphene*, B. Sc. thesis, Technische Universität Darmstadt, August 2015.

— ORAL PRESENTATIONS AT INTERNATIONAL CONFERENCES

*Underlined names indicate who presented the work.

D. Perera* and J. Rohrer, *Conductivity tuning of polycrystalline graphene by mechanical strain*, **Annual Meeting 2019 GDR-I Graphene & Co.**, Bad Herrenalb, Germany.

D. Perera and J. Rohrer, *Mechanically tuned conductivity of polycrystalline graphene*, **Graphene Week 2019**, Helsinki, Finland.

D. Perera, J. Rohrer, and K. Albe, *Mechanically tuned conductivity of graphene grain boundaries from first-principles calculations*, **DPG Spring Meeting 2019**, Regensburg, Germany.

D. Perera, J. Rohrer, and K. Albe, *Influence of local grain boundary structure on electronic transport in polycrystalline graphene*, **MSE Congress 2018**, Darmstadt, Germany.

D. Perera, J. Rohrer, and K. Albe, *Influence of local grain boundary structure on electronic transport in polycrystalline graphene*, **DPG Spring Meeting 2018**, Berlin, Germany.

— POSTER PRESENTATIONS AT INTERNATIONAL CONFERENCES

D. Perera and J. Rohrer, *Structure sensitivity of electronic transport across graphene grain boundaries*, **CAMD Summer School 2018**, Helsingør, Denmark.

D. Perera, J. Rohrer, and K. Albe, *Influence of local grain boundary structure on electronic transport in polycrystalline graphene*, **Workshop on grain boundaries in semiconducting oxides 2018**, Edesheim, Germany.

BIBLIOGRAPHY

[1] A. Geim, *Graphene: Status and prospects*, Science **324**, 1530 (2009).

[2] A. K. Geim, *Nobel lecture: Random walk to graphene*, Rev. Mod. Phys. **83**, 851 (2011).

[3] F. Schwierz, *Graphene transistors*, Nat. Nanotech. **5**, 487 (2010).

[4] A. C. Ferrari, F. Bonaccorso, V. Fal'ko, K. S. Novoselov, S. Roche, P. Bøggild, S. Borini, F. H. Koppens, V. Palermo, N. Pugno, J. A. Garrido, R. Sordan, A. Bianco, L. Ballerini, M. Prato, E. Lidorikis, J. Kivioja, C. Marinelli, T. Ryhänen, A. Morpurgo, J. N. Coleman, V. Nicolosi, L. Colombo, A. Fert, M. Garcia-Hernandez, A. Bachtold, G. F. Schneider, F. Guinea, C. Dekker, M. Barbone, Z. Sun, C. Galiotis, A. N. Grigorenko, G. Konstantatos, A. Kis, M. Katsnelson, L. Vandersypen, A. Loiseau, V. Morandi, D. Neumaier, E. Treossi, V. Pellegrini, M. Polini, A. Tredicucci, G. M. Williams, B. Hee Hong, J.-H. Ahn, J. Min Kim, H. Zirath, B. J. van Wees, H. van der Zant, L. Occhipinti, A. Di Matteo, I. A. Kinloch, T. Seyller, E. Quesnel, X. Feng, K. Teo, N. Rupesinghe, P. Hakonen, S. R. Neil, Q. Tannock, T. Löfwander, and J. Kinaret, *Science and technology roadmap for graphene, related two-dimensional crystals, and hybrid systems*, Nanoscale **7**, 4598 (2015).

[5] A. Riaz, F. Pyatkov, A. Alam, S. Dehm, A. Felten, V. S. K. Chakravadhanula, B. S. Flavel, C. Kübel, U. Lemmer, and R. Krupke, *Light emission, light detection and strain sensing with nanocrystalline graphene*, Nanotechnology **26**, 325202 (2015).

[6] A. Smith, F. Niklaus, A. Paussa, S. Vaziri, A. Fischer, M. Sterner, F. Forsberg, A. Delin, D. Esseni, P. Palestri, M. Östling, and M. Lemme, *Electromechanical piezoresistive sensing in suspended graphene membranes*, Nano Lett. **13**, 3237 (2013).

[7] A. D. Smith, F. Niklaus, A. Paussa, S. Schröder, A. C. Fischer, M. Sterner, S. Wagner, S. Vaziri, F. Forsberg, D. Esseni, M. Östling, and M. C. Lemme, *Piezoresistive properties of suspended graphene membranes under uniaxial and biaxial strain in nanoelectromechanical pressure sensors*, ACS Nano **10**, 9879 (2016).

[8] K. S. Novoselov, A. K. Geim, S. V. Morozov, D. Jiang, Y. Zhang, S. V. Dubonos, I. V. Grigorieva, and A. A. Firsov, *Electric field effect in atomically thin carbon films*, Science **306**, 666 (2004).

[9] K. Novoselov, D. Jiang, F. Schedin, T. Booth, V. Khotkevich, S. Morozov, and A. Geim, *Two-dimensional atomic crystals*, Proc. Natl. Acad. Sci. **102**, 10451 (2005).

[10] K. Novoselov, A. Geim, S. Morozov, D. Jiang, M. Katsnelson, I. Grigorieva, S. Dubonos, and A. Firsov, *Two-dimensional gas of massless Dirac fermions in graphene*, Nature **438**, 197 (2005).

[11] Y. Zhang, Y.-W. Tan, H. L. Stormer, and P. Kim, *Experimental observation of the quantum hall effect and berry's phase in graphene*, Nature **438**, 201 (2005).

[12] K. Novoselov, *Nobel lecture: Graphene: materials in the flatland*, Rev. Mod. Phys. **83**, 837 (2011).

[13] K. Novoselov, V. Fal'ko, L. Colombo, P. Gellert, M. Schwab, and K. Kim, *A roadmap for graphene*, Nature **490**, 192 (2012).

[14] V. Meunier, A. Souza Filho, E. Barros, and M. Dresselhaus, *Physical properties of low-dimensional sp2-based carbon nanostructures*, Rev. Mod. Phys. **88**, 025005 (2016).

[15] F. Pulizzi, O. Bubnova, S. Milana, D. Schilter, D. Abergel, and A. Moscatelli, *Graphene in the making*, Nat. Nanotechnol. **14**, 914 (2019).

[16] P. Wallace, *The band theory of graphite*, Phys. Rev. **71**, 622 (1947).

[17] H. Boehm, A. Clauss, G. Fischer, and U. Hofmann, *Dünnste Kohlenstoff-Folien*, Z. Naturforsch. B **17**, 150 (1962).

[18] H. Kroto, J. Heath, S. O'Brien, R. Curl, and R. Smalley, *C60: Buckminsterfullerene*, Nature **318**, 162 (1985).

[19] S. Iijima, *Helical microtubules of graphitic carbon*, Nature **354**, 56 (1991).

[20] N. Hamada, S. Sawada, and A. Oshiyama, *New one-dimensional conductors: Graphitic microtubules*, Phys. Rev. Lett. **68**, 1579 (1992).

[21] R. Saito, M. Fujita, G. Dresselhaus, and M. S. Dresselhaus, *Electronic structure of chiral graphene tubules*, Appl. Phys. Lett. **60**, 2204 (1992).

[22] J. Mintmire, D. Robertson, and C. White, *Properties of fullerene nanotubules*, J. Phys. Chem. Solids **54**, 1835 (1993).

[23] S. Reich, J. Maultzsch, C. Thomsen, and P. Ordejón, *Tight-binding description of graphene*, Phys. Rev. B **66**, 035412 (2002).

[24] J. Mintmire and C. White, *Universal density of states for carbon nanotubes*, Phys. Rev. Lett. **81**, 2506 (1998).

[25] C. White and J. Mintmire, *Density of states reflects diameter in nanotubes*, Nature **394**, 29 (1998).

[26] J. McClure, *Band structure of graphite and de Haas-van Alphen effect*, Phys. Rev. **108**, 612 (1957).

[27] J. McClure, *Theory of diamagnetism of graphite*, Phys. Rev. **119**, 606 (1960).

[28] J. Slonczewski and P. Weiss, *Band structure of graphite*, Phys. Rev. **109**, 272 (1958).

[29] G. W. Semenoff, *Condensed-matter simulation of a three-dimensional anomaly*, Phys. Rev. Lett. **53**, 2449 (1984).

[30] M. Katsnelson, K. Novoselov, and A. Geim, *Chiral tunnelling and the Klein paradox in graphene*, Nat. Phys. **2**, 620 (2006).

[31] K. Novoselov, A. Geim, S. Morozov, D. Jiang, M. Katsnelson, I. Grigorieva, S. Dubonos, and A. Firsov, *Two-dimensional gas of massless Dirac fermions in graphene*, Nature **438**, 197 (2005).

[32] A. Geim and K. Novoselov, *The rise of graphene*, Nat. Mater. **6**, 183 (2007).

[33] N. Stander, B. Huard, and D. Goldhaber-Gordon, *Evidence for Klein tunneling in graphene p-n junctions*, Phys. Rev. Lett. **102**, 026807 (2009).

[34] A. F. Young and P. Kim, *Quantum interference and Klein tunnelling in graphene heterojunctions*, Nat. Phys. **5**, 222 (2009).

[35] A. Castro Neto, F. Guinea, N. Peres, K. Novoselov, and A. Geim, *The electronic properties of graphene*, Rev. Mod. Phys. **81**, 109 (2009).

[36] N. Peres, F. Guinea, and A. Castro Neto, *Electronic properties of disordered two-dimensional carbon*, Phys. Rev. B **73**, 125411 (2006).

[37] A. Lherbier, S. M.-M. Dubois, X. Declerck, Y.-M. Niquet, S. Roche, and J.-C. Charlier, *Transport properties of graphene containing structural defects*, Phys. Rev. B **86**, 075402 (2012).

[38] M. Dresselhaus and G. Dresselhaus, *Intercalation compounds of graphite*, Adv. Phys. **51**, 1 (2002).

[39] T. Wassmann, A. P. Seitsonen, A. M. Saitta, M. Lazzeri, and F. Mauri, *Structure, stability, edge states, and aromaticity of graphene ribbons*, Phys. Rev. Lett. **101**, 096402 (2008).

[40] T.-H. Liu, G. Gajewski, C.-W. Pao, and C.-C. Chang, *Structure, energy, and structural transformations of graphene grain boundaries from atomistic simulations*, Carbon **49**, 2306 (2011).

[41] G. Soldano, M. Juarez, B. Teo, and E. Santos, *Structure and stability of graphene edges in O_2 and H_2 environments from* ab initio *thermodynamics*, Carbon **78**, 181 (2014).

[42] M. M. Ervasti, Z. Fan, A. Uppstu, A. V. Krasheninnikov, and A. Harju, *Silicon and silicon-nitrogen impurities in graphene: Structure, energetics, and effects on electronic transport*, Phys. Rev. B **92**, 235412 (2015).

[43] F. Gargiulo, G. Autès, N. Virk, S. Barthel, M. Rösner, L. R. Toller, T. O. Wehling, and O. V. Yazyev, *Electronic transport in graphene with aggregated hydrogen adatoms*, Phys. Rev. Lett. **113**, 246601 (2014).

[44] M. Mohr, K. Papagelis, J. Maultzsch, and C. Thomsen, *Two-dimensional electronic and vibrational band structure of uniaxially strained graphene from* ab initio *calculations*, Phys. Rev. B **80**, 205410 (2009).

[45] V. M. Pereira, A. Castro Neto, and N. Peres, *Tight-binding approach to uniaxial strain in graphene*, Phys. Rev. B **80**, 045401 (2009).

[46] V. M. Pereira and A. Castro Neto, *Strain engineering of graphene's electronic structure*, Phys. Rev. Lett. **103**, 046801 (2009).

[47] V. Torres, D. Faria, and A. Latgé, *Tuning transport properties of graphene three-terminal structures by mechanical deformation*, Phys. Rev. B **97**, 165429 (2018).

[48] V. Barone, O. Hod, and G. E. Scuseria, *Electronic structure and stability of semiconducting graphene nanoribbons*, Nano Lett. **6**, 2748 (2006).

[49] Y.-W. Son, M. L. Cohen, and S. G. Louie, *Energy gaps in graphene nanoribbons*, Phys. Rev. Lett. **97**, 216803 (2006).

[50] L. Lin, H. Peng, and Z. Liu, *Synthesis challenges for graphene industry*, Nat. Mater. **18**, 520 (2019).

[51] L. A. Jauregui, H. Cao, W. Wu, Q. Yu, and Y. P. Chen, *Electronic properties of grains and grain boundaries in graphene grown by chemical vapor deposition*, Solid State Commun. **151**, 1100 (2011).

[52] L. P. Biró and P. Lambin, *Grain boundaries in graphene grown by chemical vapor deposition*, New J. Phys. **15**, 035024 (2013).

[53] Y. Tison, J. Lagoute, V. Repain, C. Chacon, Y. Girard, F. Joucken, R. Sporken, F. Gargiulo, O. V. Yazyev, and S. Rousset, *Grain boundaries in graphene on SiC(000$\bar{1}$) substrate*, Nano Lett. **14**, 6382 (2014).

[54] J. Coraux, A. T. N'Diaye, C. Busse, and T. Michely, *Structural coherency of graphene on Ir(111)*, Nano Lett. **8**, 565 (2008).

[55] X. Li, W. Cai, J. An, S. Kim, J. Nah, D. Yang, R. Piner, A. Velamakanni, I. Jung, E. Tutuc, S. Banerjee, L. Colombo, and R. Ruoff, *Large-area synthesis of high-quality and uniform graphene films on copper foils*, Science **324**, 1312 (2009).

[56] X. Li, W. Cai, L. Colombo, and R. S. Ruoff, *Evolution of graphene growth on Ni and Cu by carbon isotope labeling*, Nano Lett. **9**, 4268 (2009).

[57] A. C. Ferrari and D. M. Basko, *Raman spectroscopy as a versatile tool for studying the properties of graphene*, Nat. Nanotech. **8**, 235 (2013).

[58] A. Eckmann, A. Felten, A. Mishchenko, L. Britnell, R. Krupke, K. S. Novoselov, and C. Casiraghi, *Probing the nature of defects in graphene by Raman spectroscopy*, Nano Lett. **12**, 3925 (2012).

[59] M. Huang, H. Yan, T. F. Heinz, and J. Hone, *Probing strain-induced electronic structure change in graphene by Raman spectroscopy*, Nano Lett. **10**, 4074 (2010).

[60] S. Bae, H. Kim, Y. Lee, X. Xu, J.-S. Park, Y. Zheng, J. Balakrishnan, T. Lei, H. Ri Kim, Y. I. Song, Y.-J. Kim, K. S. Kim, B. Özyilmaz, J.-H. Ahn, B. H. Hong, and S. Iijima, *Roll-to-roll production of 30-inch graphene films for transparent electrodes*, Nat. Nanotech. **5**, 574 (2010).

[61] S.-H. Bae, Y. Lee, B. K. Sharma, H.-J. Lee, J.-H. Kim, and J.-H. Ahn, *Graphene-based transparent strain sensor*, Carbon **51**, 236 (2013).

[62] B. Yang, H. Xu, J. Lu, and K. P. Loh, *Periodic grain boundaries formed by thermal reconstruction of polycrystalline graphene film*, J. Am. Chem. Soc. **136**, 12041 (2014).

[63] R. Grantab, V. Shenoy, and R. Ruoff, *Anomalous strength characteristics of tilt grain boundaries in graphene*, Science **330**, 946 (2010).

[64] J. Kotakoski and J. C. Meyer, *Mechanical properties of polycrystalline graphene based on a realistic atomistic model*, Phys. Rev. B **85**, 195447 (2012).

[65] Y. Wei, J. Wu, H. Yin, X. Shi, R. Yang, and M. Dresselhaus, *The nature of strength enhancement and weakening by pentagon–heptagon defects in graphene*, Nat. Mater. **11**, 759 (2012).

[66] H. I. Rasool, C. Ophus, W. S. Klug, A. Zettl, and J. K. Gimzewski, *Measurement of the intrinsic strength of crystalline and polycrystalline graphene*, Nat. Commun. **4**, 2811 (2013).

[67] A. Shekhawat and R. O. Ritchie, *Toughness and strength of nanocrystalline graphene*, Nat. Commun. **7**, 10546 (2016).

[68] C. Ophus, A. Shekhawat, H. Rasool, and A. Zettl, *Large-scale experimental and theoretical study of graphene grain boundary structures*, Phys. Rev. B **92**, 205402 (2015).

[69] O. V. Yazyev and S. G. Louie, *Topological defects in graphene: Dislocations and grain boundaries*, Phys. Rev. B **81**, 195420 (2010).

[70] Y. Liu and B. I. Yakobson, *Cones, pringles, and grain boundary landscapes in graphene topology*, Nano Lett. **10**, 2178 (2010).

[71] O. V. Yazyev and Y. P. Chen, *Polycrystalline graphene and other two-dimensional materials*, Nat. Nanotech. **9**, 755 (2014).

[72] J. M. Carlsson, L. M. Ghiringhelli, and A. Fasolino, *Theory and hierarchical calculations of the structure and energetics of [0001] tilt grain boundaries in graphene*, Phys. Rev. B **84**, 165423 (2011).

[73] J. Wu and Y. Wei, *Grain misorientation and grain-boundary rotation dependent mechanical properties in polycrystalline graphene*, J. Mech. Phys. Solids **61**, 1421 (2013).

[74] J. Lahiri, Y. Lin, P. Bozkurt, I. I. Oleynik, and M. Batzill, *An extended defect in graphene as a metallic wire*, Nat. Nanotech. **5**, 326 (2010).

[75] D. Gunlycke and C. White, *Graphene valley filter using a line defect*, Phys. Rev. Lett. **106**, 136806 (2011).

[76] S. S. Alexandre, A. Lúcio, A. C. Neto, and R. Nunes, *Correlated magnetic states in extended one-dimensional defects in graphene*, Nano Lett. **12**, 5097 (2012).

[77] A. Fasolino, J. Los, and M. Katsnelson, *Intrinsic ripples in graphene*, Nat. Mater. **6**, 858 (2007).

[78] V. B. Shenoy, C. D. Reddy, A. Ramasubramaniam, and Y. W. Zhang, *Edge-stress-induced warping of graphene sheets and nanoribbons*, Phys. Rev. Lett. **101**, 245501 (2008).

[79] F. Ahmadpoor and P. Sharma, *A perspective on the statistical mechanics of 2D materials*, Extreme Mech. Lett. **14**, 38 (2017).

[80] J. H. Los, A. Fasolino, and M. I. Katsnelson, *Mechanics of thermally fluctuating membranes*, npj 2D Materials and Applications **1**, 9 (2017).

[81] S. Deng and V. Berry, *Wrinkled, rippled and crumpled graphene: An overview of formation mechanism, electronic properties, and applications*, Mater. Today **19**, 197 (2016).

[82] O. V. Yazyev and S. G. Louie, *Electronic transport in polycrystalline graphene*, Nat. Mater. **9**, 806 (2010).

[83] S. B. Kumar and J. Guo, *Strain-induced conductance modulation in graphene grain boundary*, Nano Lett. **12**, 1362 (2012).

[84] J. M. Soler, E. Artacho, J. D. Gale, A. García, J. Junquera, P. Ordejón, and D. Sánchez-Portal, *The SIESTA method for* ab initio *order-N materials simulation*, J. Phys. Condens. Matter **14**, 2745 (2002).

[85] A. García, N. Papior, A. Akhtar, E. Artacho, V. Blum, E. Bosoni, P. Brandimarte, M. Brandbyge, J. Cerdá, F. Corsetti, R. Cuadrado, V. Dikan, J. Ferrer, J. Gale, P. García-Fernández, V. García-Suárez, S. García, G. Huhs, S. Illera, R. Korytár, P. Koval, I. Lebedeva, L. Lin, P. López-Tarifa, S. G. Mayo, S. Mohr, P. Ordejón, A. Postnikov, Y. Pouillon, M. Pruneda, R. Robles, D. Sánchez-Portal, J. M. Soler, R. Ullah, V. W.-z. Yu, and J. Junquera, *Siesta: Recent developments and applications*, J. Chem. Phys. **152**, 204108 (2020).

[86] N. R. Papior, `SISL: V0.10` (2020).

[87] P. Hohenberg and W. Kohn, *Inhomogeneous electron gas*, Phys. Rev. **136**, B864 (1964).

[88] R. Jones and O. Gunnarsson, *The density functional formalism, its applications and prospects*, Rev. Mod. Phys. **61**, 689 (1989).

[89] W. Kohn and L. Sham, *Self-consistent equations including exchange and correlation effects*, Phys. Rev. **140**, A1133 (1965).

[90] W. Kohn, *Nobel lecture: Electronic structure of matter—wave functions and density functionals*, Rev. Mod. Phys. **71**, 1253 (1999).

[91] A. E. Mattsson, P. A. Schultz, M. P. Desjarlais, T. R. Mattsson, and K. Leung, *Designing meaningful density functional theory calculations in materials science—a primer*, Modelling Simul. Mater. Sci. Eng. **13**, R1 (2004).

[92] L. Thomas, *The calculation of atomic fields*, Math. Proc. Camb. Phil. Soc. **23**, 542 (1927).

[93] E. Fermi, *Un metodo statistico per la determinazione di alcune proprietà dell'atome*, Rend. Accad. Naz. Lincei **6**, 602 (1927).

[94] J. P. Perdew, K. Burke, and M. Ernzerhof, *Generalized gradient approximation made simple*, Phys. Rev. Lett. **77**, 3865 (1996).

[95] D. Sánchez-Portal, P. Ordejón, E. Artacho, and J. M. Soler, *Density-functional method for very large systems with LCAO basis sets*, Int. J. Quant. Chem. **65**, 453 (1997).

[96] N. Troullier and J. L. Martins, *Efficient pseudopotentials for plane-wave calculations*, Phys. Rev. B **43**, 1993 (1991).

[97] D. Hamann, M. Schlüter, and C. Chiang, *Norm-conserving pseudopotentials*, Phys. Rev. Lett. **43**, 1494 (1979).

[98] L. Kleinman and D. Bylander, *Efficacious form for model pseudopotentials*, Phys. Rev. Lett. **48**, 1425 (1982).

[99] H. J. Monkhorst and J. D. Pack, *Special points for Brillouin-zone integrations*, Phys. Rev. B **13**, 5188 (1976).

[100] H. Hellmann, *Einführung in die Quantenchemie* (Deuticke, Leipzig, 1937).

[101] R. Feynman, *Forces in molecules*, Phys. Rev. **56**, 340 (1939).

[102] E. Economou, *Green's functions in quantum physics* (Springer, Berlin, 2006).

[103] J. Slater and G. Koster, *Simplified LCAO method for the periodic potential problem*, Phys. Rev. **94**, 1498 (1954).

[104] W. A. Harrison, *Elementary Electronic Structure* (World Scientific, River Edge, 2004).

[105] Y. Hancock, A. Uppstu, K. Saloriutta, A. Harju, and M. J. Puska, *Generalized tight-binding transport model for graphene nanoribbon-based systems*, Phys. Rev. B **81**, 245402 (2010).

[106] V.-T. Tran, J. Saint-Martin, P. Dollfus, and S. Volz, *Third nearest neighbor parameterized tight binding model for graphene nano-ribbons*, AIP Adv. **7**, 075212 (2017).

[107] R. Landauer, *Spatial variation of currents and fields due to localized scatterers in metallic conduction*, IBM J. Res. & Dev. **1**, 223 (1957).

[108] S. Datta, *Electronic Transport in Mesoscopic Systems* (Cambridge University Press, Cambridge, 1995).

[109] M. Di Ventra, *Electrical Transport in Nanoscale Systems* (Cambridge University Press, Cambridge UK, New York, 2008).

[110] B. J. van Wees, H. van Houten, C. W. J. Beenakker, J. G. Williamson, L. P. Kouwenhoven, D. van der Marel, and C. T. Foxon, *Quantized conductance of point contacts in a two-dimensional electron gas*, Phys. Rev. Lett. **60**, 848 (1988).

[111] D. A. Wharam, T. J. Thornton, R. Newbury, M. Pepper, H. Ahmed, J. E. F. Frost, D. G. Hasko, D. C. Peacock, D. A. Ritchie, and G. A. C. Jones, *One-dimensional transport and the quantisation of the ballistic resistance*, J. Phys. C: Solid State Phys. **21**, L209 (1988).

[112] P. C. Martin and J. Schwinger, *Theory of many-particle systems. I*, Phys. Rev. **115**, 1342 (1959).

[113] M. P. L. Sancho, J. M. L. Sancho, J. M. L. Sancho, and J. Rubio, *Highly convergent schemes for the calculation of bulk and surface green functions*, J. Phys. F: Met. Phys. **15**, 851 (1985).

[114] M. Brandbyge, J.-L. Mozos, P. Ordejón, J. Taylor, and K. Stokbro, *Density-functional method for nonequilibrium electron transport*, Phys. Rev. B **65**, 165401 (2002).

[115] N. Papior, N. Lorente, T. Frederiksen, A. García, and M. Brandbyge, *Improvements on non-equilibrium and transport Green function techniques: The next-generation transiesta*, Comput. Phys. Commun. **212**, 8 (2017).

[116] T. N. Todorov, *Tight-binding simulation of current-carrying nanostructures*, J. Phys. Condens. Matter **14**, 3049 (2002).

[117] N. R. Papior, *Computational Tools and Studies of Graphene Nanostructures*, Ph.D. thesis, Technical University of Denmark (2016).

[118] G. Calogero, *Multi-scale atomistic simulations of graphene-based nanodevice*, Ph.D. thesis, Technical University of Denmark (2018).

[119] A. P. Thompson, H. M. Aktulga, R. Berger, D. S. Bolintineanu, W. M. Brown, P. S. Crozier, P. J. in 't Veld, A. Kohlmeyer, S. G. Moore, T. D. Nguyen, R. Shan, M. J. Stevens, J. Tranchida, C. Trott, and S. J. Plimpton, *LAMMPS - a flexible simulation tool for particle-based materials modeling at the atomic, meso, and continuum scales*, Comput. Phys. Commun. **271**, 108171 (2022).

[120] D. W. Brenner, O. A. Shenderova, J. A. Harrison, S. J. Stuart, B. Ni, and S. B. Sinnott, *A second-generation reactive empirical bond order (REBO) potential energy expression for hydrocarbons*, J. Phys. Condens. Matter **14**, 783 (2002).

[121] P. Erhart and K. Albe, *Analytical potential for atomistic simulations of silicon, carbon, and silicon carbide*, Phys. Rev. B **71**, 035211 (2005).

[122] D. Perera and J. Rohrer, *Structure sensitivity of electronic transport across graphene grain boundaries*, Phys. Rev. B **98**, 155432 (2018).

[123] G. Schusteritsch and C. J. Pickard, *Predicting interface structures: From $SrTiO_3$ to graphene*, Phys. Rev. B **90**, 035424 (2014).

[124] D. Perera and J. Rohrer, *Semi-analytical approach to transport gaps in polycrystalline graphene*, Nanoscale **13**, 7709 (2021).

[125] K. N. Kudin, G. E. Scuseria, and B. I. Yakobson, *C_2F, BN, and C nanoshell elasticity from* ab initio *computations*, Phys. Rev. B **64**, 235406 (2001).

[126] H. Xie, Y. Kwok, F. Jiang, X. Zheng, and G. Chen, *Complex absorbing potential based lorentzian fitting scheme and time dependent quantum transport*, J. Chem. Phys. **141**, 164122 (2014).

[127] S. Datta, *Quantum Transport: Atom to Transistor* (Cambridge University Press, Cambridge, 2005).